

QUANTUM AND SEMICLASSICAL CALCULATIONS
OF CAVITY QED SPECTRA

by

LIGUANG TIAN

A DISSERTATION

Presented to the Department of Physics
and the Graduate School of the University of Oregon
in partial fulfillment of the requirements
for the degree of
Doctor of Philosophy

June 1994

“Quantum and Semiclassical Calculations of Cavity QED Spectra,” a dissertation prepared by Liguang Tian in partial fulfillment of the requirements for the Doctor of Philosophy degree in the Department of Physics. This dissertation has been approved and accepted by:



Dr. Howard J. Carmichael, Chair of the Examining Committee

5/24/94
Date

Committee in charge:

Dr. Howard J. Carmichael, Chair
Dr. Nilendra G. Deshpande
Dr. Roger Haydock
Dr. Michael E. Kellman
Dr. Michael G. Raymer

Accepted by:



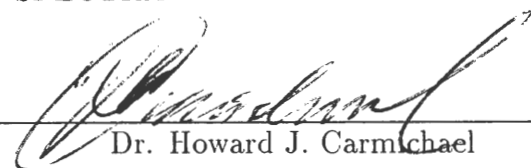
Vice Provost and Dean of the Graduate School

An Abstract of the Dissertation of

Liguang Tian for the degree of Doctor of Philosophy
in the Department of Physics to be taken June 1994

Title: QUANTUM AND SEMICLASSICAL CALCULATIONS OF CAVITY
QED SPECTRA

Approved:


Dr. Howard J. Carmichael

In this dissertation we study the interaction of a single atom with a single mode of the electromagnetic field in an optical cavity. We emphasize strong coupling conditions, where the dipole coupling strength is larger than the dissipation rates of the cavity and the atom.

By exciting the coupled atom and cavity mode with an external field, the excited-state spectroscopy of the coupled system is explored. Both quantum mechanical and semiclassical calculations are performed and their results are compared. In the limit of a weak driving field, both results show a two-peak (“vacuum” Rabi) spectrum. With increased strength of the driving field, differences are observed. The quantum calculation shows a multi-peak (two “vacuum” Rabi peaks plus additional peaks) spectrum, while the semiclassical calculation does not. These additional peaks are produced by transitions between the excited states of the Jaynes-Cummings

Hamiltonian indicative of the quantum nature of the coupled atom-cavity-mode system.

Another feature showing the quantum character of the coupled system is that an optical cavity containing one atom behaves, to a good approximation, like a two-state system when it is coherently excited on one of the “vacuum” Rabi resonances. It is shown that the cavity transmission exhibits the triplet Stark splitting of the Mollow spectrum. Quantum trajectory theory is used to study this two-state behavior.

Finally, the generation of Schrödinger cat states (superpositions of coherent states) using the coupled system of the atom and cavity mode is explored. These states are observed by using temporal-mode-matched homodyne detection. Quantum trajectories enable us to understand how loss destroys the Schrödinger cat.

CURRICULUM VITA

NAME OF AUTHOR: Liguang Tian

DATE OF BIRTH: May 15, 1965

GRADUATE AND UNDERGRADUATE SCHOOLS ATTENDED:

University of Oregon
Dalian University of Technology

DEGREES AWARDED:

Doctor of Philosophy in Physics, 1994, University of Oregon
Master of Science in Physics, 1991, University of Oregon
Bachelor of Science in Physics, 1984, Dalian University of Technology

AREAS OF SPECIAL INTEREST:

Quantum Optics and Laser Physics

PROFESSIONAL EXPERIENCE:

Research Assistant, Department of Physics, University of Oregon,
Eugene, 1990-94

Teaching Assistant, Department of Physics, University of Oregon,
Eugene, 1988-90

Assistant Professor of Physics, Dalian University of Technology,
China, 1986-88

PUBLICATIONS:

H. J. Carmichael, L. Tian, W. Ren, and P. Alsing, "Nonperturbative Atom-Photon Interactions in an Optical Cavity," in *Cavity Quantum Electrodynamics of Series of the Advances in Atomic, Molecular, and Optical Physics Volume*, edited by Paul R. Berman (Academic Press, Inc., 1993).

H. J. Carmichael, P. Kochan, and L. Tian, "Coherent States and Open Quantum System: a Comment on the Stern-Gerlach Effect and Schrödinger's Cat," in *Proceedings of the International Symposium on Coherent States: Past, Present, and Future*, edited by J. R. Klauder (World Scientific, Singapore, 1993).

J. X. Lin, C. Song, G. Xu and L. Tian, "Discussion on Limit Value at Long Wavelength End of CW CO Laser Operating in $X^1\Sigma^+$ State," *Quantum Electronics* **1**, 2 (1984).

L. Tian and H. J. Carmichael, "Quantum Trajectory Simulations of the Two-State Behavior of an Optical Cavity Containing One Atom," *Phys. Rev. A (Rapid Communications)* **46**, 6801 (1992).

L. Tian and H. J. Carmichael, "Incoherent Excitation of the Jaynes-Cummings System," *Quantum Opt.* **4**, 131 (1992).

L. Tian, C. Song, G. Xu and J. X. Lin, "Calculation and Analysis of the Small Signal Gain of CO Laser," *Academic Journal of Dalian Institute of Technology* **24**, 4 (1985).

ACKNOWLEDGMENTS

First and foremost I would like to express my sincere appreciation to Professor Howard Carmichael, my research and thesis adviser, for his guidance, support, and encouragement throughout my graduate work, and for teaching me the art of physics. The influence of his great scientific insight is an invaluable treasure to me. Special thanks are due to Professor Michael Raymer, from whom I have benefitted immensely both through his lectures on quantum optics and through group meetings. I sincerely thank Professor Tom Mossberg for the use of his lab facilities, and Professor Nilendra Deshpande for his advice and support. I thank Don Adkison and Dr. Paul Alsing for their help in the use of computers. I thank Professor Howard Carmichael and Dr. Wensheng Ren for their help in the preparation of this manuscript. Finally, I give my deep appreciation to my husband Raymond and to my sisters for their constant love and support.

DEDICATION

to My Parents

TABLE OF CONTENTS

Chapter	Page
I. INTRODUCTION	1
II. COHERENT EXCITATION: TRANSMISSION SPECTROSCOPY	10
2.1 Optical Bistability	11
2.2 Multi-photon Transitions	17
III. COHERENT EXCITATION: MODULATION SPECTROSCOPY.....	27
3.1 Modulation Spectroscopy Scheme.....	28
3.2 Numerical Results for Modulation Spectra.....	32
3.3 Analytical Results of the QED Calculation.....	40
3.4 Analytical Results of the Semiclassical Calculation	44
IV. INCOHERENT EXCITATION: SPECTROSCOPY.....	51
4.1 Matrix Elements Equations in the Secular Approximation.....	51
4.2 Steady-State Solutions	55
4.3 Spectra	57
4.4 Discussion	62
V. QUANTUM TRAJECTORY THEORY	70
5.1 Direct Photoelectric Detection.....	73
5.2 Homodyne Detection.....	82
VI. TWO-STATE BEHAVIOR.....	91
6.1 Photoelectron Counting Statistics	91
6.2 Optical Spectrum	101
VII. SCHRÖDINGER CATS	108
7.1 Wigner Function	109
7.2 Generation of Schrödinger Cats.....	110

	Page
7.3 Observation of Schrödinger Cats	117
VIII. SUMMARY AND CONCLUSIONS	126
BIBLIOGRAPHY	132

LIST OF FIGURES

Figure	Page
2.1 Schematic Diagram of a Single Atom in a Cavity Driven by a Coherent Field.....	13
2.2 The Transmission Spectrum Calculated from the Semiclassical Theory, Plotted as a Function of Driving Field Amplitude for $g/\kappa = 10$, $\gamma/2\kappa = 1$	15
2.3 The Transmission Spectrum Calculated from the Semiclassical Theory, Plotted as a Function of Driving Field Amplitude for $g/\kappa = 20$, $\gamma/2\kappa = 4$	16
2.4 The Transmission Spectrum Calculated from the QED Theory, Plotted as a Function of Driving Field Amplitude for $g/\kappa = 100$, $\gamma/2\kappa = 10$	22
2.5 Transmission spectra for $g/\kappa = 100$, $\gamma/2\kappa = 10$, and $\mathcal{E}/\kappa = 15$	24
2.6 Energy-Level Diagram for the Jaynes-Cummings Hamiltonian Showing Multi-Photon Transitions	25
3.1 The Modulation Spectrum Calculated from the QED Theory for $g/\kappa = 12$, $2g/\gamma = 5.6$	34
3.2 Energy-Level Diagram for an Atom-Cavity-Mode System	35
3.3 The Modulation Spectrum Calculated from the QED Theory for $g/\kappa = 25$, $g/2\kappa = 1$, and $\mathcal{E}/\kappa = 5$	36
3.4 The Modulation Spectrum Calculated from the QED Theory for $g/\kappa = 100$, $g/2\kappa = 1$, and $\mathcal{E}/\kappa = 5$	37
3.5 The Modulation Spectrum Calculated from the Semiclassical Theory for $g/\kappa = 12$, $2g/\gamma = 5.6$	39

3.6	Eigenvalues of Eq. (3.22) Plotted as a Function of $\langle \hat{a} \rangle_{ss}$ for $g/\kappa = 12$, $2g/\gamma = 5.6$	47
4.1	Schematic Diagram of a Single Atom in a Cavity Driven by Incoherent Fields	52
4.2	Spectra for Driving Field Intensities $N = 5$ and $M = 0$, and $2g/\gamma = 10$, $2\kappa/\gamma = 0.1$	63
4.3	Spectra for Driving Field Intensities $N = 0$ and $M = 0.5$, and $2g/\gamma = 10$, $2\kappa/\gamma = 0.1$	64
4.4	Spectra for Driving Field Intensities $N = 5$ and $M = 0$, and $2g/\gamma = 300$, $2\kappa/\gamma = 0.1$	69
5.1	Sample Quantum Trajectories Showing the Conditioned Upper State Probability of the Atom Undergoing Resonance Fluorescence	78
5.2	Waiting Time Distribution for Resonance Fluorescence Obtained from the Simulation of Fig. 5.1(a)	80
5.3	Waiting Time Distribution for Resonance Fluorescence Obtained from the Simulation of Fig. 5.1(b)	81
5.4	Sample Quantum Trajectories Based on Direct Photoelectron Detection Showing the Conditioned Mean Photon Number for a Degenerate Parametric Oscillator	86
5.5	Sample Quantum Trajectories Based on Homodyne Detection Showing the Conditioned Mean Photon Number for a Degenerate Parametric Oscillator	88
5.6	Sample Quantum Trajectories Based on Homodyne Detection Showing the Conditioned Mean Field Quadrature Amplitude for a Degenerate Parametric Oscillator	90
6.1	Energy-Level Diagram Showing the Excitation of the Lower “Vacuum” Rabi Resonance and the Resulting Dynamic Stark Splitting	93

6.2	Sample Quantum Trajectory	94
6.3	Approximate Two-State Saturation	97
6.4	Results of Simulated Photon Counting Measurements for $\gamma/2\kappa = 1$, $g/\kappa = 25$, and $\mathcal{E}/\kappa = 1$	99
6.5	Results of Simulated Photon Counting Measurements for $\gamma/2\kappa = 1$, $g/\kappa = 25$, and $\mathcal{E}/\kappa = 5$	100
6.6	Incoherent Spectrum of the Light Transmitted by the Cavity, $S_C(\omega)$, and Radiated by the Atom, $S_A(\omega)$	102
6.7	Open Quantum System B Cascades with a Quantum System A	105
6.8	Simulated Measurement of the Spectrum of the Light Transmitted by the Cavity	107
7.1	Wigner Distribution for the Superposition of Coherent States	111
7.2	Energy Levels of the Three-Level Atom Used to Generate a Schrödinger Cat State of the Optical Field	112
7.3	Model of the Schrödinger Cat inside the Cavity A Seen by the Detector in Homodyne Detection	118
7.4	Marginal Distribution Obtained from Eq. (7.34)	121
7.5	Two Sets of Distributions of the Integrated Photocurrent for Different Values of Intracavity Photon Numbers	123
7.6	Two Sets of Distributions of the Integrated Photocurrent for Different Values of Detection Efficiencies	124

CHAPTER I

INTRODUCTION

The field of cavity quantum electrodynamics (cavity QED) involves the study of atomic interactions with the electromagnetic field in a cavity. The earliest idea of cavity QED was pointed out by Purcell in 1946 [1]. He observed that the spontaneous emission rate from a two state system (a nuclear magnetic moment) coupled to an electrical circuit can be greatly enhanced. More than twenty years later, Drexhage made the first experimental demonstration of the alteration of spontaneous emission rates due to the presence of boundaries [2]. He observed a suppressed fluorescent decay rate for a dye molecule located close to a dielectric surface. The first experimental proof of Purcell's prediction was done by Goy *et al.* in 1983 [3]. They performed the experiment with Rydberg atoms (Na atoms) in a niobium superconducting resonant cavity and observed enhanced atomic spontaneous emission. Early experiments in cavity QED were performed with Rydberg atoms interacting with a single mode of a microwave cavity [3, 4]. In the last few years there have been several experiments in which the alteration of spontaneous emission rates has been observed in the optical frequency domain [5, 6, 7].

The enhancement and suppression of atomic spontaneous emission due to the presence of a boundary can be explained by first order perturbation theory (Fermi's golden rule). This theory states that the spontaneous emission rate is proportional

to the density of modes into which the excited-state atom may emit. In the presence of a cavity the mode density changes, which leads to an alteration of the spontaneous emission rate. The altered emission rate depends on the following three rates: the cavity damping rate κ , the spontaneous emission rate γ into continuum modes other than those of the cavity, and the atom-field coupling constant g , where g characterizes the oscillatory exchange of excitation between the atom and the field of the cavity.

Experiments on the enhancement and inhibition of spontaneous emission are performed in the regime of weak coupling $\kappa \gg g^2/\kappa \gg \gamma$. A nonperturbative atomic interaction with the cavity mode in the regime of strong coupling $g \gg \kappa, \gamma$ has been investigated in recent years within the context of cavity QED [3, 4, 8, 9, 10, 11]. Under these strong coupling conditions the photons emitted by the atom have a high probability to be reabsorbed before they are dissipated. The nonperturbative interaction can not be described from the viewpoint of the altered radiative process of the atom or cavity alone, but rather in terms of the dynamics of the composite atom-field entity. This composite atom-cavity system approaches the Jaynes-Cummings model of an atom coupled to a cavity mode with no dissipation [12]. One signature of the composite structure is the so-called “vacuum” Rabi splitting, which is the splitting of the degenerate *first excited state* of the uncoupled system (the atom in the ground state with one photon in the field, or the atom in the excited state with no photons in the field) due to the atom-cavity-mode interaction [13]. The splitting of these levels is $\pm g$ with one atom inside the cavity and $\pm\sqrt{N}g$ with N atoms inside the cavity.

“Vacuum” Rabi splitting is not an inherently quantum phenomenon and can also be understood from classical physics. It is essentially the normal mode splitting of coupled harmonic oscillators, one oscillator to describe the mean amplitude of the atomic polarization and the other to describe the mean amplitude of the single mode field inside the cavity. When an atom-cavity-mode system is weakly excited by coherent light the coupled harmonic oscillator picture comes very close to the physical reality [14, 15]. It also explains the “additional vacuum-field Rabi splittings” reported by Agarwal [16] for a system driven by a field with a stochastic phase [17]. It even explains the appearance of a doublet spectrum in spontaneous emission, in spite of the fact that an initially excited two-state atom is not, even approximately, a Lorentz oscillator. In this case it is the autocorrelation of the atomic polarization fluctuations that follows coupled harmonic oscillator dynamics, rather than the mean polarization amplitude itself [18].

There is a simple reason for the success of the classical coupled harmonic oscillator picture in explaining “vacuum” Rabi splitting. It is that the energy spectrum of the Jaynes-Cummings system is the same as that of coupled harmonic oscillators up to the first excited state. Thus, spectroscopic features that depend solely on transitions from the first excited state are indistinguishable between the two systems. But the systems are distinguished when we look at effects that involve transitions to higher excited states — for example, if we look at the intensity fluctuations observed in photon coincidence counting experiments [19, 11]. The systems are also distinguished

by direct spectroscopic measurement of transitions above the first excited state. For coupled harmonic oscillators the transition frequencies encountered at the first excited state are simply repeated, ad infinitum, at higher levels of excitation; the emission spectrum for coupled harmonic oscillators is characterized by a doublet at all levels of excitation. This is not so for the Jaynes-Cummings system. The level splittings for the Jaynes-Cummings Hamiltonian increase as the square root of the principal quantum number rather than in proportion to this number. Therefore, excitation above the first excited state introduces additional, incommensurate frequencies into the emission spectrum.

In the time domain the excited state splittings of an atom-cavity-mode system produce collapses and revivals of the semiclassical Rabi oscillations [20]. An experiment using Rydberg atoms in a microwave cavity has shown clear evidence of such quasiperiodic dynamics [9]. However, there have been no direct observations in the frequency domain of transitions between the excited states of an atom-cavity-mode system. In the microwave region such observations face the difficulty of detecting very weak (few quanta per mode) fields. At optical frequencies the difficulty is in achieving a sufficiently large dipole coupling strength. Some progress in this direction has been made. The “vacuum” Rabi spectrum for a collection of $N \gg 1$ atoms was observed in two experiments [14, 15], aided by the fact that the frequency splitting for many atoms is increased by the square root of the number of atoms. Very recently “vacuum” Rabi splitting was observed using a Cesium atomic beam with $\langle N \rangle \sim 1$

atom interacting with the cavity mode ($\langle N \rangle$ is the mean number of atoms) [11]. The challenge now is to observe transitions between the excited states of the composite system formed by a single atom strongly coupled to a resonant cavity mode. With the advent of laser cooling techniques and trap technology, it will be possible to perform quantum optical investigation on a single atom in the near future. In this thesis we investigate theoretically a single two-state atom strongly coupled to a single quantized mode of the electromagnetic field in an optical cavity in the strong coupling regime (atom-cavity-mode system).

The first topic of the thesis is to describe some excited-state spectroscopy of the atom-cavity-mode system that can differentiate between the quantum and classical models. Chapters II – IV are covered under this topic. In these three chapters we will describe three ways to observe the excited-state spectroscopy of the atom-cavity-mode system. The first is to inject laser light into an optical cavity containing a single two-state atom, and then to measure the intensity of the field transmitted from the cavity as a function of the frequency of the laser. This way of measuring transmission spectra follows the way in which measurements of the “vacuum” Rabi spectrum were made by Zhu *et al.* [15]. Calculations of such transmission spectra from both the QED and semiclassical theories are given in chapter II. The second is to measure the spectroscopic response of the atom-cavity-mode system to a cw pump laser plus weak, frequency tunable modulation. This way of observing excited-state spectroscopy exactly follows the way in which the nonlinear modulation spectrum of the

Jaynes-Cummings molecule was measured by Thompson *et al.* [21]. In chapter III we analyze a modulation spectroscopy scheme designed to reveal the first-to-second excited state transition of the Jaynes-Cummings model. We compare results of the QED and semiclassical calculations using parameters which are very close to those used in the experimental measurements [21]. We then identify and explain those features that distinguish the QED calculation from the semiclassical calculation. The final way to observe excited state transitions is to excite the strongly coupled atom and cavity mode system by broad-band chaotic light. The scattered, transmitted and reflected spectra corresponding to this way of measurement are calculated analytically and numerically in chapter IV. The analytical calculation of these spectra is based on the secular approximation which can be justified under strong coupling conditions. The excited-state spectra calculated in all these chapters do show the excited-state resonances of the Jaynes-Cummings system and provide a clear signature of the quantum nature of the atom-cavity-mode system.

Another feature showing the quantum character of the atom-cavity-mode system is two-state behavior of an optical cavity containing one atom. Indirectly, this too involves excited-state spectroscopy. Two-state behavior occurs because the energy levels of the coupled cavity mode and atom are unequally spaced, which, for sufficiently strong coupling allows a two-state approximation to be made. The two-state behavior is studied using a new method – the quantum trajectory method [22, 23, 24]. A stochastic wavefunction is introduced in this method to describe a source system

such as an atom-cavity-mode system. The stochastic wavefunction follows both the coherent quantum evolution of the system produced by the interaction between the atom and the cavity mode and incoherent evolution produced by atomic spontaneous emission and cavity loss. This new method provides a powerful computational tool; more importantly, it clarifies the physical interpretation. This method is reviewed in chapter V.

Chapter VI discusses the two-state behavior. In this study, we consider an atom-cavity-mode system driven by a laser. We tune the laser field to one of the “vacuum” Rabi resonances and observe the behavior of a single two-state system. In particular, we use the quantum trajectory method to show that the light transmitted by the cavity has the photoelectron counting statistics of resonance fluorescence and a Mollow-triplet spectrum for strong driving field intensities.

The final topic of the thesis is a study of Schrödinger cat states analyzed using the quantum trajectory method. Schrödinger cat states are superpositions of macroscopic quantum states. The generation of Schrödinger cat states is an issue of considerable importance in the study of the relationship between quantum and classical physics. It is found that the observation of these states is very difficult. This is because quantum coherence is destroyed by dissipation in the problem on a very fast time scale. For example, for a coherent state with amplitude α an energy decay rate 2κ is accompanied by a decay rate over short time intervals of $2\kappa|\alpha|^2$ for the interferences [25, 26].

In the field of optics, the interest in studying Schrödinger cat states began with a proposal for their generation by propagating a coherent state through a Kerr non-linear medium and observation by homodyne detection [27]. Use of a parametric amplifier to generate the states was also proposed [28, 29]. These schemes suffer the same difficulties with dissipation. Both explicit photon loss and inefficient detection contribute to the problem. The technical difficulties this raises are extreme, even for states that contain only two or three photons. There are also proposals for generating optical Schrödinger cats using a single atom [30, 31]. A number of these proposals involve the ideas of cavity QED [32, 33, 34]. The scheme we describe is similar in some respects to earlier proposals, but there are differences. Most previous proposals use dispersion to generate a superposition of phase-shifted coherent states from an initial coherent state. The absorption and emission of photons is explicitly avoided due to the problem with dissipation. In contrast, we generate the superposition of coherent states from the vacuum state; the photons it contains are emitted from an atom driven on resonance. Then there is a difference in the way we observe the Schrödinger cat. The original homodyne detection idea has been abandoned by those working in cavity QED. This is because a Schrödinger cat that lives inside a cavity is not accessible [33]; the problem of suitable detectors for microwave fields is also raised [32]. We will use, essentially, the original homodyne detection idea to observe the Schrödinger cat as it leaks out of the cavity.

Like everyone else, we find that photon loss is a practical difficulty. However, we

view the loss not just as something to be avoided, but as something first to be understood. By using the quantum trajectory approach we can see exactly how the loss destroys the quantum interference. The important thing we find is that, in principle, negative effects of the loss can be eliminated by adding a “spontaneous emission veto” while preparing the Schrödinger cat; in practice the effects of the loss can certainly be decreased. Most importantly, we find that the cavity loss involved in leaking a prepared Schrödinger cat out to an external detector does not necessarily destroy the detected interference pattern. The only requirement is that the local oscillator be temporally mode matched to the decaying signal. The generation of Schrödinger cat states and the observation of these states using temporal-mode-matched homodyne detector are described in chapter VII (We note that our study will deal with few-photon cats, not truly macroscopic ones.).

CHAPTER II

COHERENT EXCITATION: TRANSMISSION SPECTROSCOPY

The ‘vacuum’ Rabi spectrum shows the transitions between the first excited state and ground state of a coupled atom-cavity-mode system. This double-peaked spectrum has been observed in a number of experiments [11, 14, 15]. There remains, however, some motivation for going beyond these experiments because they do not distinguish between the results of QED calculations and those of semiclassical calculations. Spectra that show features associated with the excited-state resonances of the coupled atom-cavity-mode system do distinguish between the QED theory and the semiclassical theory. In chapters II – IV, we study the excited-state spectroscopy of this system. This chapter and chapter III consider coherent excitation of a coupled system of a single atom plus a single mode of the cavity field in the strong coupling regime. Chapter IV will consider incoherent excitation. In this chapter transmission spectra are presented. The standard semiclassical theory is reviewed and the corresponding QED theory is described. For increasing field strengths the spectra calculated from the semiclassical theory develop bistability on the ‘vacuum’ Rabi peaks. In contrast, the spectra calculated from the QED theory develop a series of multi-photon resonances.

2.1 Optical Bistability

We consider an optical cavity, open at the sides, containing a single two-level atom. The atom is resonant with one mode of the cavity at frequency ω_0 . The cavity is illuminated by a coherent field with frequency ω_L . The system is depicted in Figure 2.1. In the rotating wave approximation, the semiclassical Maxwell-Bloch equations for the coupled atom-cavity-mode system can be written as [35]

$$\begin{aligned}
 \frac{d\langle\hat{a}'\rangle}{dt} &= -(\kappa + i\omega_0)\langle\hat{a}'\rangle + g\langle\hat{\sigma}'_-\rangle + \mathcal{E}exp(-i\omega_L t), \\
 \frac{d\langle\hat{\sigma}'_-\rangle}{dt} &= -(\gamma/2 + i\omega_0)\langle\hat{\sigma}'_-\rangle + g\langle\hat{a}'\rangle\langle\hat{\sigma}_z\rangle, \\
 \frac{d\langle\hat{\sigma}_z\rangle}{dt} &= -\gamma(\langle\hat{\sigma}_z\rangle + 1) - 2g(\langle\hat{a}'\rangle\langle\hat{\sigma}'_-\rangle^* + \langle\hat{a}'\rangle^*\langle\hat{\sigma}'_-\rangle).
 \end{aligned}
 \tag{2.1}$$

Here $\langle\hat{a}'\rangle$ is the amplitude of the field inside the cavity, $\langle\hat{\sigma}'_-\rangle$ is the atomic polarization, and $\langle\hat{\sigma}_z\rangle$ is the atomic population difference; \mathcal{E} is the amplitude of the coherent driving field, $\gamma/2$ and κ are the atomic linewidth and cavity linewidth (half-width at half-maximum), respectively, and g is the atom-field coupling constant. The optical frequencies ω_0 and ω_L are very much larger than all the other rates, \mathcal{E} , g , γ , κ in our system. To remove the fast time dependence in Eqs. (2.1) we make the transformation

$$\langle\hat{a}'\rangle = \langle\hat{a}\rangle exp(-i\omega_L t), \quad \langle\hat{\sigma}'_-\rangle = \langle\hat{\sigma}_-\rangle exp(-i\omega_L t).
 \tag{2.2}$$

We then have the semiclassical Maxwell-Bloch equations for the coupled atom-cavity-mode system in a frame rotating at the frequency ω_L

$$\frac{d\langle\hat{a}\rangle}{dt} = -(\kappa + i\Delta)\langle\hat{a}\rangle + g\langle\hat{\sigma}_-\rangle + \mathcal{E},$$

$$\frac{d\langle\hat{\sigma}_-\rangle}{dt} = -(\gamma/2 + i\Delta)\langle\hat{\sigma}_-\rangle + g\langle\hat{a}\rangle\langle\hat{\sigma}_z\rangle, \quad (2.3)$$

$$\frac{d\langle\hat{\sigma}_z\rangle}{dt} = -\gamma(\langle\hat{\sigma}_z\rangle + 1) - 2g(\langle\hat{a}\rangle\langle\hat{\sigma}_-\rangle^* + \langle\hat{a}\rangle^*\langle\hat{\sigma}_-\rangle),$$

with $\Delta = \omega_0 - \omega_L$.

For weak driving fields we write $\langle\hat{\sigma}_z\rangle = -1$ and the first two of Eqs. (2.3) reduce to

$$\begin{aligned} \frac{dX}{dt} &= -(\kappa + i\Delta)X + gY + \mathcal{E}, \\ \frac{dY}{dt} &= -(\gamma/2 + i\Delta)Y - gX, \end{aligned} \quad (2.4)$$

with $X \leftrightarrow \langle\hat{a}\rangle$ and $Y \leftrightarrow \langle\hat{\sigma}_-\rangle$. These are coupled harmonic oscillator equations [36]. The eigenvalues for these equations are $\pm i\sqrt{g^2 - (\kappa - \gamma/2)^2/4} - i\Delta - \frac{1}{2}(\kappa + \gamma/2)$, which shows the two normal mode frequencies of the oscillators. The semiclassical oscillator model based on Eqs. (2.4) has been used to explain experimental observations of “vacuum” Rabi splitting, eventhough the name “vacuum” Rabi splitting suggests a phenomenon with a quantum-mechanical origin. “Vacuum” Rabi splitting does not distinguish between the results of the QED calculations and those of the semiclassical calculations; extension of the “vacuum” Rabi spectrum to strong driving fields will do this. The rest of this section presents the semiclassical results for such an extension. The QED calculations will be discussed in the next section.

For a fixed amplitude of the driving field we calculate the intensity of the field transmitted by the cavity as a function of the detuning of the driving field from the resonance frequency of the atom and cavity mode. This way of calculating spectra

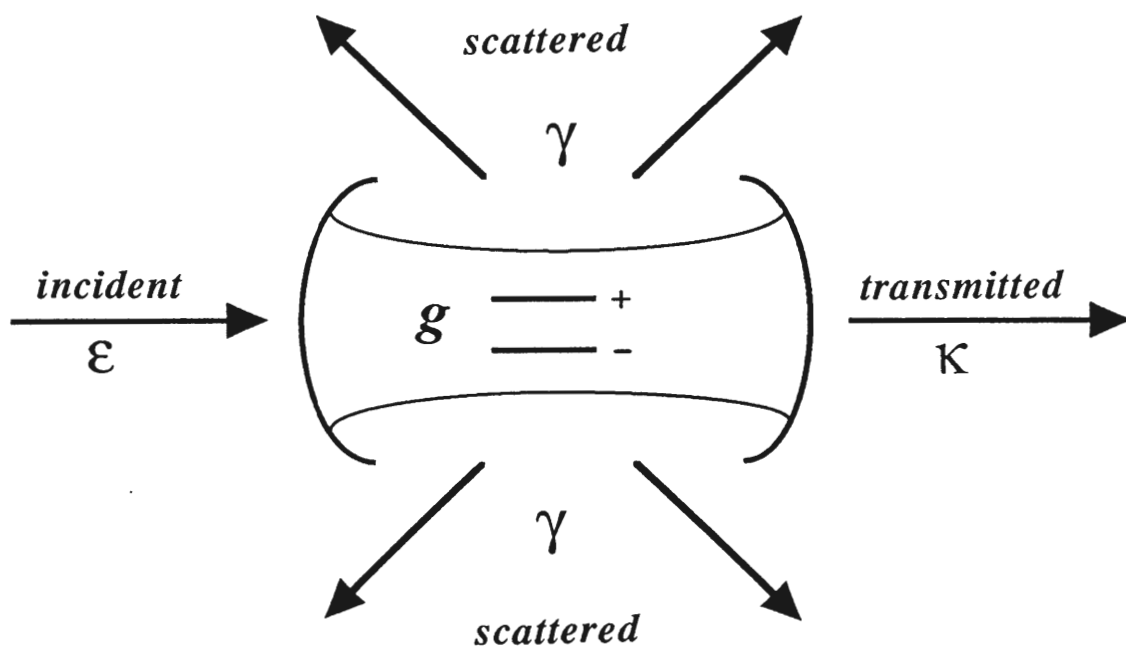


Figure 2.1. Schematic diagram of a single atom in a cavity driven by a coherent field.

follows one of the ways in which measurements of the “vacuum” Rabi spectrum were made [15, 37]. The calculations are performed by solving for the steady-state photon number $|\langle\hat{a}\rangle_{ss}|^2$ inside the cavity using the Maxwell-Bloch Eqs. (2.3). The resulting relationship between $|\langle\hat{a}\rangle_{ss}|^2$ and the driving field intensity \mathcal{E}^2 is the state equation of absorptive and dispersive optical bistability [38], which reads as

$$n_{\text{sat}}^{-1}(\mathcal{E}/\kappa)^2 = n_{\text{sat}}^{-1}|\langle\hat{a}\rangle_{ss}|^2 \left[\left(1 + \frac{2C}{1 + \delta^2 + n_{\text{sat}}^{-1}|\langle\hat{a}\rangle_{ss}|^2} \right)^2 + \left(\frac{\gamma\delta}{2\kappa} - \frac{2C\delta}{1 + \delta^2 + n_{\text{sat}}^{-1}|\langle\hat{a}\rangle_{ss}|^2} \right)^2 \right], \quad (2.5)$$

where $\delta = 2\Delta/\gamma$ is the detuning in units of the atomic linewidth, $C = Ng^2/\gamma\kappa$ is the cooperativity parameter, and $n_{\text{sat}} = \gamma^2/8g^2$ is the saturation photon number.

Eq. (2.5) shows optical bistability which comes from the combination of non-linearity in the response of the atom together with the feedback inherent in the intracavity geometry. The nonlinearity of the atom results from a combination of intensity-dependent absorption and dispersion; the former entering in the term $2C/(1 + \delta^2 + n_{\text{sat}}^{-1}|\langle\hat{a}\rangle_{ss}|^2)$ of Eq. (2.5) and the latter in $2C\delta/(1 + \delta^2 + n_{\text{sat}}^{-1}|\langle\hat{a}\rangle_{ss}|^2)$. Feedback is provided by enclosing the atom in the cavity. Eq. (2.5) has received a great deal of attention in the past [38, 39, 40]. In spite of this, our present study uncovers a previously unrecognized connection between bistability and the “vacuum” Rabi splitting. Figures 2.2 and 2.3 show the transmitted spectra calculated from Eq. (2.5). Here the transmitted spectrum means the amplitude of the field transmitted by the cavity – proportional to $|\langle\hat{a}\rangle_{ss}|$ – as a function of the detuning of the driving

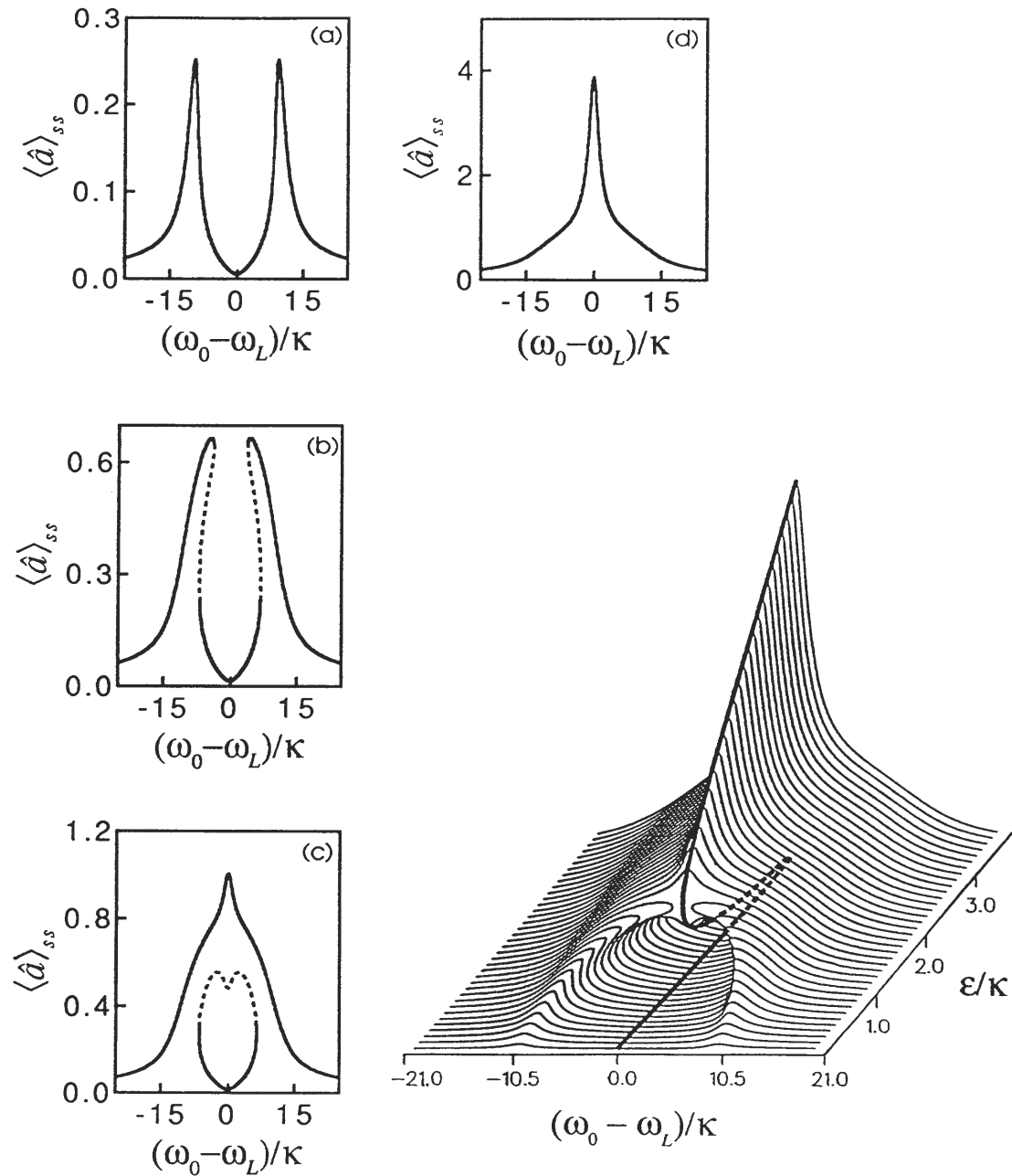


Figure 2.2. The transmission spectrum calculated from the semiclassical theory, plotted as a function of driving field amplitude for $g/\kappa = 10$, $\gamma/2\kappa = 1$: (a) $\mathcal{E}/\kappa = 0.5$, (b) $\mathcal{E}/\kappa = 1.0$, (c) $\mathcal{E}/\kappa = 1.5$, (d) $\mathcal{E}/\kappa = 4.0$. The dashed parts of the curves are unstable. The S-shaped curve of absorptive bistability is shown by the dark line in the three-dimensional picture.

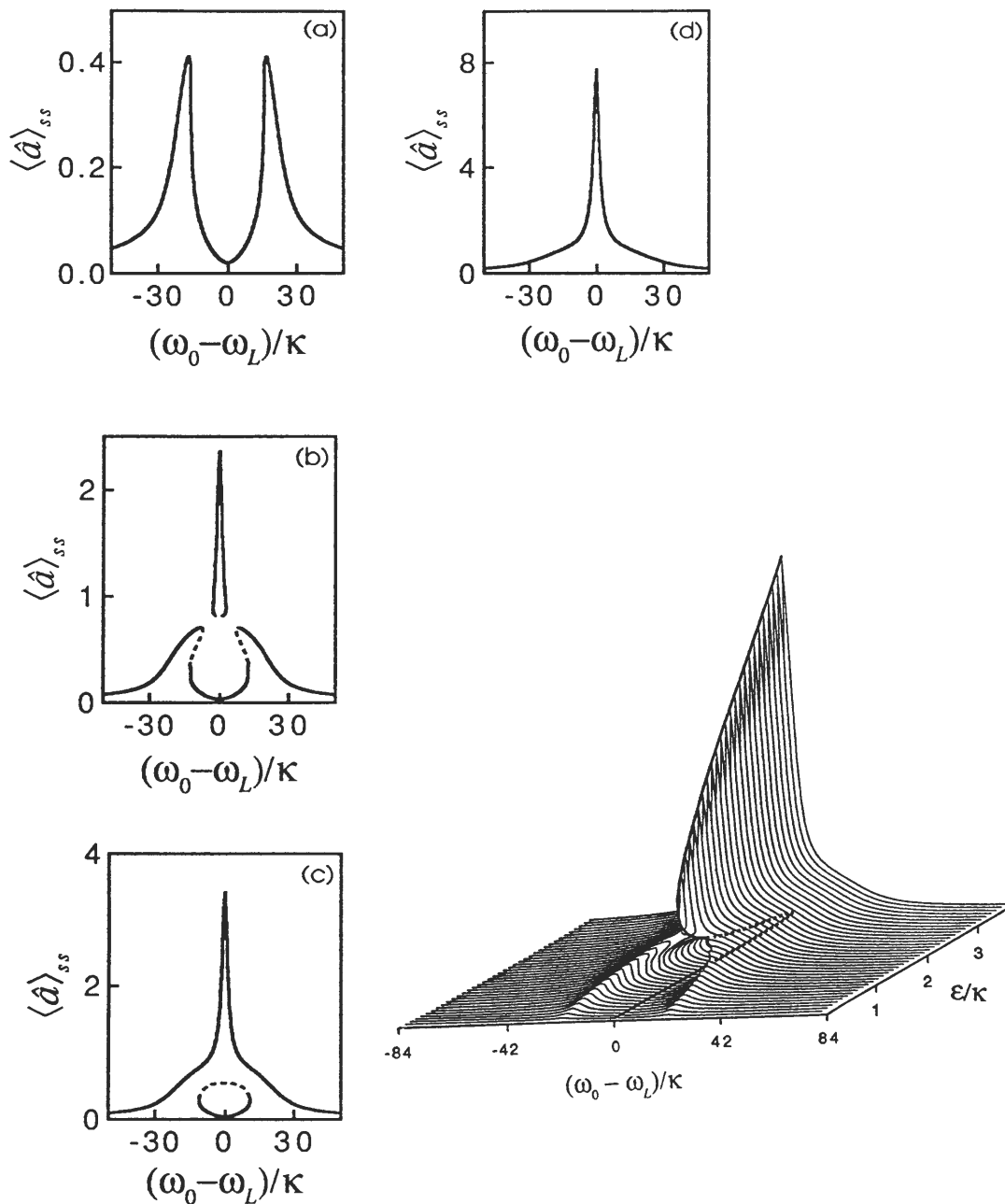


Figure 2.3. The transmission spectrum calculated from the semiclassical theory, plotted as a function of driving field amplitude for $g/\kappa = 20$, $\gamma/2\kappa = 4$: (a) $\mathcal{E}/\kappa = 1.2$, (b) $\mathcal{E}/\kappa = 1.6$, (c) $\mathcal{E}/\kappa = 2.0$, (d) $\mathcal{E}/\kappa = 4.0$. The dashed parts of the curves are unstable. The S-shaped curve of absorptive bistability is shown by the dark line in the three-dimensional picture.

field δ . The three-dimensional pictures plot the spectra versus the amplitude of the driving field \mathcal{E} . For weak driving fields the double-peaked “vacuum” Rabi spectrum is shown. When the intensity of the driving field is increased, however, the “vacuum” Rabi spectrum evolves into a one-peaked spectrum, passing through a bistable region along the way. The more familiar view of optical bistability is obtained by varying the optical field amplitude at a fixed frequency detuning, as shown by the S-shaped curve in the three-dimensional pictures.

2.2 Multi-photon Transitions

In the last section we treated the interaction between the atom and the cavity mode semiclassically. Under strong coupling conditions, however, an atom coupled to a mode of the cavity field is not just an atom in a cavity field. It is a composite atom-cavity-mode structure, like a “molecule”. In this case the semiclassical approximation cannot be justified. The interaction between the atom and cavity mode needs to be treated quantum mechanically. In this section we consider the quantum-mechanical treatment and make a comparison of the transmitted spectra with those of the semiclassical calculations to see how the composite nature is revealed. The starting point of such calculations is from a microscopic model for the atom-cavity-mode system. In the rotating-wave and dipole approximations, the microscopic model is given by the operator master equation [41, 42, 43, 44]

$$\dot{\rho}' = (1/i\hbar) [\hat{H}_{JC}, \rho'] + \mathcal{E} [\hat{a}^\dagger \exp(-i\omega_L t) - \hat{a} \exp(i\omega_L t), \rho']$$

$$+ (\gamma/2) (2\hat{\sigma}_- \rho' \hat{\sigma}_+ - \hat{\sigma}_+ \hat{\sigma}_- \rho' - \rho' \hat{\sigma}_+ \hat{\sigma}_-) + \kappa (2\hat{a} \rho' \hat{a}^\dagger - \hat{a}^\dagger \hat{a} \rho' - \rho' \hat{a}^\dagger \hat{a}), \quad (2.6)$$

where ρ' is the reduced density operator for the model system, and

$$\hat{H}_{JC} = \hbar\omega_0 (\hat{a}^\dagger \hat{a} + \hat{\sigma}_z/2) + i\hbar g (\hat{a}^\dagger \hat{\sigma}_- - \hat{a} \hat{\sigma}_+) \quad (2.7)$$

is the on resonance Jaynes-Cummings Hamiltonian [12] describing the interaction between the atom and the cavity mode; \hat{a}^\dagger and \hat{a} are the field creation and annihilation operators for the cavity mode and satisfy the boson commutation relation $[\hat{a}, \hat{a}^\dagger] = 1$, $\hat{\sigma}_+$ and $\hat{\sigma}_-$ are raising and lowering operators for the atom, obeying the pseudospin commutation relations $[\hat{\sigma}_+, \hat{\sigma}_-] = 2\hat{\sigma}_z$, $[\hat{\sigma}_\pm, \hat{\sigma}_z] = \mp\hat{\sigma}_\pm$. The second term on the right-hand side of Eq. (2.6) describes the interaction of the cavity mode with the injected laser field, the third describes spontaneous emission from the atom out the sides of the cavity, and the fourth describes loss through the cavity mirrors.

The Jaynes-Cummings Hamiltonian (2.7) defines the composite atom-cavity-mode system; the rest of the model is there to excite the system and provides the linewidths. The energy spectrum of the atom-cavity-mode system is defined by the eigenvalues of the Jaynes-Cummings Hamiltonian, with

$$\begin{aligned} E_g &= -(1/2)\hbar\omega_0, \\ E_{n,u} &= \hbar [\omega_0(n - 1/2) + \sqrt{n} g], \\ E_{n,l} &= \hbar [\omega_0(n - 1/2) - \sqrt{n} g]. \end{aligned} \quad (2.8)$$

The corresponding eigenstates are

$$|g\rangle = |0\rangle|-\rangle,$$

$$|n, u\rangle = (1/\sqrt{2})(|n-1\rangle|+\rangle + i|n\rangle|-\rangle), \quad (2.9)$$

$$|n, l\rangle = (1/\sqrt{2})(|n-1\rangle|+\rangle - i|n\rangle|-\rangle),$$

where $n = 1, 2, \dots$. Here $|+\rangle$ and $|-\rangle$ are the upper and lower atomic states, and $|n\rangle$ denotes the n photon Fock state of the field. States (2.9) have been referred to as dressed states [45]. We will extensively use the dressed-state representation throughout this work. The one-photon transition frequencies $(E_{1,u} - E_g)/\hbar = \omega_0 + g$ and $(E_{1,l} - E_g)/\hbar = \omega_0 - g$ locate the peaks of the “vacuum” Rabi spectrum, which can be explained by both quantum-mechanical and semiclassical models. We will obtain spectra that show evidence of the multi-photon transitions which quantum mechanics is responsible for.

We transform Eq. (2.6) to the interaction picture by defining $\rho' = U\rho U^\dagger$, where $U = \exp[-i(\hat{a}^\dagger\hat{a} + \hat{\sigma}_z/2)\omega_L t]$. We then obtain the master equation in a frame rotating at frequency ω_L

$$\begin{aligned} \dot{\rho} &= \mathcal{L}\rho \\ &= -i\Delta [\hat{a}^\dagger\hat{a} + \hat{\sigma}_z/2, \rho] + \mathcal{E} [\hat{a}^\dagger - \hat{a}, \rho] + g [\hat{a}^\dagger\hat{\sigma}_- - \hat{a}\hat{\sigma}_+, \rho] \\ &\quad + (\gamma/2)(2\hat{\sigma}_-\rho\hat{\sigma}_+ - \hat{\sigma}_+\hat{\sigma}_-\rho - \rho\hat{\sigma}_+\hat{\sigma}_-) + \kappa(2\hat{a}\rho\hat{a}^\dagger - \hat{a}^\dagger\hat{a}\rho - \rho\hat{a}^\dagger\hat{a}). \end{aligned} \quad (2.10)$$

Before solving this master equation, let us see how the quantum-mechanical equations connect to the coupled harmonic oscillator model. From Eq. (2.10) the mean-value equations can be obtained, with

$$\frac{d\langle\hat{a}\rangle}{dt} = -(\kappa + i\Delta)\langle\hat{a}\rangle + g\langle\hat{\sigma}_-\rangle + \mathcal{E},$$

$$\frac{d\langle\hat{\sigma}_-\rangle}{dt} = -(\gamma/2 + i\Delta)\langle\hat{\sigma}_-\rangle + g\langle\hat{\sigma}_z\hat{a}\rangle, \quad (2.11)$$

$$\frac{d\langle\hat{\sigma}_z\rangle}{dt} = -\gamma(\langle\hat{\sigma}_z\rangle + 1) - 2g\langle\hat{a}^\dagger\hat{\sigma}_-\rangle - 2g\langle\hat{\sigma}_+\hat{a}\rangle.$$

For weak driving fields we may use the truncated basis $|0\rangle|-\rangle$, $|0\rangle|+\rangle$, $|1\rangle|-\rangle$, in which $\hat{a} \equiv (|0\rangle|-\rangle)\langle\langle-|\langle 1|)$ and $\hat{\sigma}_z\hat{a} \equiv -\frac{1}{2}(|0\rangle|-\rangle)\langle\langle-|\langle 1|)$; then $\langle\hat{\sigma}_z\hat{a}\rangle = -\langle\hat{a}\rangle/2$ and the first two of Eqs. (2.11) reduce to Eqs. (2.4) with the correspondence $X \leftrightarrow \langle\hat{a}\rangle$, $Y \leftrightarrow \langle\hat{\sigma}_-\rangle$. Note that Eqs. (2.11) and (2.3) are also related, the latter following from the former after we factorize the averages of operator products. This is a good approximation for a many-atom system in which the quantum fluctuations are small, but not for a one-atom system where the quantum fluctuations are large [46].

Now with respect to the recent experiments on “vacuum” Rabi splitting, the three sets of equations, (2.3), (2.4) and (2.11), have the following significance: Eqs. (2.4) model all the experiments [14, 37, 15] [the model based on linear dispersion theory [15] is the frequency-space version of Eqs. (2.4)]. For the experiments with many atoms [14, 15] the route to Eqs. (2.4) starts from Eqs. (2.3) rewritten as the many-atom version of the Maxwell Bloch equations

$$\begin{aligned} \frac{d\langle\hat{a}\rangle}{dt} &= -(\kappa + i\Delta)\langle\hat{a}\rangle + g\langle\hat{J}_-\rangle + \mathcal{E}, \\ \frac{d\langle\hat{J}_-\rangle}{dt} &= -(\gamma/2 + i\Delta)\langle\hat{J}_-\rangle + g\langle\hat{J}_z\rangle\langle\hat{a}\rangle, \\ \frac{d\langle\hat{J}_z\rangle}{dt} &= -\gamma(\langle\hat{J}_z\rangle + N) - 2g(\langle\hat{a}^\dagger\rangle\langle\hat{J}_-\rangle + \langle\hat{J}_+\rangle\langle\hat{a}\rangle), \end{aligned} \quad (2.12)$$

where \hat{J}_+ , \hat{J}_- , and \hat{J}_z are collective operators describing a system of N atoms. For

weak driving fields we write $\langle \hat{J}_z \rangle = -N$ and the first two of Eqs. (2.12) reduce to Eqs. (2.4) with $X \leftrightarrow \langle \hat{a} \rangle$, $Y \leftrightarrow \langle \hat{J}_- \rangle / \sqrt{N}$, $g \leftrightarrow \sqrt{N}g$. For the experiment with one atom [37] the route to Eqs. (2.4) starts from Eqs. (2.11). Thus, the classical coupled oscillator model explains “vacuum” Rabi splitting as observed in these experiments so far, and at the level of the qualitative physics it does not distinguish between the QED and the semiclassical calculations. If, however, we consider the nonlinear regime (strong driving fields) the prediction of Eqs. (2.11) will disagree with that of Eqs. (2.3). The spectra calculated from the QED theory will not develop optical bistability on the “vacuum” Rabi peaks as the semiclassical theory does. We demonstrate this in the following.

Eqs. (2.11) do not form a closed set; in fact, they are part of an infinite set of equations. To obtain a closed set of equations we have to truncate the Fock-state basis. We truncated the Fock-state basis (at $n \sim 20$) and solved the master equation in steady state by direct matrix inversion. The method is limited to relatively small photon numbers, but is adequate for making a comparison with the semiclassical results. Fig. 2.4 show the transmission spectrum of the QED calculation. The QED result is completely different from the bistable result obtained from the semiclassical theory. The absence of any evidence for bistability is not a surprise since there cannot be multiple solutions in a plot of the true *mean* photon number (In the semiclassical calculation, the fluctuations of the system have not been considered.). In fact the average over the two branches of solutions of the Maxwell-Bloch equations probably

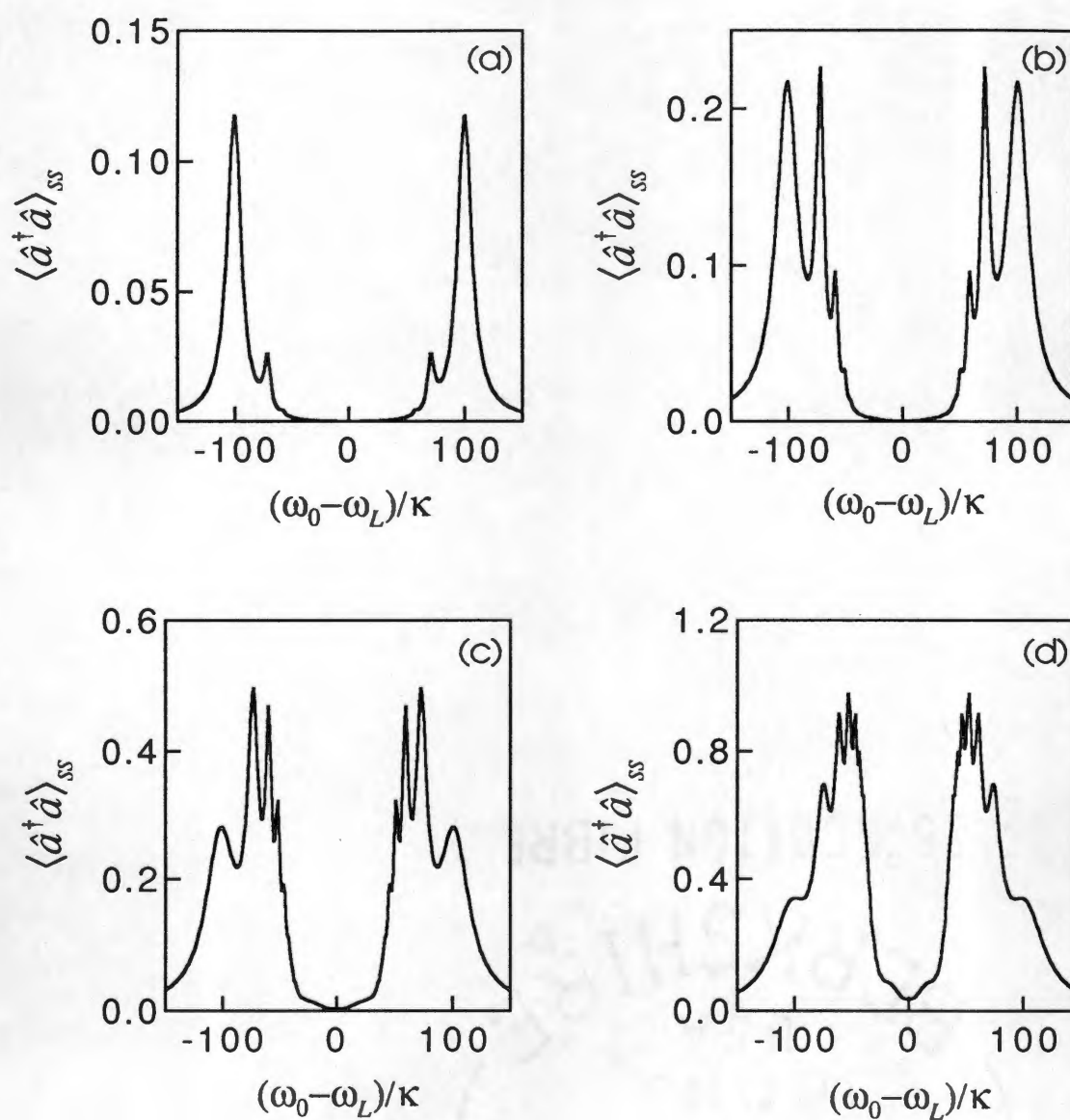


Figure 2.4. The transmission spectrum calculated from the QED theory for $g/\kappa = 100$, $\gamma/2\kappa = 10$: (a) $\mathcal{E}/\kappa = 5$, (b) $\mathcal{E}/\kappa = 10$, (c) $\mathcal{E}/\kappa = 15$, (d) $\mathcal{E}/\kappa = 20$.

lies close to the result of the QED calculation through most of the detuning range shown in Fig. 2.5, even very close to resonance where the upper branch of solutions is metastable [38]. The most notable difference in the QED result is the presence of additional resonances in between the “vacuum” Rabi peaks. These are multi-photon resonances caused by the absorption of two, three, or four photons at once. Fig. 2.6 shows the transitions responsible for these resonances. The resonance frequencies can be calculated from Eqs. (2.8). They satisfy the condition ($n = 1, 2, \dots$)

$$n\hbar\omega_{L,n} = \hbar\omega_0(n - 1/2) \pm \hbar\sqrt{n}g + \hbar\omega_0/2 \Rightarrow \omega_{L,n} - \omega_0 = \pm g/\sqrt{n} \quad (2.13)$$

The formula $\omega_{L,n} - \omega_0 = \pm g/\sqrt{n}$ matches the positions of the peaks in Fig. 2.4 very well.

The one-photon resonances are the “vacuum” Rabi resonances that are mimicked by classical coupled harmonic oscillators. The higher resonances provide a clear signature of the quantum nature of the coupled atom and cavity mode. They cannot be reproduced by either classical or semiclassical coupled oscillator models. The positions of these resonances are determined by the level structure of the atom-cavity “molecule,” a structure that can only be obtained by quantizing both the atom and the cavity mode.

As mentioned above, the quantum-mechanical correspondance of bistability cannot be evidenced in a plot of the mean photon number. Savage and Carmichael [47] have demonstrated that it may be evidenced by a bimodality in a plot of the time evolution for the probability distribution of the mean photon number. For a

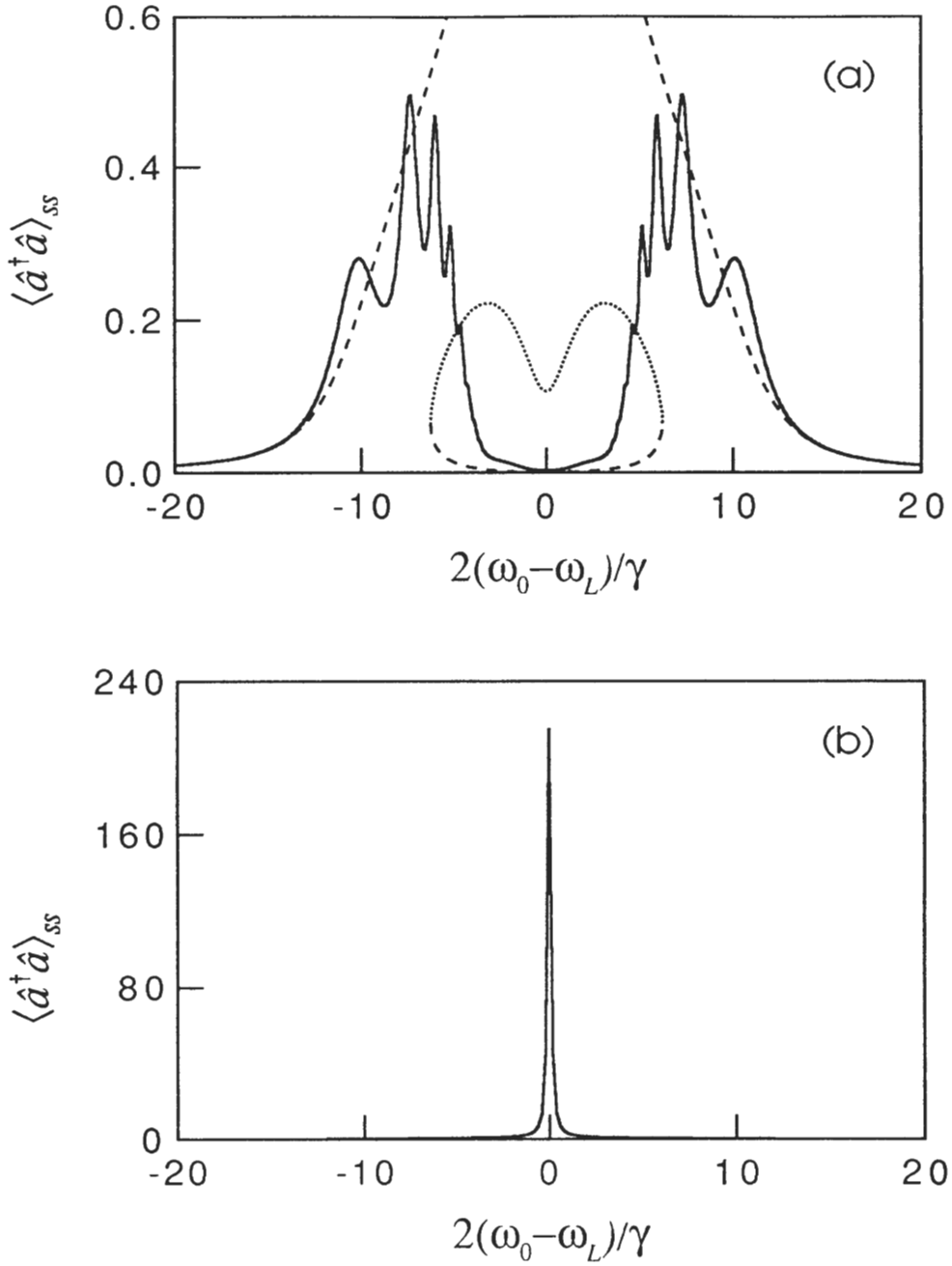


Figure 2.5. Transmission spectra for $g/\kappa = 100$, $\gamma/2\kappa = 10$, and $\mathcal{E}/\kappa = 15$: (a) Comparison of semiclassical (dashed and dotted lines) and QED results. The dotted line is unstable. (b) Continuation of the upper (metastable) transmission curve near resonance obtained from the semiclassical theory.

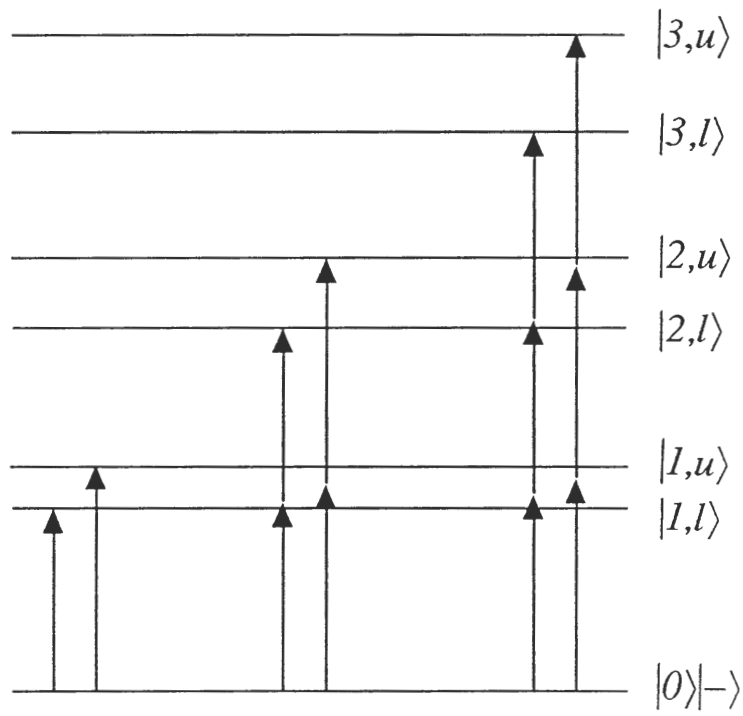


Figure 2.6. Energy-level diagram for the Jaynes-Cummings Hamiltonian showing multi-photon transitions. The one photon resonances produce the vacuum Rabi peaks, and the two-photon and three-photon resonances produce the additional peaks, as shown in Fig. 2.4.

saturation photon number n_{sat} on the order of at least 1, they observed a distinctly bimodal distribution consistent with the semiclassical prediction of coexisting strong absorption, low photon number (unsaturated atom), and weak absorption, high photon number (saturated atom) states. Of course, the two states identified with the two peaks in the photon number distribution are not strictly bistable at the level of quantum noise. Bistability is a macroscopic phenomenon reached in the limit $n_{\text{sat}} \rightarrow \infty$. However, with increasing n_{sat} , switching times become longer and the peaks of photon number distribution approaches to the semiclassical states. In the regime considered in this dissertation, the saturation photon number n_{sat} is much smaller than unity. Thus, a bimodality cannot be seen in the probability distribution of the mean photon number; quantum fluctuations completely destroy the bistable behavior shown in the semiclassical results.

Two final notes about Figure 2.5 are given here. First, on comparing Figs. 2.5(a) and 2.5(b) we see an incredible reduction in mean photon number in the QED result. The ratio g/κ is rather extreme in the figure, but quite remarkable reductions also occur for more moderate ratios. Second, strong coupling conditions $g \gg \kappa, \gamma/2$ are necessary for seeing multi-photon transitions clearly.

CHAPTER III

COHERENT EXCITATION: MODULATION SPECTROSCOPY

In the previous chapter we considered a coupled atom-cavity-mode system driven by a coherent field and studied the transmission spectra of such a system. We found that the semiclassical calculation exhibits bistable behavior and the quantum-mechanical calculation shows completely different behavior – multi-photon transitions – under strong coupling conditions. Strong coupling conditions as extreme as those considered in the previous chapter, however, have not been realized in the current experiments at optical frequencies. The motivation of the study in this chapter is to observe the excited-state transition of the coupled system under the conditions that current experiments can realize. We study the spectroscopic response of the atom-cavity-mode system to a cw coherent pump plus weak, frequency tunable modulation. We analyze a modulation spectroscopy scheme designed to reveal the first-to-second excited-state transition as proposed recently in a cavity QED experiment [21]. We perform both quantum-mechanical and semiclassical calculations of modulation spectra using parameters which are very close to those realized in this experiment. Results of the QED and the semiclassical calculations are compared and those features that distinguish the QED calculation from the semiclassical calculation are identified and explained. Under extreme strong coupling conditions, analytic expressions for the spectra are obtained.

3.1 Modulation Spectroscopy Scheme

We consider a coupled atom-cavity-mode system as before. But in this chapter the system we consider is driven by a weak, single sideband modulated optical field (pump field plus probe field)

$$\mathcal{E}(t) = [\mathcal{E} + \mathcal{E}' \exp(-i\nu t)] \exp(-i\omega_L t) + \text{c.c.}, \quad (3.1)$$

where c.c. denotes the complex conjugate. The amplitude of the pump field is much larger than the amplitude of the probe field, $\mathcal{E} \gg \mathcal{E}'$, and the frequency of the pump field is tuned to the lower “vacuum” Rabi resonance $\omega_L = \omega_0 - g$. The strong pump field drives the coupled system up to the one of the first excited states, and then the weak probe field probes the transmission of the coupled system as a function of the modulation frequency ν . Thus a fingerprint of the first-to-second excited-state transition is written on the modulation spectrum.

We first describe the modulation spectroscopy scheme based on the QED theory, and then describe that based on the semiclassical theory. In the QED approach, our model system is described by the master equation (in a frame rotating at ω_L)

$$\dot{\rho}(t) = \mathcal{L}\rho(t) + \mathcal{L}'\rho(t), \quad (3.2)$$

where $\mathcal{L}\rho(t)$ is given by Eq. (2.10), and

$$\mathcal{L}'\rho(t) = \mathcal{E}' \left[\hat{a}^\dagger \exp(-i\nu t) - \hat{a} \exp(i\nu t), \rho(t) \right] \quad (3.3)$$

is due to the presence of the probe field. We write the density operator in the form

$$\rho(t) = \rho_{ss} + \rho'(t), \quad (3.4)$$

where ρ_{ss} satisfies

$$\dot{\rho}_{ss} = \mathcal{L}\rho_{ss} = 0. \quad (3.5)$$

From Eqs. (3.2), (3.4) and (3.5), we obtain

$$\dot{\rho}(t) = (\mathcal{L} + \mathcal{L}')\rho'(t) + \mathcal{L}'\rho_{ss}. \quad (3.6)$$

In the limit of very weak modulation, we can drop the term $\mathcal{L}'\rho'(t)$ and have

$$\dot{\rho}'(t) = \mathcal{L}\rho'(t) + \mathcal{E}' \exp(-i\nu t)[\hat{a}^\dagger, \rho_{ss}] + \mathcal{E}' \exp(i\nu t)[\rho_{ss}, \hat{a}]. \quad (3.7)$$

Since we only detect the transmitted field from the cavity with the same frequency as that of the input probe field, instead of solving Eq. (3.7) we only need to solve the equation

$$\dot{\rho}'(t) = \mathcal{L}\rho'(t) + \mathcal{E}' \exp(-i\nu t)[\hat{a}^\dagger, \rho_{ss}]. \quad (3.8)$$

For fast computation, we consider a perturbation to the steady state which contains all of the probe frequencies needed at once, i.e. we integrate $\exp(-i\nu t)$ with respect to the modulation frequency ν and have

$$\dot{\rho}'(t) = \mathcal{L}\rho'(t) + \mathcal{E}'\delta(t)[\hat{a}^\dagger, \rho_{ss}]. \quad (3.9)$$

Eq. (3.9) taken with the initial condition $\rho'(0) = 0$, is equivalent to the equation

$$\dot{\rho}'(t) = \mathcal{L}\rho'(t), \quad (3.10)$$

with the initial condition

$$\rho'(0) = \mathcal{E}'[\hat{a}^\dagger, \rho_{ss}]. \quad (3.11)$$

The modulation spectrum of the transmitted cavity field is then given by the equation

$$S(\omega) = \left| \int_{-\infty}^{\infty} dt \exp(i\omega t) \langle \hat{a}'(t) \rangle \right|^2, \quad (3.12)$$

where

$$\langle \hat{a}'(t) \rangle = \text{tr} (\hat{a}\rho'(t)) / \mathcal{E}' \quad (3.13)$$

is the perturbation of the transmitted cavity field amplitude driven by \mathcal{E}' , which can be calculated from Eqs. (3.10) and (3.11).

Let us now describe the modulation spectroscopy scheme based on the semiclassical theory. Our model system is described by the Maxwell-Bloch equations (in a frame rotating of ω_L)

$$\begin{aligned} \langle \dot{\hat{a}} \rangle &= -(\kappa + i\Delta)\langle \hat{a} \rangle + g\langle \hat{\sigma}_- \rangle + \mathcal{E} + \mathcal{E}' \exp(-i\nu t), \\ \langle \dot{\hat{a}}^\dagger \rangle &= -(\kappa - i\Delta)\langle \hat{a}^\dagger \rangle + g\langle \hat{\sigma}_+ \rangle + \mathcal{E} + \mathcal{E}' \exp(i\nu t), \\ \langle \dot{\hat{\sigma}}_- \rangle &= -(\gamma/2 + i\Delta)\langle \hat{\sigma}_- \rangle + g\langle \hat{a} \rangle \langle \hat{\sigma}_z \rangle, \\ \langle \dot{\hat{\sigma}}_+ \rangle &= -(\gamma/2 - i\Delta)\langle \hat{\sigma}_+ \rangle + g\langle \hat{a}^\dagger \rangle \langle \hat{\sigma}_z \rangle, \\ \langle \dot{\hat{\sigma}}_z \rangle &= -\gamma(\langle \hat{\sigma}_z \rangle + 1) - 2g(\langle \hat{a}^\dagger \rangle \langle \hat{\sigma}_- \rangle + \langle \hat{a} \rangle \langle \hat{\sigma}_+ \rangle). \end{aligned} \quad (3.14)$$

Eqs. (3.14) can be written as the compact vector equation

$$\dot{\vec{x}} = \vec{f}(\vec{x}) + \mathcal{E}' \exp(-i\nu t) \vec{e}_1 + \mathcal{E}' \exp(i\nu t) \vec{e}_2, \quad (3.15)$$

with

$$\vec{x} = \begin{pmatrix} \langle \hat{a} \rangle \\ \langle \hat{a}^\dagger \rangle \\ \langle \hat{\sigma}_- \rangle \\ \langle \hat{\sigma}_+ \rangle \\ \langle \hat{\sigma}_z \rangle \end{pmatrix}, \quad \vec{e}_1 = \begin{pmatrix} 1 \\ 0 \\ 0 \\ 0 \\ 0 \end{pmatrix}, \quad \vec{e}_2 = \begin{pmatrix} 0 \\ 1 \\ 0 \\ 0 \\ 0 \end{pmatrix}. \quad (3.16)$$

Let us write \vec{x} in the form

$$\vec{x} = \vec{x}_{ss} + \vec{x}', \quad (3.17)$$

where \vec{x}_{ss} satisfies

$$\dot{\vec{x}}_{ss} = \vec{f}(\vec{x}_{ss}) = 0. \quad (3.18)$$

With Eqs. (3.17) and (3.18), Eq. (3.15) now reads as

$$\dot{\vec{x}}' = \left(\frac{d\vec{f}}{d\vec{x}} \Big|_{\vec{x}=\vec{x}_{ss}} \right) \vec{x}' + \mathcal{E}' \exp(-i\nu t) \vec{e}_1 + \mathcal{E}' \exp(i\nu t) \vec{e}_2. \quad (3.19)$$

Here we have made a Taylor series expansion of $\vec{f}(\vec{x}_{ss} + \vec{x}')$ and kept only the first order term. This is because the perturbation from the steady state is very small due to very weak modulation. As mentioned in the QED calculation, we only need one of the two frequency components; thus we only need to solve the equation

$$\dot{\vec{x}}' = \left(\frac{d\vec{f}}{d\vec{x}} \Big|_{\vec{x}=\vec{x}_{ss}} \right) \vec{x}' + \mathcal{E}' \exp(-i\nu t) \vec{e}_1. \quad (3.20)$$

We calculate the transmitted spectrum in the same way as in the QED approach.

We integrate $\exp(-i\nu t)$ with respect to modulation frequency ν and have

$$\dot{\vec{x}}' = \left(\frac{d\vec{f}}{d\vec{x}} \Big|_{\vec{x}=\vec{x}_{ss}} \right) \vec{x}' + \mathcal{E}' \delta(t) \vec{e}_1. \quad (3.21)$$

Eq. (3.21) is equivalent to the following equation

$$\dot{\vec{x}}' = \left(\frac{d\vec{f}}{d\vec{x}} \Big|_{\vec{x}=\vec{x}_{ss}} \right) \vec{x}' = M \vec{x}', \quad (3.22)$$

with initial condition $\vec{x}'(0) = \mathcal{E}' \vec{e}_1$. Here we have defined the matrix

$$M = \begin{pmatrix} -(ig + \kappa) & 0 & g & 0 & 0 \\ 0 & ig - \kappa & 0 & g & 0 \\ g\langle \hat{\sigma}_z \rangle_{ss} & 0 & -(ig + \gamma/2) & 0 & g\langle \hat{a} \rangle_{ss} \\ 0 & g\langle \hat{\sigma}_z \rangle_{ss} & 0 & ig - \gamma/2 & g\langle \hat{a} \rangle_{ss}^* \\ -2g\langle \hat{\sigma}_- \rangle_{ss}^* & -2g\langle \hat{\sigma}_- \rangle_{ss} & -2g\langle \hat{a} \rangle_{ss}^* & -2g\langle \hat{a} \rangle_{ss} & \gamma \end{pmatrix}. \quad (3.23)$$

From the solution of Eq. (3.22), the modulation spectrum of the transmitted cavity field can be calculated using Eq. (3.12).

3.2 Numerical Results for Modulation Spectra

Following the schemes we described in the last section, we have calculated modulation spectra numerically from both the QED and the semiclassical theories. The

parameters we have used here are very close to those realized in current experiments. We first show the result of the modulation spectrum calculated from the QED theory. Fig. 3.1 shows how the spectrum changes as the intensity of the pump field is changed. For a very weak pump field, the spectrum exhibits a two-peaked structure corresponding to the familiar “vacuum” Rabi splitting. With increasing intensity of the pump field, Figs. 3.1(a) and 3.1(b) show that the intensity of the transmitted field at the lower “vacuum” Rabi resonance $\omega - \omega_L = 0$ becomes lower than that at the upper “vacuum” Rabi resonance $\omega - \omega_L = 2g$, and a new peak at the frequency $\omega - \omega_L = (2 - \sqrt{2})g$ appears in between the “vacuum” Rabi peaks. The new resonance corresponds to the transition to the first excited state from the second excited states of the Jaynes-Cummings Hamiltonian ($|2, l\rangle \rightarrow |1, l\rangle$). These features are due to the absorption of the pump field tuned to the lower “vacuum” Rabi resonance. These resonances are illustrated in Fig. 3.2. In Figs. 3.1(c), 3.1(d) and 3.1(e), as the intensity of the pump field is increased further, the intensity of the transmitted cavity field at frequency $\omega - \omega_L = (2 - \sqrt{2})g$ increases, and a complicated structure appears around the lower “vacuum” Rabi resonance which comes from the pump-probe spectroscopy of a two-state transition, as done originally by Mollow [48]. Note that a doublet appears around the upper “vacuum” Rabi resonance. This is due to dynamic Stark splitting (shown in Fig. 3.2). When extremely strong coupling conditions are approached, the peaks in the spectrum are well separated compared to their widths (shown in Figs. 3.3 and 3.4). Fig. 3.4 shows us the clear structure around the lower

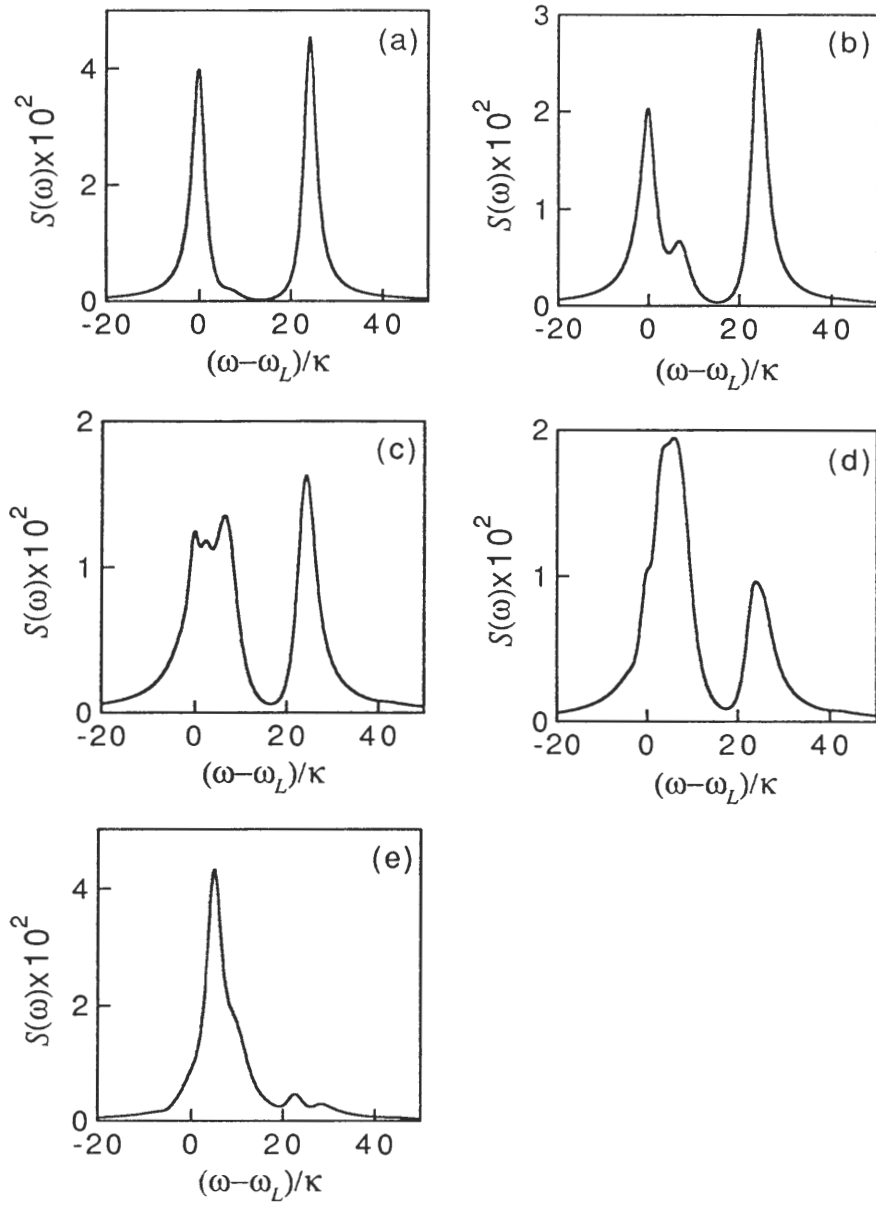


Figure 3.1. The modulation spectrum calculated from the QED theory for $g/\kappa = 12$, $2g/\gamma = 5.6$: (a) $\mathcal{E}/\kappa = 0.5$, (b) $\mathcal{E}/\kappa = 1.0$, (c) $\mathcal{E}/\kappa = 1.5$, (d) $\mathcal{E}/\kappa = 2.0$, (e) $\mathcal{E}/\kappa = 4.0$.

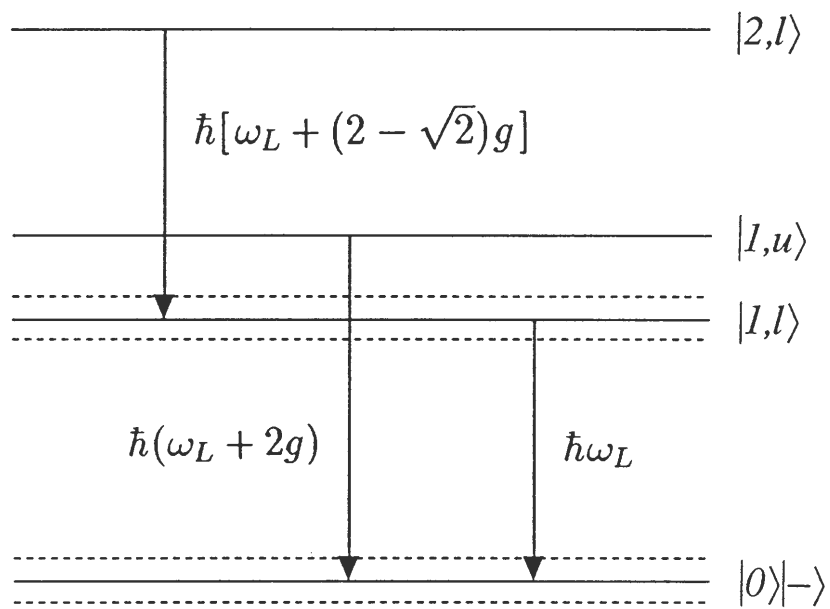


Figure 3.2. Energy-level diagram for an atom-cavity-mode system. The dashed lines show the dynamic Stark splitting induced by a laser tuned to the lower “vacuum” Rabi resonance.

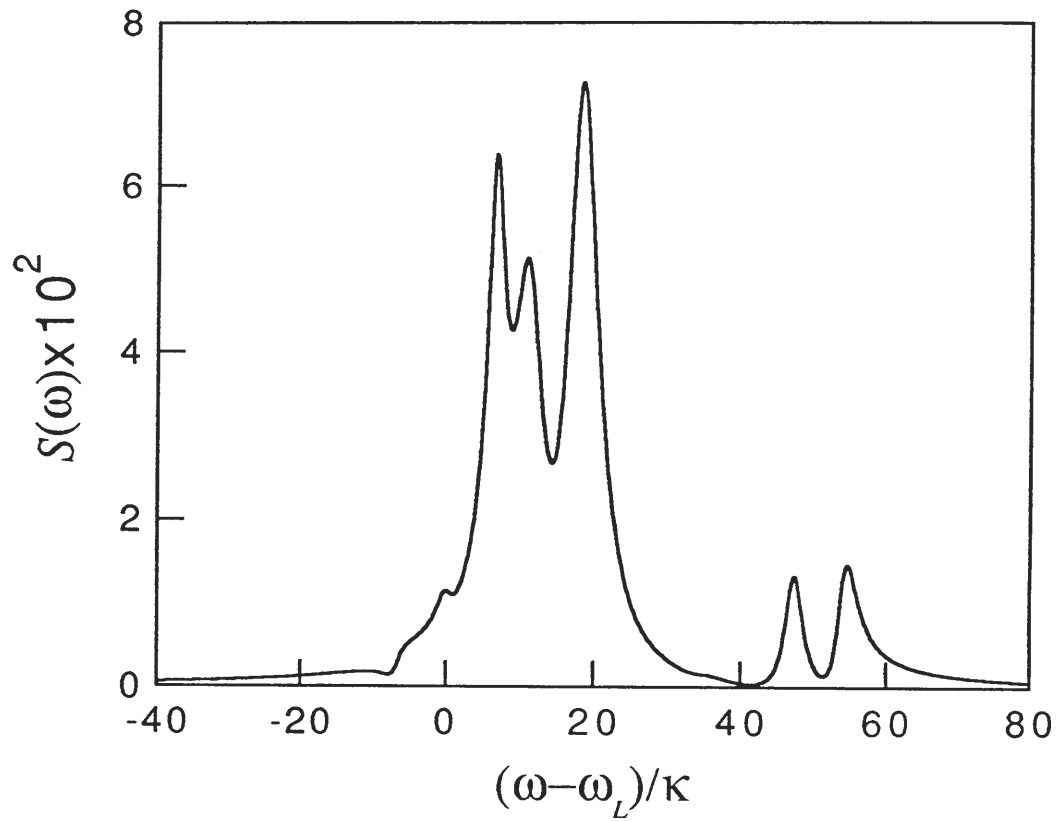


Figure 3.3. The modulation spectrum calculated from the QED theory for $g/\kappa = 25$, $\gamma/2\kappa = 1$, and $\mathcal{E}/\kappa = 5$.

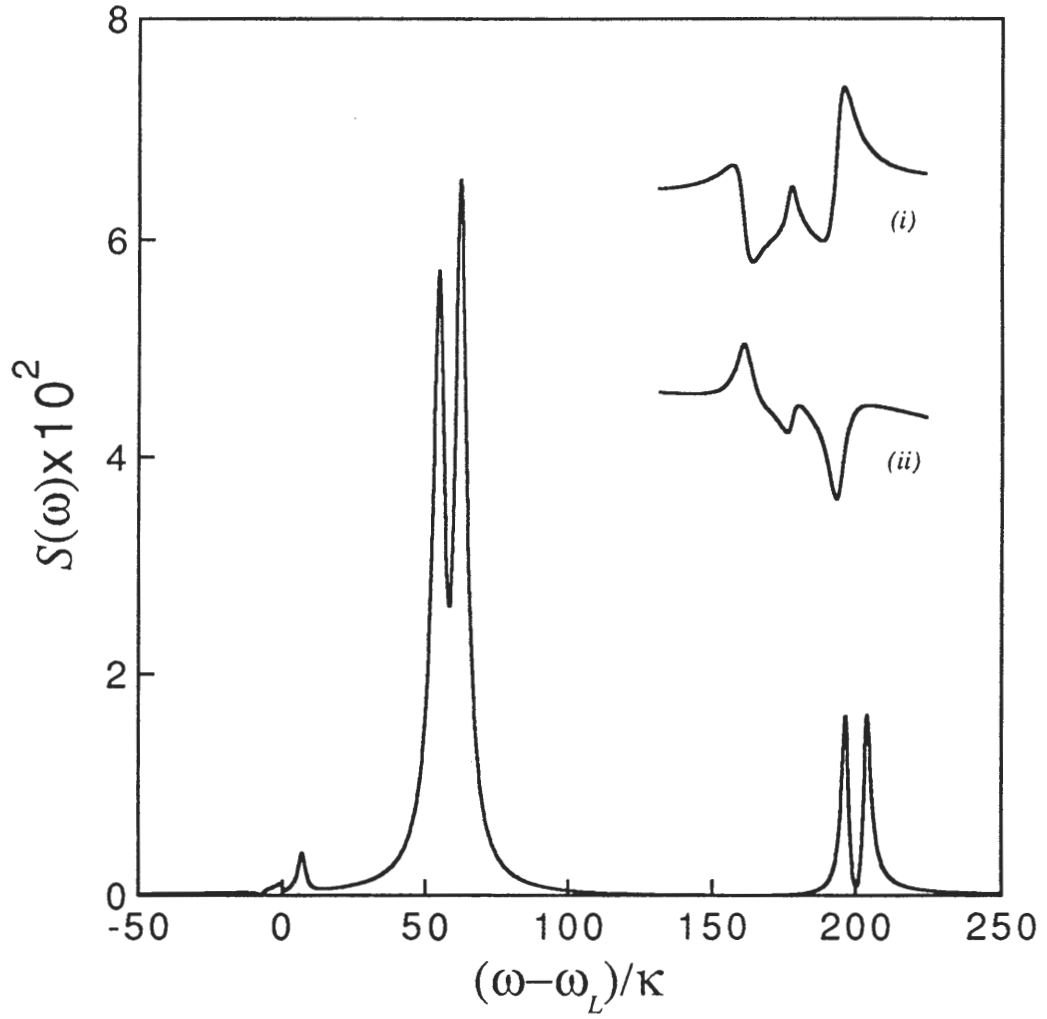


Figure 3.4. The modulation spectrum calculated from the QED theory for $g/\kappa = 100$, $\gamma/2\kappa = 1$, and $\mathcal{E}/\kappa = 5$. The spectrum around the lower “vacuum” Rabi resonance is blown up – the two curves (i) and (ii) in the upper right corner show the real and imaginary parts of the amplitude of the transmitted cavity field, respectively.

“vacuum” Rabi resonance, the doublet around the upper “vacuum” Rabi resonance, and the new resonance in between the “vacuum” Rabi resonance due to the first-to-second excited-state transition. The spectrum around the lower “vacuum” Rabi resonance is blown up – the two curves in the upper right corner show the real and imaginary parts of the amplitude of the transmitted cavity field as a function of probe frequency, respectively. They exhibit the familiar structures shown in Mollow’s paper [48].

For a very strong pump field, the spectrum has a one-peaked structure, with the peak located at the resonance frequency ω_0 of the cavity mode. This corresponds to the spectroscopic response of the empty cavity to a weak probe field.

We now show the results of the modulation spectrum calculated from the semi-classical theory. For comparison, Fig. 3.5 is plotted with the same parameters as Fig. 3.1. For a very weak pump field, the same two-peaked “vacuum” Rabi spectrum is obtained. But the spectrum changes dramatically with increasing the intensity of the pump field. Fig. 3.5 shows that the height of the left peak in the spectrum located around the lower “vacuum” Rabi resonance is always higher than that of the right peak around the upper “vacuum” Rabi resonance, and the new resonance in between the “vacuum” Rabi resonances never shows up. It also shows that the position of the peaks is moving as the intensity of the pump field is increased. This is due to the dispersion which comes from that the presence of the atom inside the cavity is accounted for by a nonlinear susceptibility. For a very strong pump field, the same

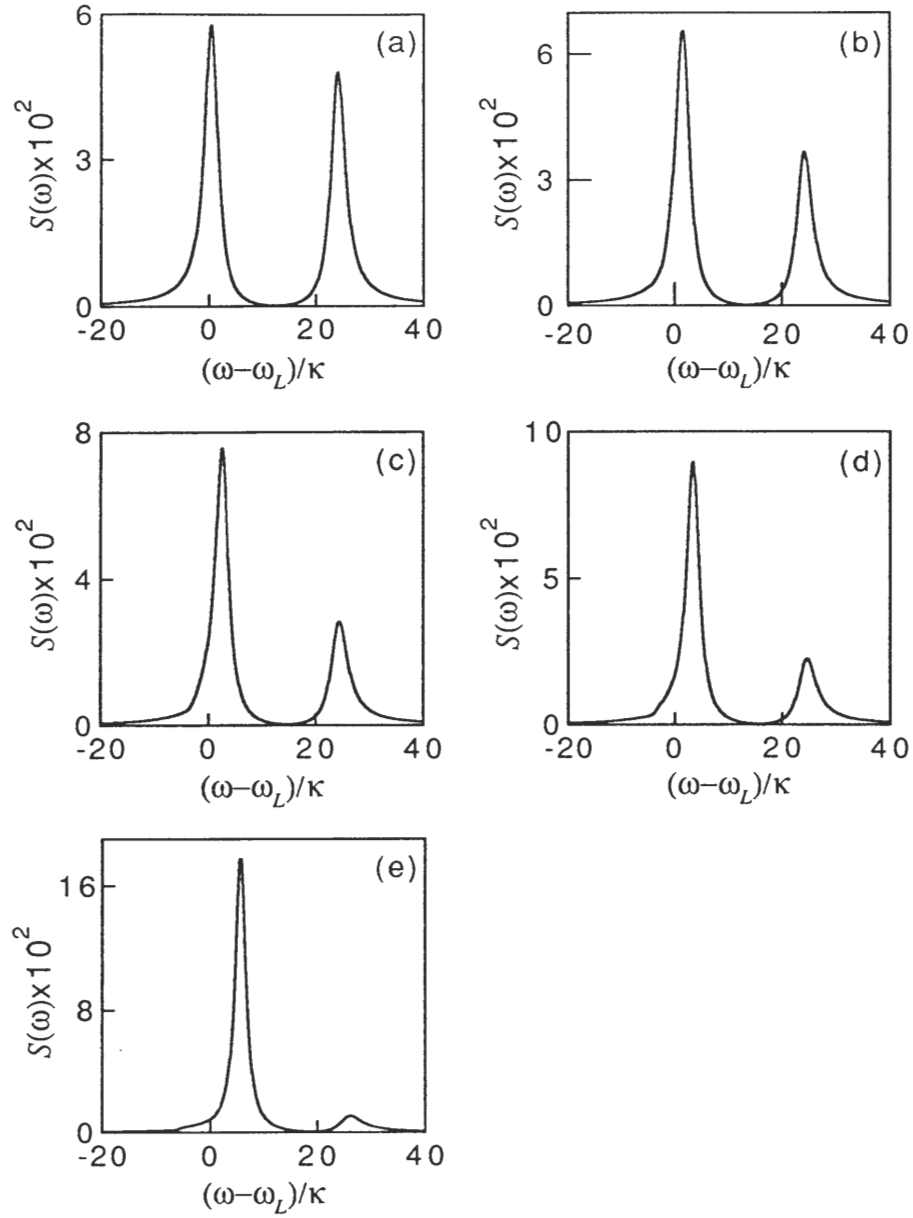


Figure 3.5. The modulation spectrum calculated from the semiclassical theory for $g/\kappa = 12$, $2g/\gamma = 5.6$: (a) $\mathcal{E}/\kappa = 0.5$, (b) $\mathcal{E}/\kappa = 1.0$, (c) $\mathcal{E}/\kappa = 1.5$, (d) $\mathcal{E}/\kappa = 2.0$, (e) $\mathcal{E}/\kappa = 4.0$.

one-peaked spectrum is obtained.

Those features that distinguish the QED calculation from the semiclassical calculation provide a clear signature of the quantum nature of the coupled atom-cavity-mode system. In the next two sections, we will show the analytical calculations from both the QED and the semiclassical theories. In general one can not calculate these modulation spectra analytically. Under extremely strong coupling conditions, however, an analytical calculation is possible.

3.3 Analytical Results of the QED Calculation

To perform an analytical calculation, we consider very weak excitation and the extremely strong coupling condition $g \gg \kappa, \gamma/2$. This condition allows us to solve the master equation (3.10) using the secular approximation [45]. We make the transformation

$$\bar{\rho} = \exp(i\hat{H}t/\hbar)\rho' \exp(-i\hat{H}t/\hbar), \quad (3.24)$$

where

$$\hat{H} = \hbar g(\hat{a}^\dagger \hat{a} + \hat{\sigma}_z/2) + i\hbar g(\hat{a}^\dagger \hat{\sigma}_- - \hat{a} \hat{\sigma}_+), \quad (3.25)$$

and drop all the oscillatory terms in the transformed master equation (secular approximation). In the limit of very weak excitation we may use the truncated five dressed-state basis $|g\rangle, |1, l\rangle, |1, u\rangle, |2, l\rangle, |2, u\rangle$. In general there should be twenty-five matrix elements of $\bar{\rho}$ for five-state basis. But here many of them are zero. The

non-zero matrix elements of $\bar{\rho}$ satisfy the following equations:

$$\begin{aligned}\dot{\bar{\rho}}_g &= -2\alpha\bar{\rho}_g + i\Omega(\bar{\rho}_{1,l;g} - \bar{\rho}_{g;1,l}), \\ \dot{\bar{\rho}}_{g;1,l} &= -\alpha\bar{\rho}_{g;1,l} - 2i\Omega\bar{\rho}_g, \\ \dot{\bar{\rho}}_{1,l;g} &= -\alpha\bar{\rho}_{1,l;g} + 2i\Omega\bar{\rho}_g,\end{aligned}\tag{3.26}$$

where

$$\alpha = \frac{1}{2}(\kappa + \gamma/2), \quad \Omega = \mathcal{E}/\sqrt{2},\tag{3.27}$$

$\bar{\rho}_g = \langle g|\bar{\rho}|g\rangle$, $\bar{\rho}_{1,l} = \langle 1, l|\bar{\rho}|1, l\rangle$, $\bar{\rho}_{1,l;g} = \langle 1, l|\bar{\rho}|g\rangle$, $\bar{\rho}_{g;1,l} = \langle g|\bar{\rho}|1, l\rangle$, and we have used $\bar{\rho}_g + \bar{\rho}_{1,l} = 0$;

$$\dot{\bar{\rho}}_{1,u;g} = -\alpha\bar{\rho}_{1,u;g},\tag{3.28}$$

where $\bar{\rho}_{1,u;g} = \langle 1, u|\bar{\rho}|g\rangle$;

$$\begin{aligned}\dot{\bar{\rho}}_{2,\eta;g} &= -\beta_1\bar{\rho}_{2,\eta;g} - i\Omega\bar{\rho}_{2,\eta;1,l}, \\ \dot{\bar{\rho}}_{2,\eta;1,l} &= -\beta_2\bar{\rho}_{2,\eta;1,l} - i\Omega\bar{\rho}_{2,\eta;g},\end{aligned}\tag{3.29}$$

where $\beta_1 = \frac{1}{2}(3\kappa + \gamma/2)$, $\beta_2 = 2\kappa + \gamma/2$, $\bar{\rho}_{2,\eta;g} = \langle 2, \eta|\bar{\rho}|g\rangle$, $\bar{\rho}_{2,\eta;1,l} = \langle 2, \eta|\bar{\rho}|1, l\rangle$, $\eta = u, l$. We Fourier transform Eqs. (3.26) – (3.29) and obtain the following solutions by using Eqs. (3.24) and (3.25):

$$\begin{aligned}F_{1,l;g}(\nu) &= \frac{\rho'_{1,l;g}(0)[2(\alpha^2 + \Omega^2) - \nu^2 - 3i\alpha\nu] + 2i\Omega\rho'_g(0)(\alpha - i\nu)}{(\alpha - i\nu)[2(\alpha^2 + 2\Omega^2) - \nu^2 - 3i\alpha\nu]}, \\ F_{1,u;g}(\nu) &= \frac{\rho'_{1,u;g}(0)}{[\alpha - i(\nu - 2g)]}, \\ F_{2,\eta;1,l}(\nu) &= \frac{-i\Omega\rho'_{2,\eta;g}(0) + \rho'_{2,\eta;1,l}(0)[\beta_1 + i(\nu - \nu_{2,\eta;1,l})]}{\Omega^2 + [\beta_2 + i(\nu - \nu_{2,\eta;1,l})][\beta_1 + i(\nu - \nu_{2,\eta;1,l})]},\end{aligned}\tag{3.30}$$

where $\eta = u, l$, $\nu_{2,l;1,l} = (2 - \sqrt{2})g$, $\nu_{2,u;1,l} = (2 + \sqrt{2})g$, and

$$F_{i,j}(\nu) = \int_0^\infty dt \exp(i\nu t) \rho'_{i,j}(t), \quad i(j) = g; 1, l; 1, u; 2, l; 2, u. \quad (3.31)$$

Here $\rho'_{i,j}(0)$ may be calculated in terms of the steady state solution, ρ_{ss} , of the master equation (3.10). As we know, under strong coupling conditions the coupled atom-cavity-mode system behaves like a two-state system [49]. Thus, there are only four non-zero matrix elements of the steady state density operator ρ_{ss}

$$\begin{aligned} (\rho_g)_{ss} &= 2(\alpha^2 + \Omega^2)/\zeta, & (\rho_{1,l})_{ss} &= 2\Omega^2/\zeta, \\ (\rho_{g;1,l})_{ss} &= -2i\alpha\Omega/\zeta, & (\rho_{1,l;g})_{ss} &= 2i\alpha\Omega/\zeta, \end{aligned} \quad (3.32)$$

where $\zeta = 2(\alpha^2 + 2\Omega^2)$. With Eqs. (3.32) and (3.11), we find

$$\begin{aligned} \rho'_g(0) &= -\sqrt{2}\alpha\Omega/\zeta, & \rho'_{1,l;g}(0) &= i\sqrt{2}\alpha^2/\zeta, \\ \rho'_{2,l;1,l}(0) &= (1 + \sqrt{2})\Omega^2/\zeta, & \rho'_{2,l;g}(0) &= i(1 + \sqrt{2})\alpha\Omega/\zeta, \\ \rho'_{1,u;g}(0) &= -i\sqrt{2}(\alpha^2 + \Omega^2)/\zeta, & \rho'_{2,u;g}(0) &= i(1 - \sqrt{2})\alpha\Omega/\zeta, \\ \rho'_{2,u;1,l}(0) &= (1 - \sqrt{2})\Omega^2/\zeta. \end{aligned} \quad (3.33)$$

Now the perturbation of the transmitted cavity field amplitude may be expressed as

$$\begin{aligned} \langle \hat{a}'(t) \rangle &= \text{tr}(\hat{a}\rho')/\mathcal{E}' \\ &= \frac{i}{\sqrt{2}}\rho'_{1,u;g}(t) - \frac{i}{\sqrt{2}}\rho'_{1,l;g}(t) + \left(\frac{1}{2} + \frac{1}{\sqrt{2}}\right)\rho'_{2,l;1,l}(t) + \left(\frac{1}{2} - \frac{1}{\sqrt{2}}\right)\rho'_{2,u;1,l}(t). \end{aligned} \quad (3.34)$$

From Eq. (3.12) the modulation spectrum is then written as

$$S(\nu) = \left| \frac{1}{\sqrt{2}} F_{1,u;g}(\nu) - \frac{1}{\sqrt{2}} F_{1,l;g}(\nu) + \left(\frac{1}{2} + \frac{1}{\sqrt{2}} \right) F_{2,l;1,l}(\nu) + \left(\frac{1}{2} - \frac{1}{\sqrt{2}} \right) F_{2,u;1,l}(\nu) \right|^2. \quad (3.35)$$

Using Eqs. (3.30), (3.33) and (3.35), we calculate $S(\nu)$. Extremely strong coupling conditions assume that the peaks in the spectrum may be well separated. Thus, we have

$$\begin{aligned} S(\nu = 0) &= \frac{1}{2} |F_{1,l;g}(\nu = 0)|^2 = \frac{\alpha^6}{4(\alpha^2 + 2\Omega^2)^4}, \\ S(\nu = 2g) &= \frac{1}{2} |F_{1,u;g}(\nu = 2g)|^2 = \frac{(\alpha^2 + \Omega^2)^2}{4\alpha^2(\alpha^2 + 2\Omega^2)^2}, \\ S(\nu = \nu_{2,l;1,l}) &= \left(\frac{1}{2} + \frac{1}{\sqrt{2}} \right)^2 |F_{2,l;1,l}(\nu = \nu_{2,l;1,l})|^2 = \frac{(1 + \sqrt{2})^4 \Omega^4 (\beta_1 + \alpha)^2}{16(\alpha^2 + 2\Omega^2)^2 (\Omega^2 + \beta_1 \beta_2)^2}, \\ S(\nu = \nu_{2,u;1,l}) &= \left(\frac{1}{2} - \frac{1}{\sqrt{2}} \right)^2 |F_{2,u;1,l}(\nu = \nu_{2,u;1,l})|^2 = \frac{(1 - \sqrt{2})^4 \Omega^4 (\beta_1 + \alpha)^2}{16(\alpha^2 + 2\Omega^2)^2 (\Omega^2 + \beta_1 \beta_2)^2}. \end{aligned} \quad (3.36)$$

These equations clearly show that a new peak appears in between the “vacuum” Rabi resonances, located at frequency $\nu_{2,l;1,l}$, and also that the peak located at frequency $\nu_{2,u;1,l}$ can hardly be seen because of the relatively small value of $S(\nu = \nu_{2,u;1,l})$. The ratio of the intensity of the transmitted cavity field at the lower “vacuum” Rabi resonance to that at the upper “vacuum” Rabi resonance is

$$\frac{S(\nu = 0)}{S(\nu = 2g)} = \left[\left(1 + \mathcal{E}^2 / 2\alpha^2 \right)^2 \left(1 + \mathcal{E}^2 / \alpha^2 \right)^2 \right]^{-1} \leq 1. \quad (3.37)$$

Eq. (3.37) indicates that the intensity of the transmitted cavity field at the lower “vacuum” Rabi resonance is lower than that at the upper “vacuum” Rabi resonance when the pump field is turned on. This agrees with Fig. 3.3.

3.4 Analytical Results of the Semiclassical Calculation

We consider the extremely strong coupling conditions $g \gg \kappa, \gamma/2$, as described in the last section. Under these conditions we may obtain the solution to Eq. (3.22) by solving the eigenvalue problem

$$M\vec{x}' = \lambda\vec{x}' \quad (3.38)$$

or

$$|M - \lambda I| = 0. \quad (3.39)$$

The strong coupling conditions allow us to calculate the eigenvalues of Eq. (3.39) with the following two steps. We first neglect the κ and γ terms (i.e. set $\kappa = \gamma = 0$) in M and calculate the eigenvalue $\bar{\lambda}$. We then include the κ and γ terms in M and calculate the correction λ' to the eigenvalue $\bar{\lambda}$. Thus, the eigenvalue λ in Eq. (3.38) may be written as

$$\lambda = \bar{\lambda} + \lambda', \quad (3.40)$$

where $\bar{\lambda}$ and λ' determine the location and linewidth of the peaks in the modulation spectrum, respectively.

Let us now calculate $\bar{\lambda}$. Setting $\kappa = \gamma = 0$ in M , we replace Eq. (3.39) by

$$|\bar{M} - \bar{\lambda}I| = 0, \quad (3.41)$$

where

$$\bar{M} = \begin{pmatrix} -ig & 0 & g & 0 & 0 \\ 0 & ig & 0 & g & 0 \\ g\langle\hat{\sigma}_z\rangle_{ss} & 0 & -ig & 0 & g\langle\hat{a}\rangle_{ss} \\ 0 & g\langle\hat{\sigma}_z\rangle_{ss} & 0 & ig & g\langle\hat{a}\rangle_{ss}^* \\ -2g\langle\hat{\sigma}_-\rangle_{ss}^* & -2g\langle\hat{\sigma}_-\rangle_{ss} & -2g\langle\hat{a}\rangle_{ss}^* & -2g\langle\hat{a}\rangle_{ss} & 0 \end{pmatrix}. \quad (3.42)$$

Here the steady state solutions $\langle\hat{a}\rangle_{ss}$, $\langle\hat{\sigma}_-\rangle_{ss}$ and $\langle\hat{\sigma}_z\rangle_{ss}$ to Eqs. (2.3) are

$$\langle\hat{a}\rangle_{ss} = -iq, \quad \langle\hat{\sigma}_-\rangle_{ss} = q/(1+2q^2), \quad \langle\hat{\sigma}_z\rangle_{ss} = -(1+2q^2)^{-1}, \quad (3.43)$$

with $q = |\langle\hat{a}\rangle_{ss}|$. Substituting Eqs. (3.42) and (3.43) into Eq. (3.41), we then solve Eq. (3.41) and have

$$\begin{aligned} \bar{\lambda}_1 &= 0, \\ \bar{\lambda}_{2,3} &= \mp i \left[1 + 2q^2 + 1/(1+2q^2) - 2\sqrt{1+q^4} \right]^{1/2} g, \\ \bar{\lambda}_{4,5} &= \mp i \left[1 + 2q^2 + 1/(1+2q^2) + 2\sqrt{1+q^4} \right]^{1/2} g. \end{aligned} \quad (3.44)$$

For weak excitation, Eqs. (3.44) read as

$$\bar{\lambda}_1 = 0, \quad \bar{\lambda}_{2,3} = \mp i\sqrt{3}q^2g, \quad \bar{\lambda}_{4,5} = \mp 2ig. \quad (3.45)$$

When $q \rightarrow 0$, $\bar{\lambda}_{1,2,3} = 0$ and $\bar{\lambda}_{4,5} = \mp 2ig$. These eigenvalues correspond to the familiar “vacuum” Rabi resonances. For strong excitation, Eqs. (3.44) read as

$$\bar{\lambda}_1 = 0, \quad \bar{\lambda}_{2,3} = \pm ig, \quad \bar{\lambda}_{4,5} = \mp 2iqg. \quad (3.46)$$

These eigenvalues describe the atomic inversion, single cavity mode and atomic polarization. The analytical calculation agrees with the exact calculation shown in Fig. 3.6(b) very well.

Let us now calculate the correction λ' to the eigenvalue λ . Note that when we calculate $\bar{\lambda}$ in the above, we set $\kappa = \gamma = 0$. Now we have to consider the contribution from the small non-zero κ and γ terms to calculate the correction λ' . Thus, Eqs. (3.43) are replaced by

$$\begin{aligned}\langle \hat{a} \rangle_{ss} &= \mathcal{E}(\gamma/2 + ig)(1 + 2q^2)/\bar{w}, & \langle \hat{\sigma}_- \rangle_{ss} &= -g\mathcal{E}/\bar{w}, \\ \langle \hat{\sigma}_z \rangle_{ss} &= -(g^2 + \gamma^2/4)/[g^2(1 + 2q^2) + \gamma^2/4],\end{aligned}\quad (3.47)$$

where

$$\bar{w} = g^2 + (\kappa + ig)(\gamma/2 + ig)(1 + 2q^2). \quad (3.48)$$

Substituting Eqs. (3.47), (3.48) and (3.23) into Eq. (3.39), and then neglecting the second and higher order terms in λ' , κ and γ , we find

$$\lambda'_i = A/B, \quad (3.49)$$

$$\begin{aligned}A &= -2\kappa \left[\bar{\lambda}_i^4 + \bar{\lambda}_i^2 g^2 (4q^2 + w_0) - \bar{\lambda}_i \gamma g^2 w_1 \right] \\ &\quad - \gamma \left[2\bar{\lambda}_i^4 + \bar{\lambda}_i^2 g^2 (2q^2 + 3w_0) - \bar{\lambda}_i \gamma g^2 w_1 + 8g^4 w_2 \right],\end{aligned}$$

$$B = 5\bar{\lambda}_i^4 + 6\bar{\lambda}_i^2 g^2 (2q^2 + w_0) - 4\bar{\lambda}_i \gamma g^2 w_1 + 12g^4 w_2.$$

Here w_0 , w_1 , and w_2 have been defined as

$$w_0 = 1 + (1 + 2q^2)^{-1}, \quad w_1 = q^2/(1 + 2q^2), \quad w_2 = q^4/(1 + 2q^2). \quad (3.50)$$

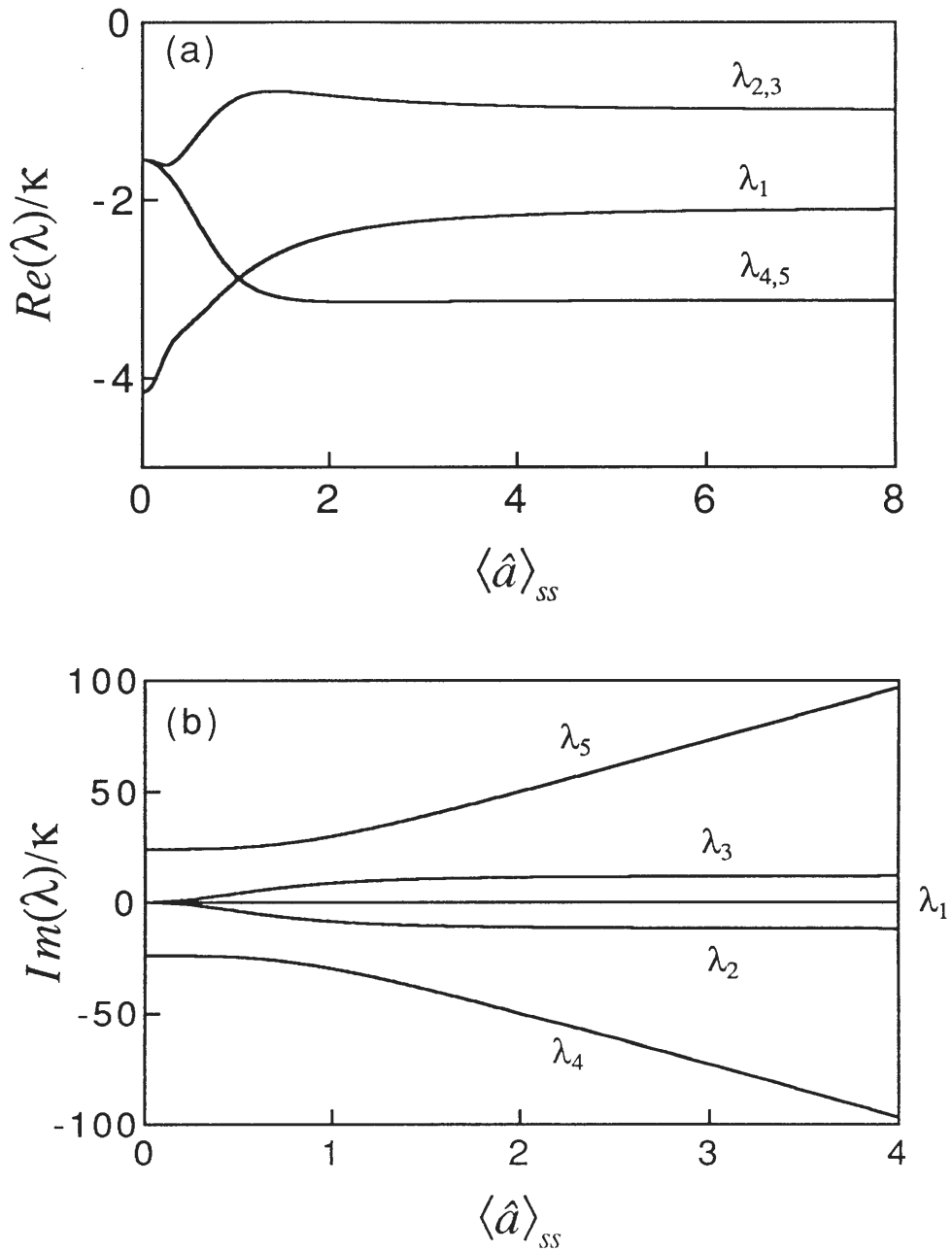


Figure 3.6. Eigenvalues of Eq. (3.22) plotted as a function of $\langle \hat{a} \rangle_{ss}$ for $g/\kappa = 12$, $2g/\gamma = 5.6$: (a) real part of the eigenvalues, (b) imaginary part of the eigenvalues.

Note that Eq. (3.49) is invalid in the limit of very weak excitation for $i = 1, 2, 3$ since in this limit $\bar{\lambda}_{2,3} \rightarrow \bar{\lambda}_1 = 0$ (see Fig. 3.6(b)).

In this case, we need to keep all of the lowest dominant terms in $\bar{\lambda}$, λ' , κ and γ in Eq. (3.39). We then find

$$\lambda'_1 = -\gamma, \quad \lambda'_2 = -\alpha, \quad \lambda'_3 = -\alpha. \quad (3.51)$$

According to Eqs. (3.49), λ'_4 and λ'_5 are obtained as

$$\lambda'_4 = -\alpha, \quad \lambda'_5 = -\alpha. \quad (3.52)$$

From Eqs. (3.45), (3.51) and (3.52), we have the eigenvalues in the limit of weak excitation,

$$\lambda_1 = \gamma, \quad \lambda_{2,3} = \mp i\sqrt{3}q^2g - \alpha, \quad \lambda_{4,5} = \mp 2ig - \alpha. \quad (3.53)$$

To make a comparison with the QED calculation, we will construct the modulation spectrum in the limit of weak excitation. Let us write \vec{x} in the form

$$\vec{x}' = \sum_{i=1}^5 \vec{y}_i \exp(\lambda_i t), \quad (3.54)$$

where λ_i is given in Eqs. (3.53), and \vec{y}_i is the coefficient vector. Substituting Eq. (3.54) into Eq. (3.22), we calculate \vec{y}_i . We are only interested in the amplitude of the transmitted cavity field

$$\langle \hat{a}'(t) \rangle = \sum_{i=1}^5 a_i \exp(\lambda_i t). \quad (3.55)$$

Here the expression of a_i is

$$a_2 = \frac{(1 + p_3/z^*)/p_1 + (1 + p_3/p_2)/z}{2[(1/p_1^2 - 1/p_2^2)/p_1 + (1 + p_1/p_2)(1/z^* + 1/z)]},$$

$$a_3 = [(1 + p_3/z^*)/2 - a_2(1 + p_1/z^*)]/(1 - p_2/z^*), \quad (3.56)$$

$$a_1 = -[p_3/2 + (a_3p_2 - a_2p_1)]/z^*,$$

$$a_4 = 1/2, \quad a_5 = 0,$$

where

$$\begin{aligned} z &= 2q^2 + i(\kappa - 3\gamma/2)/g, \quad p_1 = 2(\sqrt{3} - 1)q^2 - \bar{\beta}^2/g^2, \\ p_2 &= 2(\sqrt{3} + 1)q^2 + \bar{\beta}^2/g^2, \quad p_3 = 2q^2 + \bar{\beta}^2/g^2, \\ \bar{\beta} &= (\kappa - \gamma/2)/2, \end{aligned} \quad (3.57)$$

z^* is the conjugate of z .

The modulation spectrum may now be calculated by substituting Eq. (3.55) into Eq. (3.12). It takes the form

$$S(\nu) = \left| \frac{a_1}{i\nu - \gamma} + \frac{a_2}{i(\nu - \sqrt{3}q^2g) - \alpha} + \frac{a_3}{i(\nu + \sqrt{3}q^2g) - \alpha} + \frac{a_4}{i(\nu - 2g) - \alpha} \right|^2. \quad (3.58)$$

In the limit of weak excitation ($q \rightarrow 0$), Eq. (3.58) describes a two-peaked spectrum, with the left peak slightly shifted from the position of the lower “vacuum” Rabi resonance (the shift depends on q^2g) and the right peak located at the upper “vacuum” Rabi resonance $2g$. There is no evidence of the new peak in between the vacuum Rabi peaks. From Eq. (3.58) we calculate the ratio of the intensity of the left peak to that of the right peak as a function of q . We find the ratio is always larger than unity as q is increased which agrees with Fig. 3.5.

Before we close this section, we give the modulation spectrum in the limit of very

strong excitation. From Eqs. (3.49), we have

$$\lambda'_1 = -\gamma/2, \quad \lambda'_{2,3} = -\kappa, \quad \lambda'_{4,5} = -3\gamma/4. \quad (3.59)$$

Eqs. (3.51), (3.52) and (3.59) agree with the curves shown in Fig. 3.6(a) very well.

Combining Eqs. (3.59) and (3.46), we obtain

$$\lambda_1 = -\gamma/2, \quad \lambda_{2,3} = \mp ig - \kappa, \quad \lambda_{4,5} = \mp 2iqg - 3\gamma/4. \quad (3.60)$$

From these equations, the amplitude of the transmitted cavity field may be constructed as

$$\langle \hat{a}(t) \rangle = \exp[-(ig + \kappa)t]. \quad (3.61)$$

Thus, the corresponding modulation spectrum is given by

$$S(\nu) = [\kappa^2 + (\nu - g)^2]^{-1}. \quad (3.62)$$

Eq. (3.62) describes a one-peaked spectrum with the location at g and a linewidth of κ . The same result can be obtained from the QED theory.

CHAPTER IV

INCOHERENT EXCITATION: SPECTROSCOPY

In the previous two chapters we have studied the coherent excitation of an atom-cavity-mode system. This chapter concerns incoherent excitation of the system. We calculate scattered, transmitted and reflected spectra for this system driven by broad-band chaotic light. We begin with an analytical calculation in the secular approximation. This gives useful expressions for linewidths and transition amplitudes. But the secular approximation can be quite inaccurate for practical parameter values. We therefore also calculate the spectra numerically, without using the secular approximation. The results of the exact numerical calculations and the analytical calculations are compared. Prospects for experiments are discussed.

4.1 Matrix Element Equations in the Secular Approximation

We consider a coupled atom-cavity-mode system. The atom interacts with a field $\hat{\Gamma}_a(t)$ entering through the side of the cavity, and the cavity mode interacts with the fields $\hat{\Gamma}_i(t)$ and $\hat{\Gamma}_t(t)$ entering through two partially transmitting mirrors. We model the fields by quantized white noise; $\hat{\Gamma}_a(t)$ and $\hat{\Gamma}_i(t)$ have nonzero intensities that represent sources of broad-band chaotic light, and $\hat{\Gamma}_t(t)$ is a vacuum field. The system is depicted in Figure 4.1. The nonvanishing field correlation functions are

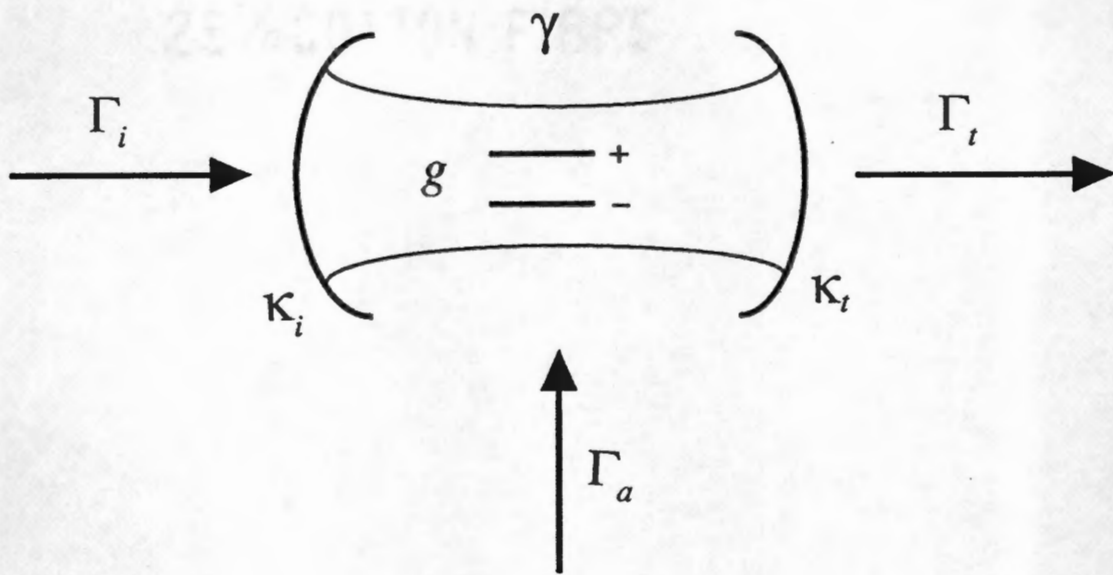


Figure 4.1. Schematic diagram of a single atom in a cavity driven by incoherent fields.

$$\begin{aligned}
\langle \hat{\Gamma}_a^\dagger(t) \hat{\Gamma}_a(t') \rangle &= \gamma M \delta(t - t'), \\
\langle \hat{\Gamma}_a(t) \hat{\Gamma}_a^\dagger(t') \rangle &= \gamma(M + 1) \delta(t - t'), \\
\langle \hat{\Gamma}_i^\dagger(t) \hat{\Gamma}_i(t') \rangle &= 2\kappa_i N \delta(t - t'), \\
\langle \hat{\Gamma}_i(t) \hat{\Gamma}_i^\dagger(t') \rangle &= 2\kappa_i(N + 1) \delta(t - t'), \\
\langle \hat{\Gamma}_t(t) \hat{\Gamma}_t^\dagger(t') \rangle &= 2\kappa_t \delta(t - t'),
\end{aligned} \tag{4.1}$$

where $\hat{\Gamma}_a(t)$, $\hat{\Gamma}_i(t)$, and $\hat{\Gamma}_t(t)$ have photon flux units, γ is the cavity-inhibited linewidth (full-width at half-maximum) of the atom, and $2(\kappa_i + \kappa_t)$ is the linewidth of the cavity mode. The intensities of the driving fields are determined by the parameters M and N ; γM is the photon flux per atomic absorption cross-section for the field $\hat{\Gamma}_a(t)$, and $2\kappa_i N$ is the photon flux coupled into the cavity mode from the field $\hat{\Gamma}_i(t)$. The white noise assumption is an approximation. In practice the spectra we calculate hold for driving-field bandwidths that are much greater than the widths of the computed spectra.

Our model system is described by the master equation

$$\begin{aligned}
\dot{\rho} &= (1/i\hbar) [\hat{H}_{JC}, \rho] + (\gamma/2)(M + 1)(2\hat{\sigma}_- \rho \hat{\sigma}_+ - \hat{\sigma}_+ \hat{\sigma}_- \rho - \rho \hat{\sigma}_+ \hat{\sigma}_-) \\
&\quad + (\gamma/2)M(2\hat{\sigma}_+ \rho \hat{\sigma}_- - \hat{\sigma}_- \hat{\sigma}_+ \rho - \rho \hat{\sigma}_- \hat{\sigma}_+) \\
&\quad + [\kappa_i(N + 1) + \kappa_t](2\hat{a} \rho \hat{a}^\dagger - \hat{a}^\dagger \hat{a} \rho - \rho \hat{a}^\dagger \hat{a}) \\
&\quad + \kappa_i N(2\hat{a}^\dagger \rho \hat{a} - \hat{a} \hat{a}^\dagger \rho - \rho \hat{a} \hat{a}^\dagger),
\end{aligned} \tag{4.2}$$

where \hat{H}_{JC} has been defined in Eq. (2.7). We consider extremely strong coupling

conditions and make the transformation

$$\bar{\rho} = \exp(i\hat{H}_{JC}t/\hbar)\rho\exp(-i\hat{H}_{JC}t/\hbar). \quad (4.3)$$

We then drop all oscillatory terms in the transformed master equation using the secular approximation [45]. Since we drop terms oscillating at frequencies $\pm 2(\sqrt{n+1} - \sqrt{n})g$, this may not be a good approximation, even at moderate excitation levels. Nevertheless, it is useful to begin by obtaining analytical results; we will assess the accuracy of the secular approximation later on. In the secular approximation the diagonal matrix elements of $\bar{\rho}$ satisfy the rate equations

$$\begin{aligned} \dot{\bar{\rho}}_g &= -2\gamma_{g,1}\bar{\rho}_g + 2\gamma_{1,g}\bar{\rho}_1, \\ \dot{\bar{\rho}}_1 &= -(\gamma_{1,g} + 2\gamma_{1,2})\bar{\rho}_1 + \gamma_{g,1}\bar{\rho}_g + 2\gamma_{2,1}\bar{\rho}_2, \\ \dot{\bar{\rho}}_n &= -2(\gamma_{n,n-1} + \gamma_{n,n+1})\bar{\rho}_n + 2\gamma_{n-1,n}\bar{\rho}_{n-1} + 2\gamma_{n+1,n}\bar{\rho}_{n+1}, \quad n = 2, 3, \dots, \end{aligned} \quad (4.4)$$

where $\bar{\rho}_g = \langle g|\bar{\rho}|g\rangle$ and $\bar{\rho}_n = \langle n, l|\bar{\rho}|n, l\rangle = \langle n, u|\bar{\rho}|n, u\rangle$; the transition rates are

$$\begin{aligned} \gamma_{g,1} &= (\gamma/2)M + \kappa_i N, \\ \gamma_{1,g} &= (\gamma/2)(M+1) + \kappa_i(N+1) + \kappa_t, \\ \gamma_{n,n+1} &= (\gamma/4)M + (\kappa_i/2)N(2n+1), \quad n = 1, 2, \dots, \\ \gamma_{n,n-1} &= (\gamma/4)(M+1) + [(\kappa_i/2)(N+1) + (\kappa_t/2)](2n-1), \quad n = 2, 3, \dots \end{aligned} \quad (4.5)$$

Note the symmetry between states labelled by u and by l which leads us to omit these labels on the diagonal matrix elements and transition rates. We will retain the u, l labels on the off-diagonal matrix elements, however, since the off-diagonal

matrix elements of $\bar{\rho}$ are replaced by matrix elements of correlation functions when we calculate spectra, and it is helpful if the correlation functions with different u, l -labels are distinguished. Thus, we write the equations of motion for off-diagonal matrix elements as

$$\begin{aligned}\dot{\bar{\rho}}_{1,\eta;g} &= -(\gamma_{1,g}/2 + \gamma_{1,2} + \gamma_{g,1})\bar{\rho}_{1,\eta;g}, \\ \dot{\bar{\rho}}_{2,\eta;1,\xi} &= -(\gamma_{2,1} + \gamma_{2,3} + \gamma_{1,2} + \gamma_{1,g}/2)\bar{\rho}_{2,\eta;1,\xi}, \\ \dot{\bar{\rho}}_{n+1,\eta;n,\xi} &= -(\gamma_{n+1,n} + \gamma_{n+1,n+2} + \gamma_{n,n+1} + \gamma_{n,n-1})\bar{\rho}_{n+1,\eta;n,\xi}, \quad n = 2, 3, \dots\end{aligned}\tag{4.6}$$

Here $\bar{\rho}_{1,\eta;g} = \langle 1, \eta | \bar{\rho} | g \rangle$, $\bar{\rho}_{n+1,\eta;n,\xi} = \langle n+1, \eta | \bar{\rho} | n, \xi \rangle$, and η and ξ are either u or l .

Under the transformation (4.3) the matrix elements of ρ are given by

$$\rho_g = \bar{\rho}_g, \quad \rho_n = \bar{\rho}_n,\tag{4.7}$$

and

$$\begin{aligned}\rho_{1,\eta;g} &= \exp[-i(\omega_0 + \epsilon_\eta g)t]\bar{\rho}_{1,\eta;g}, \\ \rho_{n+1,\eta;n,\xi} &= \exp(-i\omega_0 + \epsilon_\eta \sqrt{n+1}g - \epsilon_\xi \sqrt{n}gt)\bar{\rho}_{n+1,\eta;n,\xi},\end{aligned}\tag{4.8}$$

where $\epsilon_\eta (\epsilon_\xi) = +1, -1$ for $\eta (\xi) = u, l$.

4.2 Steady-State Solutions

Because of the symmetry between states carrying the labels u and l we can add the populations $\langle n, u | \bar{\rho} | n, u \rangle = \bar{\rho}_n$ and $\langle n, l | \bar{\rho} | n, l \rangle = \bar{\rho}_n$ for $n = 1, 2, \dots$, so that Eqs. (4.4) describe a one-dimensional array of states with transitions between neighboring

states. Such a configuration comes to a steady state in detailed balance [50]. We have

$$\begin{aligned} 2(\bar{\rho}_1)_{ss} &= (2\gamma_{g,1}/\gamma_{1,g})(\bar{\rho}_g)_{ss}, \\ 2(\bar{\rho}_{n+1})_{ss} &= (\gamma_{n,n+1}/\gamma_{n+1,n})2(\bar{\rho}_n)_{ss}, \quad n = 1, 2, \dots \end{aligned} \quad (4.9)$$

which gives the steady-state populations

$$(\rho_n)_{ss} = (\bar{\rho}_n)_{ss} = \prod_{m=1}^n \left(\frac{(\gamma/2)M + (2m-1)\kappa_i N}{(\gamma/2)(M+1) + (2m-1)[\kappa_i(N+1) + \kappa_t]} \right) (\rho_g)_{ss}, \quad (4.10)$$

with

$$2 \sum_{n=1}^{\infty} (\bar{\rho}_n)_{ss} + (\bar{\rho}_g)_{ss} = 1. \quad (4.11)$$

When $\kappa_t = 0$ and $M = N$ (all reservoirs at the same temperature) we obtain the expected thermal equilibrium distribution:

$$(\rho_g)_{ss} = \frac{1}{1+2N}, \quad (\rho_n)_{ss} = \frac{1}{1+2N} \left(\frac{N}{1+N} \right)^n, \quad n = 1, 2, \dots \quad (4.12)$$

Note that if N is the mean thermal photon number at frequency ω_0 and temperature T , then $N/(1+N) = \exp[-\hbar\omega_0/k_B T]$; also, the normalization obtained from Eq. (4.11) accounts for the fact that there are *two* states ($|n, u\rangle$ and $|n, l\rangle$) with energy $E_n - E_g \approx n\hbar\omega_0$, $n = 1, 2, \dots$ (The master equation (4.2) does not include the corrections needed to reach the exact thermal equilibrium, with the dipole interaction energy included — $E_n - E_g = n\hbar\omega_0 \pm \sqrt{n}\hbar g$ [51].)

We will be interested primarily in conditions with either M or N set to zero. Then the connection with thermal equilibrium holds in the following limiting cases: When $M = 0$ only the cavity is illuminated. Then, if $\kappa_i(N+1) + \kappa_t \gg \gamma/2$ we have

$$(\rho_g)_{ss} = \frac{1 + \kappa_t/\kappa_i}{1 + \kappa_t/\kappa_i + 2N},$$

$$(\rho_n)_{ss} = \frac{1 + \kappa_t/\kappa_i}{1 + \kappa_t/\kappa_i + 2N} \left(\frac{N}{1 + \kappa_t/\kappa_i + N} \right)^n, \quad n = 1, 2, \dots \quad (4.13)$$

This is the thermal equilibrium distribution (4.12) with N replaced by $N/(1 + \kappa_i/\kappa_t)$.

When $N = 0$ only the atom is illuminated. Then, if $(\gamma/2)(M + 1) \gg \kappa_i + \kappa_t$ we recover the distribution (4.12) with N replaced by M .

For general parameter values the distribution (4.10) is not exactly a thermal equilibrium distribution. It is similar, however; $(\rho_g)_{ss}$ is always the largest probability, with $(\rho_n)_{ss}$ falling off monotonically with increasing n . Of course, in the secular approximation the off-diagonal matrix elements of ρ are all zero in steady state. Without the secular approximation they are not; we will see the consequences of this fact later on.

4.3 Spectra

In this section we calculate three spectra in the secular approximation: the spectrum of dipole scattering from the atom, the spectrum of the light transmitted by the cavity, and for the case where the cavity mode is driven, the spectrum of the light reflected by the cavity.

4.3.1 Spectrum of Atomic Dipole Scattering

The spectrum of dipole scattering from the atom is given by the Fourier transform of the autocorrelation function of the atomic dipole operator [52]:

$$P_a(\omega) = (1/\pi) \text{Re} \int_0^\infty \langle \hat{\sigma}_+(0) \hat{\sigma}_-(\tau) \rangle_{ss} \exp(i\omega\tau) d\tau, \quad (4.14)$$

where the normalization is such that the integral of $P_a(\omega)$ over all frequencies gives the probability for the atom to be in its excited state. In the secular approximation the dipole correlation function may be expanded in the dressed-state basis as

$$\langle \hat{\sigma}_+(0)\hat{\sigma}_-(\tau) \rangle_{ss} = \frac{1}{2} \sum_{\eta} \langle \hat{S}_{g\eta}^\dagger(0)\hat{S}_{g\eta}(\tau) \rangle_{ss} + \frac{1}{4} \sum_{n=1}^{\infty} \sum_{\eta,\xi} \langle \hat{S}_{\xi\eta}^{n\dagger}(0)\hat{S}_{\xi\eta}^n(\tau) \rangle_{ss}. \quad (4.15)$$

Here η and ξ are either u or l , and $\hat{S}_{g\eta} \equiv |g\rangle\langle 1, \eta|$, $\hat{S}_{\xi\eta}^n \equiv |n, \xi\rangle\langle n+1, \eta|$, $n = 1, 2, \dots$. In general, nondiagonal terms $\langle \hat{S}_{g\eta}^\dagger(0)\hat{S}_{g\eta'}(\tau) \rangle_{ss}$ and $\langle \hat{S}_{\xi\eta}^{n\dagger}(0)\hat{S}_{\xi'\eta'}^n(\tau) \rangle_{ss}$ also appear in the expansion, but in the secular approximation these are all zero.

Now according to the quantum regression theorem [53], the correlation functions on the right-hand side of Eq. (4.15) satisfy the same equations of motion as the off-diagonal matrix elements of ρ , with the initial conditions $\langle \hat{S}_{g\eta}^\dagger(0)\hat{S}_{g\eta}(0) \rangle_{ss} = (\rho_1)_{ss}$, $\langle \hat{S}_{\xi\eta}^{n\dagger}(0)\hat{S}_{\xi\eta}^n(0) \rangle_{ss} = (\rho_{n+1})_{ss}$, $n = 1, 2, \dots$. Thus, from Eqs. (4.6), (4.7) and (4.8), we have

$$\begin{aligned} \langle \hat{S}_{g\eta}^\dagger(0)\hat{S}_{g\eta}(\tau) \rangle_{ss} &= (\rho_1)_{ss} e^{-\beta|\tau|} \exp[-i(\omega_0 + \epsilon_\eta g)\tau], \\ \langle \hat{S}_{\xi\eta}^{n\dagger}(0)\hat{S}_{\xi\eta}^n(\tau) \rangle_{ss} &= (\rho_{n+1})_{ss} e^{-\alpha_n|\tau|} \exp(-i\omega_0 + \epsilon_\eta \sqrt{n+1}g - \epsilon_\xi \sqrt{n}g)\tau, \end{aligned} \quad n = 1, 2, \dots, (4.16)$$

where

$$\begin{aligned} \beta &= \gamma_{1,g}/2 + \gamma_{1,2} + \gamma_{g,1}, \\ \alpha_1 &= \gamma_{2,1} + \gamma_{2,3} + \gamma_{1,2} + \gamma_{1,g}/2, \\ \alpha_n &= \gamma_{n+1,n} + \gamma_{n+1,n+2} + \gamma_{n,n+1} + \gamma_{n,n-1}, \quad n = 2, 3, \dots \end{aligned} \quad (4.17)$$

The spectrum is then given by a sum of Lorentzians:

$$P_a(\omega) = (\rho_1)_{ss}(1/2)[L_{gu}(\omega) + L_{gl}(\omega)] \\ + \sum_{n=1}^{\infty} (\rho_{n+1})_{ss}(1/4)[L_{uu}^n(\omega) + L_{ll}^n(\omega) + L_{lu}^n(\omega) + L_{ul}^n(\omega)], \quad (4.18)$$

with

$$L_{gu}(\omega) = \frac{\beta/\pi}{\beta^2 + (\omega - \omega_0 - g)^2}, \quad L_{gl}(\omega) = \frac{\beta/\pi}{\beta^2 + (\omega - \omega_0 + g)^2}, \quad (4.19)$$

and

$$L_{uu}^n(\omega) = \frac{\alpha_n/\pi}{\alpha_n^2 + (\omega - \omega_0 - \delta_n^- g)^2}, \quad L_{ll}^n(\omega) = \frac{\alpha_n/\pi}{\alpha_n^2 + (\omega - \omega_0 + \delta_n^- g)^2}, \\ L_{lu}^n(\omega) = \frac{\alpha_n/\pi}{\alpha_n^2 + (\omega - \omega_0 - \delta_n^+ g)^2}, \quad L_{ul}^n(\omega) = \frac{\alpha_n/\pi}{\alpha_n^2 + (\omega - \omega_0 + \delta_n^+ g)^2}, \\ n = 1, 2, \dots, \quad (4.20)$$

where we have defined

$$\delta_n^\pm = \sqrt{n+1} \pm \sqrt{n}. \quad (4.21)$$

The first two Lorentzians in Eq. (4.18) give the “vacuum” Rabi peaks. They are produced by transitions to the ground state from the first excited states. In addition, for each of the higher excited states there are four Lorentzians produced by transitions between excited states — $\{|n+1, u\rangle \text{ or } |n+1, l\rangle\} \rightarrow \{|n, u\rangle \text{ or } |n, l\rangle$, for $n = 1, 2, \dots$

4.3.2 Spectrum of Light Transmitted by the Cavity

The light transmitted by the cavity mirrors is described by the quantized fields

$$\hat{\mathcal{E}}_r(t) = \hat{\Gamma}_i(t_R) + \sqrt{2\kappa_i} \hat{a}(t_R), \\ \hat{\mathcal{E}}_t(t) = \hat{\Gamma}_t(t_R) + \sqrt{2\kappa_t} \hat{a}(t_R), \quad (4.22)$$

where $\hat{\mathcal{E}}_r(t)$ and $\hat{\mathcal{E}}_t(t)$ have photon flux units, and t_R denotes the retarded time. If the intensity of the light driving the cavity is zero ($N = 0$) these fields have the same spectrum. If it is not, the spectra are different; then we refer to $\hat{\mathcal{E}}_t(t)$ and $\hat{\mathcal{E}}_r(t)$ as the transmitted and reflected fields, respectively.

The spectrum of the transmitted field is given by the Fourier transform of the autocorrelation function for the field amplitude:

$$\begin{aligned} P_t(\omega) &= (2\kappa_t)^{-1}(1/\pi)\text{Re} \int_0^\infty \langle \hat{\mathcal{E}}_t^\dagger(0)\hat{\mathcal{E}}_t(\tau) \rangle_{ss} \exp(i\omega\tau) d\tau \\ &= (1/\pi)\text{Re} \int_0^\infty \langle \hat{a}^\dagger(0)\hat{a}(\tau) \rangle_{ss} \exp(i\omega\tau) d\tau, \end{aligned} \quad (4.23)$$

where the integral of $P_t(\omega)$ over all frequencies gives the mean number of photons in the cavity. The vacuum field $\hat{\Gamma}_t(t_R)$ does not contribute because the operators in Eq. (4.23) appear in normal order. We follow the calculational procedure that gave the spectrum of dipole scattering and, in the secular approximation, expand the field correlation function as

$$\langle \hat{a}^\dagger(0)\hat{a}(\tau) \rangle_{ss} = \frac{1}{2} \sum_\eta \langle \hat{S}_{g\eta}^\dagger(0)\hat{S}_{g\eta}(\tau) \rangle_{ss} + \frac{1}{4} \sum_{n=1}^\infty \sum_{\eta,\xi} C_{\eta,\xi}^n \langle \hat{S}_{\xi\eta}^{n\dagger}(0)\hat{S}_{\xi\eta}^n(\tau) \rangle_{ss}, \quad (4.24)$$

where

$$C_{\eta,\xi}^n = \sqrt{n+1} + \epsilon_\eta \epsilon_\xi \sqrt{n}, \quad n = 1, 2, \dots, \quad (4.25)$$

with $\epsilon_\eta (\epsilon_\xi) = +1, -1$ for $\eta (\xi) = u, l$. Then, using Eqs. (4.16) we obtain a spectrum similar to Eq. (4.18):

$$\begin{aligned} P_t(\omega) &= (\rho_1)_{ss}(1/2) [L_{gu}(\omega) + L_{gl}(\omega)] + \sum_{n=1}^\infty (\rho_{n+1})_{ss}(1/4) \\ &\quad \left[C_{u,u}^n L_{uu}^n(\omega) + C_{l,l}^n L_{ll}^n(\omega) + C_{l,u}^n L_{lu}^n(\omega) + C_{u,l}^n L_{ul}^n(\omega) \right]. \end{aligned} \quad (4.26)$$

The only difference is the appearance of the constants $C_{\eta,\xi}^n$, which changes the relative heights of the spectral peaks.

4.3.3 Spectrum of Light Reflected by the Cavity

The spectrum of the reflected field is given by

$$P_r(\omega) = (2\kappa_i)^{-1}(1/\pi)Re \int_0^\infty \langle \hat{\mathcal{E}}_r(0)^\dagger \hat{\mathcal{E}}_r(\tau) \rangle_{ss} \exp(i\omega\tau) d\tau, \quad (4.27)$$

where $\hat{\mathcal{E}}_r(t) = \hat{\Gamma}_i(t_R) + \sqrt{2\kappa_i} \hat{a}(t_R)$ [the first of Eqs. (4.22)]. Since $\hat{\Gamma}_i(t)$ is not a vacuum field this spectrum is given by the sum four terms: The driving field $\hat{\Gamma}_i(t)$ contributes the broad-band (white) background

$$(2\kappa_i)^{-1}(1/\pi)Re \int_0^\infty \langle \hat{\Gamma}_i^\dagger(0) \hat{\Gamma}_i(\tau) \rangle_{ss} \exp(i\omega\tau) d\tau = N, \quad (4.28)$$

the normalization gives units of photon number per unit bandwidth. To this background is added the transmitted spectrum $P_t(\omega)$ and two interference terms given by Fourier transforms of the correlation functions [54]

$$(\sqrt{2\kappa_i})^{-1} \langle \hat{a}^\dagger(0) \hat{\Gamma}_i(\tau) \rangle_{ss} = \begin{cases} N \langle [\hat{a}^\dagger(0), \hat{a}(\tau)] \rangle_{ss} & \tau < 0 \\ (1/2)N \langle [\hat{a}^\dagger(0), \hat{a}(\tau)] \rangle_{ss} & \tau = 0 \\ 0 & \tau > 0 \end{cases} \quad (4.29)$$

and

$$(\sqrt{2\kappa_i})^{-1} \langle \hat{\Gamma}_i^\dagger(0) \hat{a}(\tau) \rangle_{ss} = \begin{cases} 0 & \tau < 0 \\ (1/2)N \langle [\hat{a}^\dagger(0), \hat{a}(\tau)] \rangle_{ss} & \tau = 0 \\ N \langle [\hat{a}^\dagger(0), \hat{a}(\tau)] \rangle & \tau > 0. \end{cases} \quad (4.30)$$

One part of the commutator on the right-hand side of Eqs. (4.29) and (4.30) contributes $NP_t(\omega)$ — thus, altogether, we add $(N + 1)P_t(\omega)$ to the background spectrum (4.28). The other piece of the commutator involves

$$\langle \hat{a}(\tau)\hat{a}^\dagger(0) \rangle_{ss} = \frac{1}{2} \sum_{\eta} \langle \hat{S}_{g\eta}(\tau)\hat{S}_{g\eta}^\dagger(0) \rangle_{ss} + \frac{1}{4} \sum_{n=1}^{\infty} \sum_{\eta,\xi} C_{\eta,\xi}^n \langle \hat{S}_{\xi\eta}^n(\tau)\hat{S}_{\xi\eta}^{n\dagger}(0) \rangle_{ss}, \quad (4.31)$$

which we have expanded, once again, in the secular approximation. Using the quantum regression theorem, $\langle \hat{S}_{g\eta}(\tau)\hat{S}_{g\eta}^\dagger(0) \rangle_{ss}$ and $\langle \hat{S}_{\xi\eta}^n(\tau)\hat{S}_{\xi\eta}^{n\dagger}(0) \rangle_{ss}$ are given by Eqs. (4.16), with $(\rho_1)_{ss}$ and $(\rho_{n+1})_{ss}$ replaced by $(\rho_g)_{ss}$ and $(\rho_n)_{ss}$, respectively. Then, putting the four terms together, the spectrum of the reflected light is given by

$$P_r(\omega) = N + R_1(1/2) [L_{gu}(\omega) + L_{gl}(\omega)] + \sum_{n=1}^{\infty} R_{n+1}(1/4) [C_{u,u}^n L_{uu}^n(\omega) + C_{l,l}^n L_{ll}^n(\omega) + C_{l,u}^n L_{lu}^n(\omega) + C_{u,l}^n L_{ul}^n(\omega)]. \quad (4.32)$$

where

$$\begin{aligned} R_1 &= (N + 1)(\rho_1)_{ss} - (\rho_g)_{ss}, \\ R_n &= (N + 1)(\rho_n)_{ss} - N(\rho_{n-1})_{ss}, \quad n = 2, 3, \dots \end{aligned} \quad (4.33)$$

Note that Eq. (4.32) reduces to Eq. (4.26) when $N = 0$.

4.4 Discussion

Examples of the spectra given by Eqs. (4.18), (4.26), and (4.32) are plotted as the dashed curves in Figs. 4.2 and 4.3. In Fig. 4.2 we plot spectra for the driven cavity, with $M = 0$ and $N = 5$; in Fig. 4.3 we plot spectra for the driven atom,

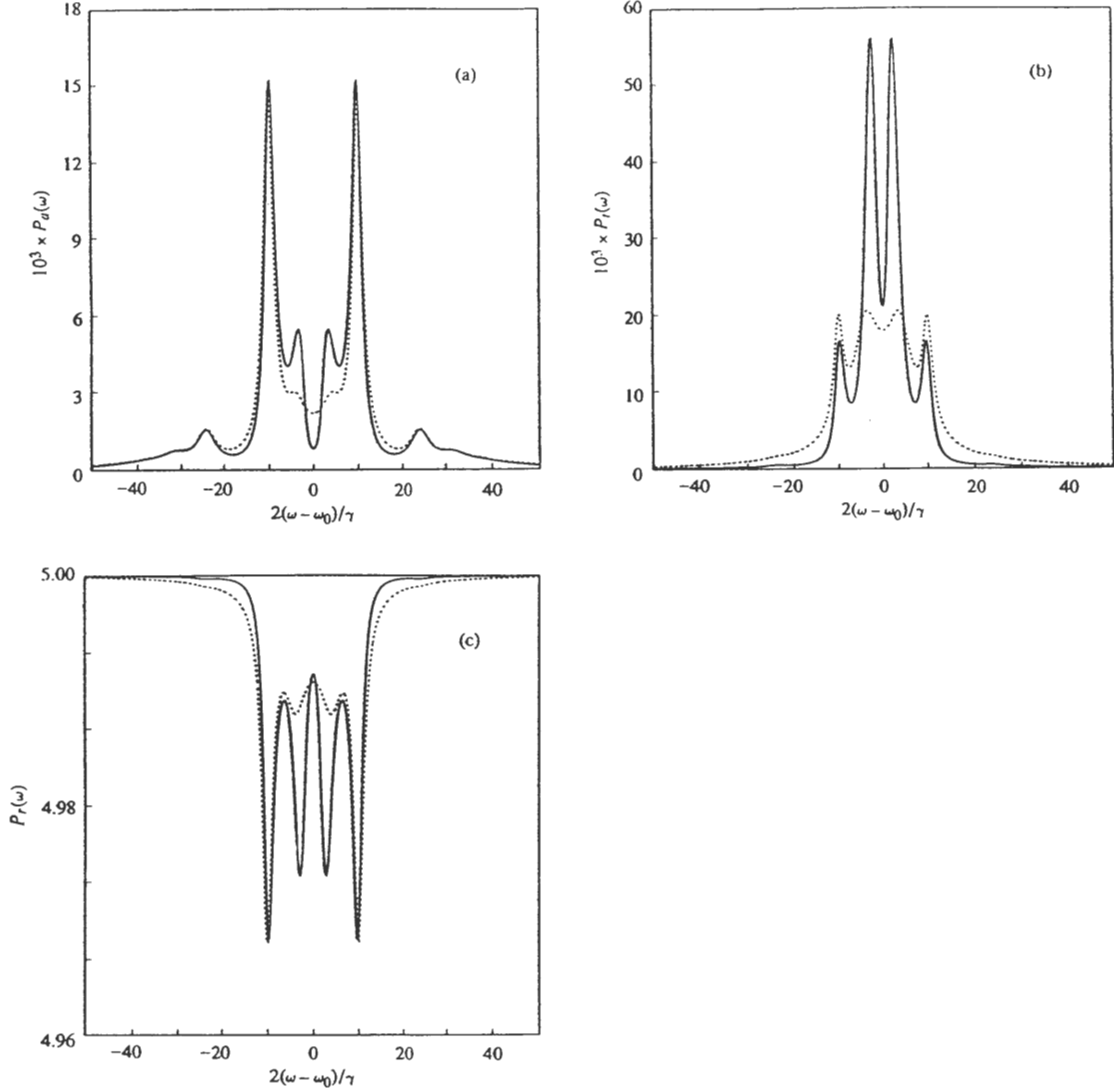


Figure 4.2. Spectra for driving field intensities $N = 5$ and $M = 0$, and $2g/\gamma = 10$, $2\kappa/\gamma = 0.1$: (a) The spectrum of atomic dipole scattering, (b) the spectrum of the light transmitted by the cavity, and (c) the spectrum of the light reflected by the cavity. The dashed curves are plotted from Eqs. (4.18), (4.26), and (4.32) which were derived using the secular approximation; the solid curves were calculated numerically without the use of the secular approximation.

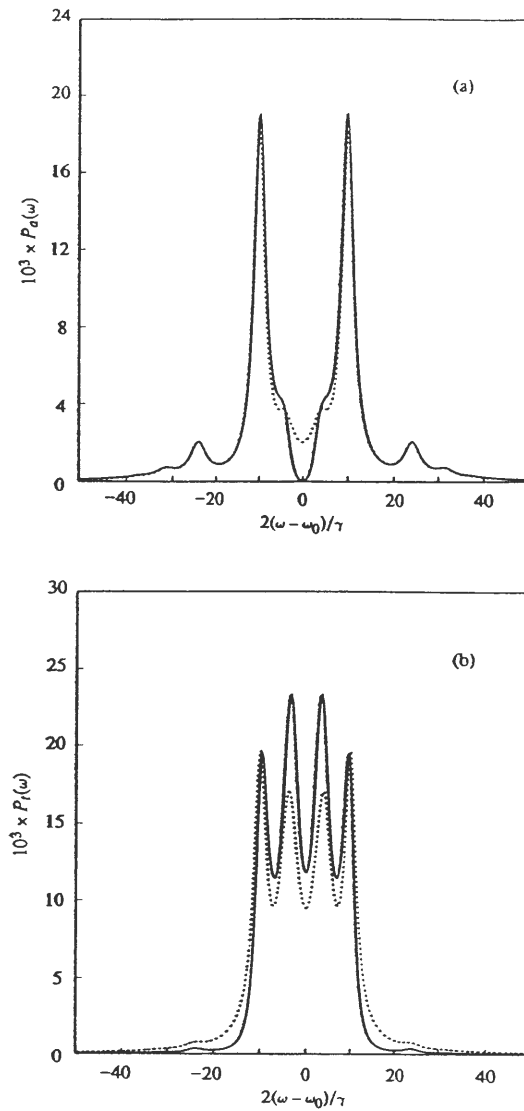


Figure 4.3. Spectra for driving field intensities $N = 0$ and $M = 0.5$, and $2g/\gamma = 10$, $2\kappa/\gamma = 0.1$: (a) The spectrum of atomic dipole scattering, and (b) the spectrum of the light transmitted by the cavity. The dashed curves are plotted from Eqs. (4.18), (4.26), and (4.32) which were derived using the secular approximation; the solid curves were calculated numerically without the use of the secular approximation.

with $N = 0$ and $M = 0.5$. The ratio of the atomic and cavity linewidths is 10 : 1, and we have chosen intensities ($N = 5$ and $M = 0.5$) in the same ratio so that the steady-state populations (4.10) are similar for the driven cavity and the driven atom.

All of the dashed curves in Figs. 4.2 and 4.3 show evidence of the excited state Jaynes-Cummings resonances. In addition to the prominent “vacuum” Rabi peaks at $\omega - \omega_0 = \pm g$, there are peaks at $\omega - \omega_0 = \pm(\sqrt{2}+1)g$ and $\omega - \omega_0 = \pm(\sqrt{2}-1)g$ caused by transitions between the first and second excited states of the Jaynes-Cummings Hamiltonian. There are two important points about linewidths and transition amplitudes that affect these spectra. First, for intensities $N > 1$ and $M > 1$, the widths α_n calculated from Eqs. (4.17) and (4.5) are significantly larger than the radiative widths of the atom and the cavity mode. The larger widths require a larger value of g to resolve the structure in the spectra. Thus, the observation of Jaynes-Cummings resonances using excitation by incoherent light becomes more and more impractical as the intensity of the light is raised in order to reach higher and higher excited states. Since the width contributed to the excited states by the cavity mode also increases in proportion to the principle quantum number n , the cavity width is more damaging in this respect than the atomic width. It is for this reason that we have chosen a cavity width ten times smaller than the atomic width for the plots in Figs. 4.2 and 4.3. The second observation concerns the comparison between the transition amplitudes associated with emission from the atom — the scattered spectrum, and from the cavity

— the transmitted spectrum. These are

$$\begin{aligned}\langle n, \xi | \hat{\sigma}_- | n+1, \eta \rangle &= -(1/2)(i\epsilon_\xi), \\ \langle n, \xi | \hat{a} | n+1, \eta \rangle &= (1/2)(\sqrt{n} + \epsilon_\xi \epsilon_\eta \sqrt{n+1}).\end{aligned}\tag{4.34}$$

The squares of these amplitudes, multiplied by the steady-state population $(\rho_{n+1})_{ss}$, determine the coefficients of the Lorentzians in the spectra (4.18) and (4.26). We see that for the atomic dipole scattering the strength of the $|n+1, u\rangle \rightarrow |n, u\rangle$ and $|n+1, l\rangle \rightarrow |n, l\rangle$ transitions is the same as the strength of the $|n+1, u\rangle \rightarrow |n, l\rangle$ and $|n+1, l\rangle \rightarrow |n, u\rangle$ transitions. But for the light transmitted by the cavity, the $|n+1, u\rangle \rightarrow |n, u\rangle$ and $|n+1, l\rangle \rightarrow |n, l\rangle$ transitions are stronger ($\epsilon_\xi \epsilon_\eta = +1$) than the $|n+1, u\rangle \rightarrow |n, l\rangle$ and $|n+1, l\rangle \rightarrow |n, u\rangle$ transitions ($\epsilon_\xi \epsilon_\eta = -1$). This is reflected in the comparison between Figs. 4.2(a) and 4.3(a) (atomic dipole scattering) and Figs. 4.2(b) and 4.3(b) (light transmitted by the cavity); in Figs. 4.2(b) and 4.3(b) the peaks that appear in between the “vacuum” Rabi peaks are stronger than those that appear outside the “vacuum” Rabi peaks, while in Figs. 4.2(a) and 4.3(a) they are not. Adding to this the fact that the amplitudes $\langle n, l | \hat{a} | n+1, l \rangle$ and $\langle n, u | \hat{a} | n+1, u \rangle$ are larger than the amplitudes $\langle n, l | \hat{\sigma}_- | n+1, l \rangle$ and $\langle n, u | \hat{\sigma}_- | n+1, u \rangle$, we would predict that the most prominent new peaks would be seen between the “vacuum” Rabi peaks, at frequencies $\omega - \omega_0 = \pm(\sqrt{2} - 1)g$, in the spectrum of the light transmitted by the cavity. This is what we find in Figs. 4.2 and 4.3.

For the parameters used in Figs. 4.2 and 4.3 the spectral peaks caused by transitions from the second excited state to the first appear at $2(\omega - \omega_0)/\gamma = \pm(\sqrt{2} -$

1)($2g/\gamma$) = ± 4.14 and $2(\omega - \omega_0)/\gamma = \pm(\sqrt{2} + 1)(2g/\gamma) = \pm 24.14$. The “vacuum” Rabi peaks appear at $2(\omega - \omega_0)/\gamma = \pm(2g/\gamma) = \pm 10.00$. Our use of the secular approximation assumes that all peaks are well separated compared to their widths. To check the validity of this approximation we can calculate the peak widths from Eqs. (4.17) and (4.5). The half-width of the “vacuum” Rabi peaks is given by

$$\beta = (\gamma/4)(4M + 1) + (\kappa_i/2)(6N + 1) + \kappa_t/2, \quad (4.35)$$

from which we obtain $2\beta/\gamma = 1.55$ for Fig. 4.2 and $2\beta/\gamma = 1.30$ for Fig. 4.3. The half-width α_1 for transitions from the second excited state to the first is given by

$$\alpha_1 = \gamma(M + 1/2) + 2\kappa_i(3N + 1) + 2\kappa_t, \quad (4.36)$$

from which we obtain $2\alpha_1/\gamma = 2.2$ and $2\alpha_1/\gamma = 2.7$ for Figs. 4.2 and 4.3, respectively. From these numbers, and from the figures themselves, it appears that the “vacuum” Rabi peaks and the two peaks falling between them are probably not sufficiently separated to justify the use of the secular approximation. For the smaller unresolved peaks caused by higher excited state transitions the situation is even worse; these transitions produce peaks that are both closer together and have larger widths. We have therefore also calculated the spectra numerically without making the secular approximation. These results are plotted as solid lines in Figs. 4.2 and 4.3. The differences between the solid and dashed lines are large near the center of the spectrum where the peaks are closest together and we would expect the secular approximation to be worst. It is good, however, to see that the additional resonances become more

prominent, not less, when the secular approximation is removed. The spectra of the light transmitted by the cavity [Figs. 4.2(b) and 4.3(b)] show substantial peaks in between the “vacuum” Rabi peaks, and corresponding absorption dips are present in the reflected spectrum [Fig. 4.3(c)].

To check that, for large enough g , the spectra obtained with the secular approximation approach those obtained without this approximation, we plot both for $2g/\gamma = 300$ in Fig. 4.4. On the whole the agreement is very good; although, near the center of the spectrum discernible differences still remain. This is because incoherent excitation produces a steady-state population distribution with a very long tail (almost thermal). Many excited state transitions contribute to the spectrum, and the transmitted spectrum, in particular, is affected by strong $|n + 1, u\rangle \rightarrow |n, u\rangle$ and $|n + 1, l\rangle \rightarrow |n, l\rangle$ transitions, which become broader and broader as the level of excitation increases. For these high level transitions the secular approximation is not very good, even for the large value of g used in Fig. 4.4.

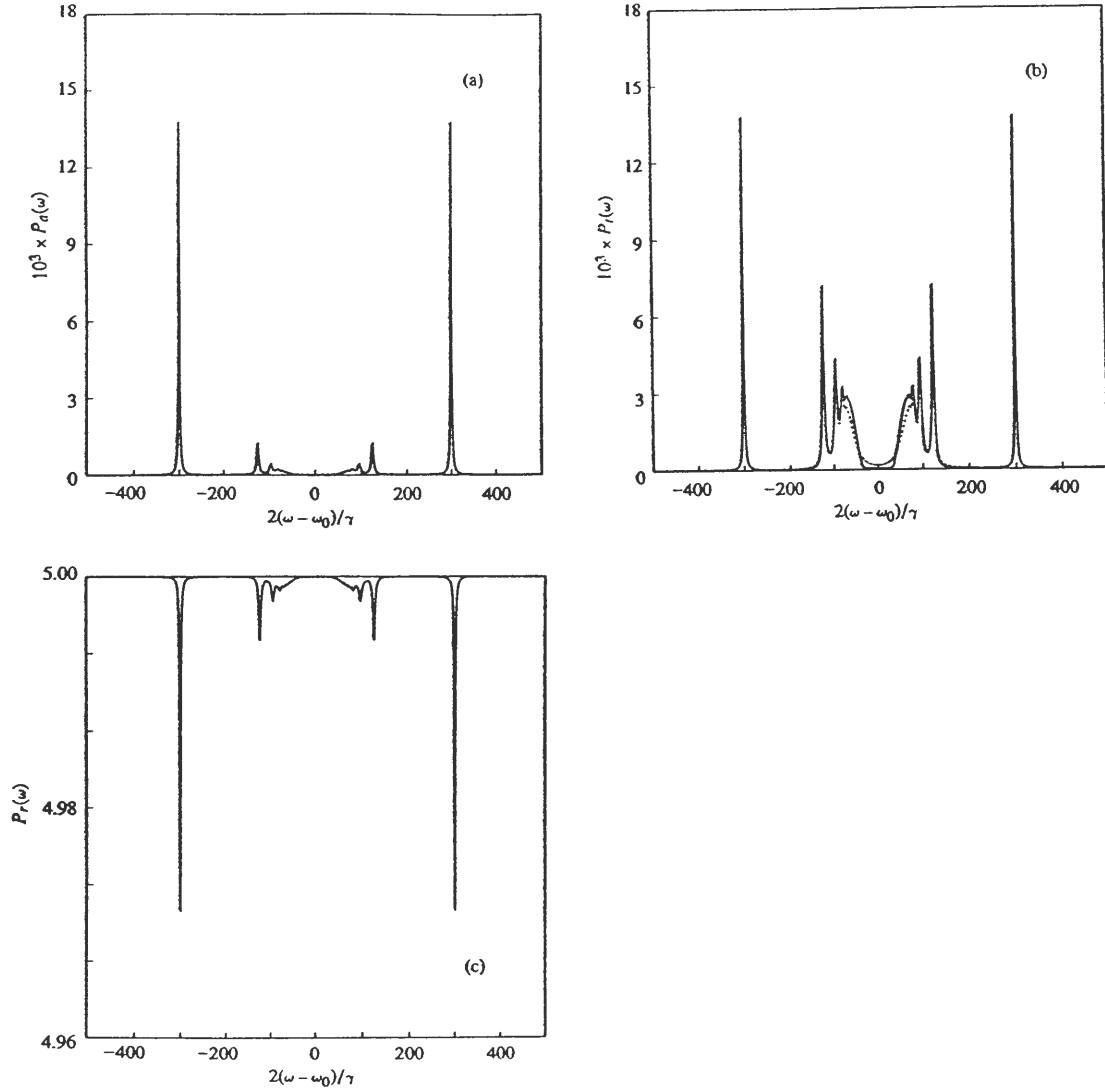


Figure 4.4. Spectra for driving field intensities $N = 5$ and $M = 0$, and $2g/\gamma = 300$, $2\kappa/\gamma = 0.1$: (a) The spectrum of atomic dipole scattering, (b) the spectrum of the light transmitted by the cavity, and (c) the spectrum of the light reflected by the cavity. The dashed curves are plotted from Eqs. (4.18), (4.26), and (4.32) which were derived using the secular approximation; the solid curves were calculated numerically without the use of the secular approximation.

CHAPTER V

QUANTUM TRAJECTORY THEORY

In the previous three chapters we have used the master equation approach to describe the dynamic evolution of a quantum mechanical source system. The next three chapters are going to deal with another approach, the quantum trajectory approach, which was developed very recently [22, 23, 24]. This new approach provides a new way of analyzing and thinking about the master equations that describe a photoemissive source. By considering an analogy with classical statistical physics one can understand the role of the new approach. In classical statistical physics, there are two approaches taken to describe the evolution of a system. The first uses a probability distribution and a Fokker-Planck equation which generates the evolution in time. The second uses an ensemble of noisy trajectories which is generated by a set of stochastic differential equations. In quantum physics, the corresponding two approaches are the master equation approach and the quantum trajectory approach. The master equation is an equation for the density operator which is the quantum mechanical version of a probability distribution. The quantum trajectory can be considered as a quantum mechanical version of a stochastic trajectory.

The quantum trajectory approach is built around the standard theory of photoelectric detection and the master equation theory of a photoemissive source. The mathematical language used in the approach follows that of the theory of continu-

ous quantum measurement[55]. Since quantum trajectory theory combines the two theories, it relates the statistics of photoelectron emissions to a dynamical process involving photon emissions taking place at the source. In this approach a stochastic wavefunction describes the time-dependent state of the quantum mechanical source conditioned on a history of classical stochastic signals that appear at detectors monitoring the source system. The stochastic wavefunction evolution generates the measurement record, the numbers that appear in the laboratory. The parallel evolution of stochastic wavefunction and accompanying measurement record is called a quantum trajectory. Such a single trajectory gives a picture of what is going on in the source in a visible form. The master equation approach does not allow this concrete visualization. Thus the quantum trajectory approach clarifies the physical interpretation.

On the other hand, the quantum trajectory approach also provides a powerful computational method. We demonstrate this from the following two cases. First, when it is very hard or impossible to use the standard master equation method to deal with a large system, the quantum trajectory method may provide a way to solve the problem. This can be understood as follows.. Suppose that n is the total truncated states of the system needed in the problem. Generally, there are n^2 matrix elements of the density operator (A master equation describes a dynamic evolution of a density operator.). Thus, for 10^2 states there are 10^4 coupled differential equations which need to be solved by using the standard method. Some computers do not have enough memory to solve the 10^4 differential equations. In this situation the quantum

trajectory method perhaps can be used to solve the problem. This is because the quantum trajectory approach can be formulated in terms of wavefunction rather than density operator. For 10^2 states there are only 10^2 differential equations which need to be solved. Certainly most computers can handle this task. Second, even for some medium-size system which can fit the computer memory the quantum trajectory method may still have an advantage over the standard method in some cases. The reason is as follows. The connection between the conditioned wavefunction and the master equation is that an ensemble average, or time average, taken with respect to the conditioned wavefunction reproduces the results of a master equation calculation. Although the quantum trajectory method must solve many less equations than the standard method does, this advantage comes at the expense of taking an average over an ensemble of trajectories. In principle, to approach the results obtained from the standard method one must take an average over a large ensemble of trajectories, and This may require more computing time than the standard method does. In many cases, however, one does not necessarily need the results with very high accuracy to compare with the experimental results. Thus, only the average over a relatively small ensemble of trajectories is needed. This may lead to a less computing time needed in the quantum trajectory method compared to the standard method.

The quantum trajectory approach was born more or less for the needs in the field of cavity QED. For some cavity QED problems the standard methods are either invalid or difficult to apply, but the quantum trajectory approach provides a new

and useful way to proceed. In the following two chapters we will use the quantum trajectory approach to solve two problems related to cavity QED. To prepare for that, in this chapter we describe the quantum trajectory approach for a cavity QED system. The master equation for this system is written in a similar form to Eq. (2.6).

Here we write

$$\begin{aligned} \dot{\rho} = & (1/i\hbar)[\hat{H}, \rho] + \kappa(2\hat{a}\rho\hat{a}^\dagger - \hat{a}^\dagger\hat{a}\rho - \rho\hat{a}^\dagger\hat{a}) \\ & + (\gamma/2)(2\hat{\sigma}_-\rho\hat{\sigma}_+ - \hat{\sigma}_+\hat{\sigma}_-\rho - \rho\hat{\sigma}_+\hat{\sigma}_-), \end{aligned} \quad (5.1)$$

where the form of \hat{H} is to be specified for each example below. We hope to accomplish two things in this chapter. First, we will briefly review two types of quantum trajectories for the system modeled by Eq. (5.1), one constructed for direct photoelectric detection and the other constructed for homodyne detection. Second, we will demonstrate through familiar examples that these trajectories can provide a penetrating view of the dynamics of a quantum source system, and that an average over an ensemble of trajectories reproduces the results of a master equation calculation.

5.1 Direct Photoelectric Detection

The quantum trajectory wavefunction is denoted by $|\psi_c(t)\rangle$. The subscript c reminds us that this is a conditioned wavefunction. The fundamental connection with the master equation is given by the relation

$$\rho(t) = \overline{|\psi_c(t)\rangle\langle\psi_c(t)|} \quad (5.2)$$

where the overbar denotes an average over an ensemble of trajectories. Quantum trajectories have a physical interpretation derived from the theory of photoelectric detection. Imagine ideal detectors that record every photon lost, either as atomic fluorescence or by transmission through the cavity mirrors. The wavefunction $|\psi_c(t)\rangle$ describes the state of the open system (the atom and cavity mode) at time t , *conditioned* on a specific history of photoelectric pulses recorded at these detectors. The evolution of $|\psi_c(t)\rangle$ is most simply given in terms of the unnormalized wavefunction $|\bar{\psi}_c(t)\rangle$, where $|\psi_c(t)\rangle = |\bar{\psi}_c(t)\rangle / \sqrt{\langle \bar{\psi}_c(t) | \bar{\psi}_c(t) \rangle}$. We state the quantum trajectory equations corresponding to the master equation (5.1) as follows [56]. The conditioned wavefunction satisfies a coherent evolution between photon emissions governed by a Schrödinger equation with non-Hermitian Hamiltonian, interrupted by instantaneous collapses at the times of the photon emissions: Between photon emissions we have the Schrödinger equation

$$|\dot{\bar{\psi}}_c\rangle = (1/i\hbar)[\hat{H} - i\hbar(\gamma/2)\hat{\sigma}_+\hat{\sigma}_- - i\hbar\kappa\hat{a}^\dagger\hat{a}]|\bar{\psi}_c\rangle. \quad (5.3)$$

Photon emissions occur at random times at a rate determined by $|\psi_c(t)\rangle$. Emission out the sides of the cavity occurs at the rate

$$r_A(t) = \gamma\langle\psi_c(t)|\hat{\sigma}_+\hat{\sigma}_-|\psi_c(t)\rangle \quad (5.4)$$

and is accompanied by the wavefunction collapse

$$|\bar{\psi}_c(t)\rangle \rightarrow \hat{\sigma}_-|\bar{\psi}_c(t)\rangle. \quad (5.5)$$

The emission of a photon through the cavity mirrors occurs at the rate

$$r_C(t) = 2\kappa\langle\psi_c(t)|\hat{a}^\dagger\hat{a}|\psi_c(t)\rangle, \quad (5.6)$$

and is accompanied by the collapse

$$|\bar{\psi}_c(t)\rangle \rightarrow \hat{a}|\bar{\psi}_c(t)\rangle. \quad (5.7)$$

Using a computer, sequences of collapses are readily simulated in a Monte-Carlo fashion while simultaneously integrating Eq. (5.3). In this way we produce realizations of the quantum trajectories $|\psi_c(t)\rangle$.

We now apply the quantum trajectory approach described above to the example of resonance fluorescence. This example is relatively simple so that we might solve the trajectory equation in the problem analytically. The master equation for resonance fluorescence [57] is

$$\dot{\rho} = (1/i\hbar)[\hat{H}_{rf}, \rho] + (\gamma/2)(2\hat{\sigma}_-\rho\hat{\sigma}_+ - \hat{\sigma}_+\hat{\sigma}_-\rho - \rho\hat{\sigma}_+\hat{\sigma}_-), \quad (5.8)$$

where

$$\hat{H}_{rf} = \hbar\omega_A\hat{\sigma}_z/2 - \hbar(\Omega/2)(e^{-i\omega_A t}\hat{\sigma}_+ + e^{i\omega_A t}\hat{\sigma}_-) \quad (5.9)$$

describes the interaction of a single two-state atom with an external coherent field (proportional to the Rabi frequency Ω) on resonance, and ω_A is a resonance frequency of the atom. Correspondingly, we have the Schrödinger equation for the conditioned wavefunction between photon emissions, with

$$|\dot{\bar{\psi}}_c\rangle = (1/i\hbar)[\hat{H}_{rf} - i\hbar(\gamma/2)\hat{\sigma}_+\hat{\sigma}_-]|\bar{\psi}_c\rangle. \quad (5.10)$$

At the times of the photon emissions the wavefunction collapses according to Eq. (5.5).

The rate for a photon emission is given by Eq. (5.4).

Let us assume an initial state

$$|\bar{\psi}_c(\mathbf{0})\rangle = |\psi_c(\mathbf{0})\rangle = |l\rangle, \quad (5.11)$$

where $|l\rangle$ denotes the lower state of the two-state atom. In the presence of the driving field the atom then evolves to a new state at time t

$$|\psi_c(t)\rangle = c_l(t)|l\rangle + c_u(t)|u\rangle, \quad (5.12)$$

where $|u\rangle$ denotes the upper state of the two-state atom. The collapse (5.5) applies at the times of photon emissions. Thus, after each photon emission the atom is in its lower state. This indicates that the evolution between photon emissions always starts from the same initial state (5.11). In this way the atom continuously evolves from its lower state to a superposition state, and then makes a collapse and emits a photon. The evolution of the conditioned wavefunction is obviously governed by a stationary stochastic process. This is what one might expect to obtain by solving the master equation (5.8) [22].

From Eq. (5.10) we find that the unnormalized amplitudes $\bar{c}_l(t)$ and $\bar{c}_u(t)$ obey the equations

$$\begin{aligned} \dot{\bar{c}}_l &= i(\omega_A/2)\bar{c}_l + i(\Omega/2)e^{i\omega_A t}\bar{c}_u, \\ \dot{\bar{c}}_u &= -(\gamma/2 + i\omega_A/2)\bar{c}_u + i(\Omega/2)e^{-i\omega_A t}\bar{c}_l. \end{aligned} \quad (5.13)$$

These equations have the solutions

$$\begin{aligned}\bar{c}_l(t) &= e^{-(\gamma/4)t} e^{i\omega_A t/2} [\cosh(\theta t) + (\gamma/4\theta) \sinh(\theta t)], \\ \bar{c}_u(t) &= i e^{-(\gamma/4)t} e^{-i\omega_A t/2} (\Omega/2\theta) \sinh(\theta t),\end{aligned}\tag{5.14}$$

where

$$2\theta = \sqrt{(\gamma/2)^2 - \Omega^2}.\tag{5.15}$$

The rate for photon emission is then given by

$$\gamma_A = \gamma |c_u(t)|^2 = \gamma \frac{|\bar{c}_u(t)|^2}{|\bar{c}_l(t)|^2 + |\bar{c}_u(t)|^2}.\tag{5.16}$$

Figure 5.1 shows two examples of quantum trajectories for resonance fluorescence in which the conditioned upper state probability $\langle \hat{\sigma}_+ \hat{\sigma}_- \rangle_c = |c_u(t)|^2$ is plotted. The vertical jumps occur at the times of the photon emissions. Every emission collapses the atom to its lower state – $\langle \hat{\sigma}_+ \hat{\sigma}_- \rangle_c \rightarrow 0$. The collapse is responsible for photon antibunching in resonance fluorescence. Photon antibunching means that it is improbable to see two photon emissions during any time interval that is short compared to the atomic lifetime. From these trajectories we can see exactly how the photon antibunching happens in resonance fluorescence. After each photon emission the atom is certainly in its ground state. In order to be able to emit a second photon, the atom must first evolve back to the upper state, a process that takes an average time on the order of the Rabi frequency. For strong excitation Fig. 5.1(b) shows a coherent Rabi oscillation between the emissions. The oscillation is caused by the dynamic Stark splitting due to the interaction of the atom with the strong driving field.

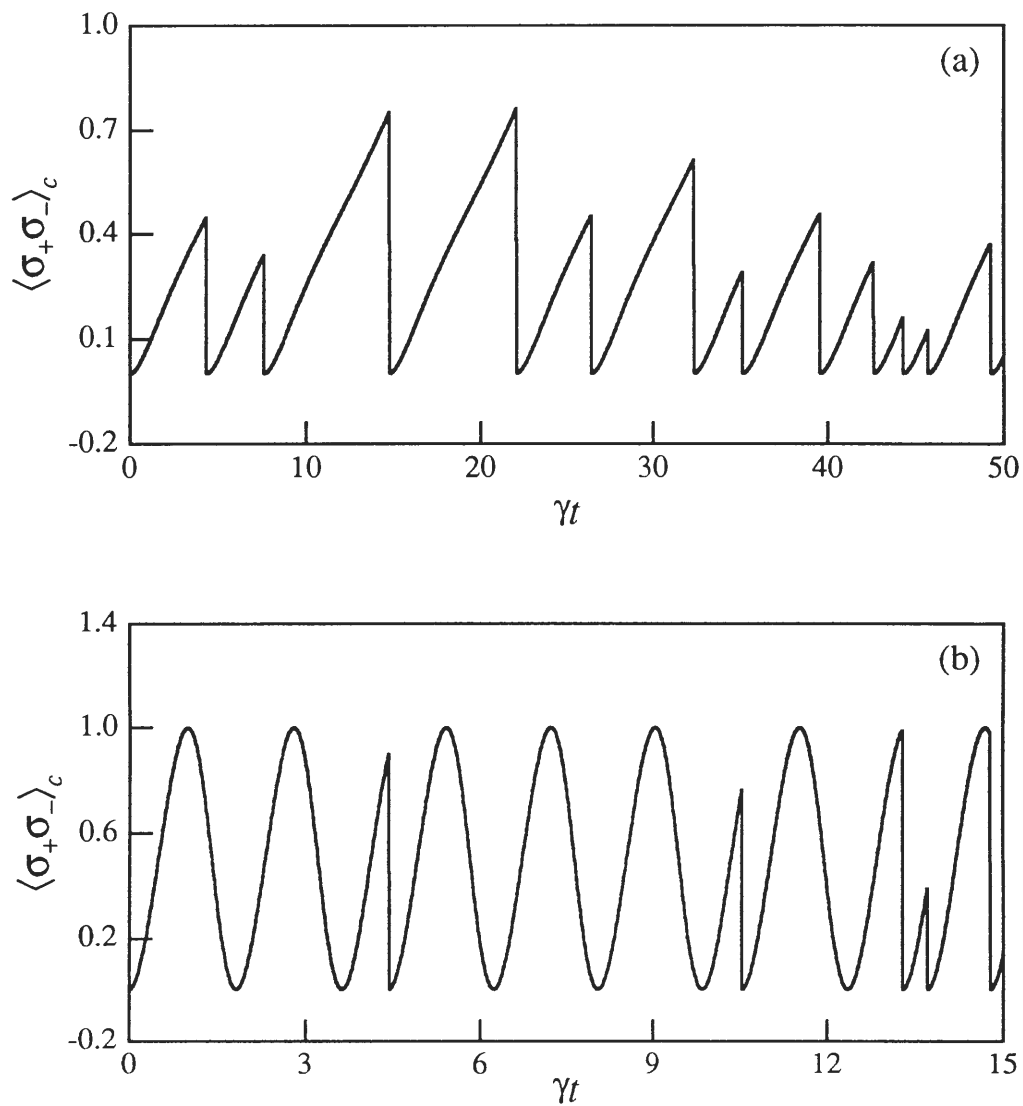


Figure 5.1. Sample quantum trajectories showing the conditioned upper state probability of the atom undergoing resonance fluorescence. (a) Weak excitation, $\Omega/\gamma = 0.7$; (b) strong excitation, $\Omega/\gamma = 3.5$.

Let us now construct photon counting distributions and waiting time distributions from simulations like those illustrated in Fig. 5.1. We simply count the number of photon emissions for a certain counting time interval and then repeat the process for many such intervals. Thus we build up a histogram of the number of photon emissions occurring during the counting time – a histogram of the number of photoelectron counts. By normalizing such a histogram we obtain the photoelectron counting distribution. In the same way the waiting time distribution $w(\tau)$ can also be obtained from a histogram of the time intervals between successive photoelectron emissions. Figures 5.2 and 5.3 show two examples of such waiting time distributions obtained from simulations of Fig. 5.1. Notice that $w(0) = 0$ in these figures. This corresponds to photon antibunching in resonance fluorescence. A peaked distribution in Figures 5.2 and 5.3 reveals a tendency for photon emissions to occur at regularly spaced times. The insets in these figures show the waiting time distributions which were calculated analytically from the master equation approach in [57]. It can be seen that the agreement is very good. An ensemble average taken with respect to quantum trajectories does reproduce the results of a master equation calculation. It can also be seen that residual sampling fluctuations appear in the numerical simulations which are much like those expected in a laboratory experiment.

The quantum trajectories we have described so far come from a decomposition of the master equation based on direct photoelectric detection. We call such a decomposition an unraveling of the master equation. Other idealized measurements

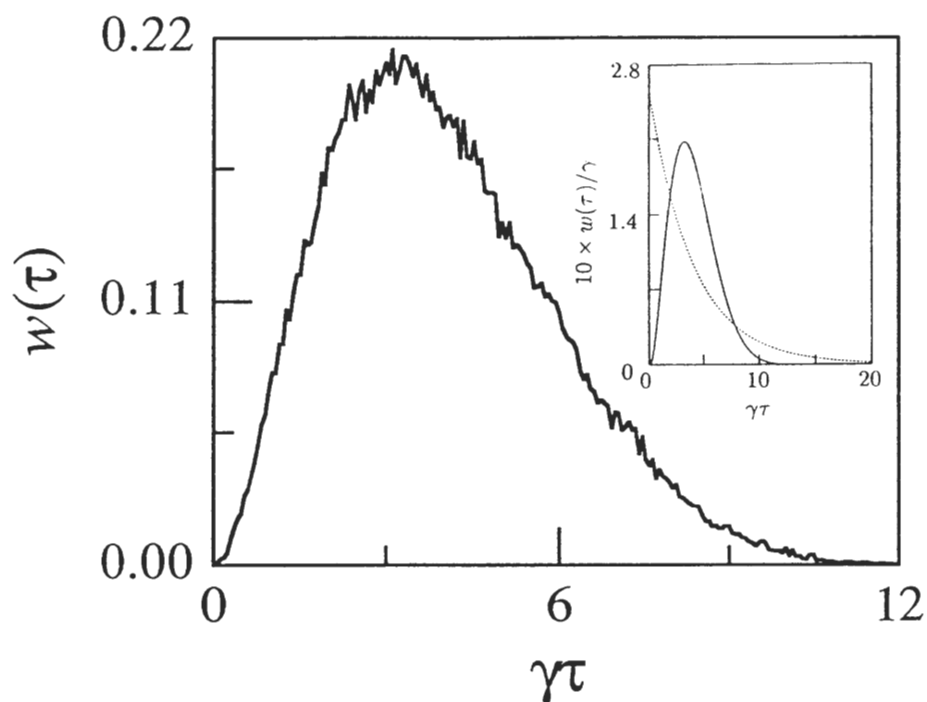


Figure 5.2. Waiting time distribution for resonance fluorescence obtained from the simulation of Fig. 5.1(a). The inset shows the distribution calculated analytically in [52]

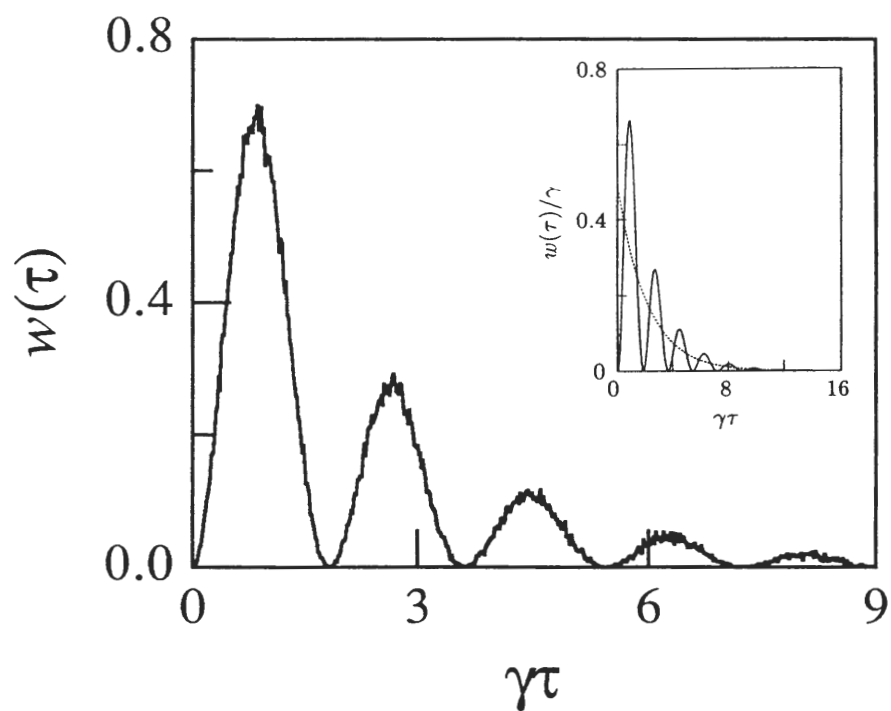


Figure 5.3. Waiting time distribution for resonance fluorescence obtained from the simulation of Fig. 5.1(b). The inset shows the distribution calculated analytically in [52]

give different unravelings, and quite different quantum trajectories. One example is homodyne detection. A quantum trajectory based on homodyne detection produces a continuous evolution of the conditioned wavefunction. Such a wavefunction will be described in the following section and will be used in chapter VII.

5.2 Homodyne Detection

In homodyne detection the field to be detected (signal field) is combined at a beam splitter with a strong local oscillator field. The sum field then illuminates a photoelectric detector. The measurement record at the detector is a stochastic photocurrent. In a realistic homodyne measurement the amplitude of the local oscillator field is many orders of magnitude larger than that of the signal field. Therefore the stochastic photocurrent is composed of only three components: a d. c. component proportional to the photon flux of the local oscillator, a shot noise component proportional to the square root of the local oscillator photon flux, and a component due to the interference of the local oscillator and signal fields, also proportional to the square root of the local oscillator photon flux. In balanced detection the d. c. component is removed leaving only the shot noise and signal components [58].

The homodyne measurement record is still a counting process. It is not sensible, however, to proceed with direct counting trajectories as before. The reason for this is that the local oscillator photon flux is much larger than that of the signal so there is an extremely small change produced in the signal state by one collapse of

the combined system of signal plus local oscillator. Physically this means that a photoelectron emission probably corresponds to the annihilation of a local oscillator photon, with only a small probability that a photon was annihilated from the signal field. The sensible approach under these conditions is to take a continuous evolution limit. The two pieces of the quantum trajectory evolution, coherent plus collapse, can then be combined into a single stochastic Schrödinger equation for the conditioned wavefunction of the signal. In this case, the wavefunction is conditioned on the history of the stochastic photocurrent realized by an ideal homodyne detector rather than on a sequence of pulses seen in direct photoelectric detection. The quantum trajectories generated from this wavefunction also satisfy Eq. (5.2). We now state the quantum trajectory equations for the system modeled by Eq. (5.1) based on homodyne detection of the field transmitted through the cavity mirrors, still using direct photoelectric detection to track the fluorescence from the atom:

In between atomic emissions the (unnormalized) conditioned wavefunction satisfies the stochastic Schrödinger equation

$$|\dot{\bar{\psi}}_c\rangle = (1/i\hbar)[\hat{H} - i\hbar(\gamma/2)\hat{\sigma}_+\hat{\sigma}_- - i\hbar\kappa\hat{a}^\dagger\hat{a} + i\hbar\xi(t)e^{i(\omega_L t - \phi)}\sqrt{2\kappa}\hat{a}]|\bar{\psi}_c\rangle, \quad (5.17)$$

with

$$\xi(t) = \sqrt{2\kappa}\langle\bar{\psi}_c|(e^{-i(\omega_L t - \phi)}\hat{a}^\dagger + e^{i(\omega_L t - \phi)}\hat{a})|\bar{\psi}_c\rangle + \mu(t), \quad (5.18)$$

where ϕ is the phase of the local oscillator and $\mu(t)$ is a Gaussian white noise associated with the local oscillator shot noise. As before, the atomic emissions occur randomly at the rate $r_A(t)$ (Eq. 5.4), and each atomic emission is accompanied by a wavefunction

collapse (Eq. 5.5). The quantity $\xi(t)$ is related to the homodyne photocurrent $I(t)$.

For a broad detection bandwidth we write

$$I(t) = Ge \left[f + \sqrt{f} \xi(t) \right], \quad (5.19)$$

where e is the electronic charge, G is the gain, and $f \gg 2\kappa \langle \bar{\psi}_c | \hat{a}^\dagger \hat{a} | \bar{\psi}_c \rangle$ is the local oscillator photon flux.

The example we consider here to illustrate the homodyne detection trajectories is the degenerate parametric oscillator. This system includes two cavity modes coupled by a nonlinearity. One mode is a pump mode with frequency $2\omega_c$ and the other is a subharmonic mode with frequency ω_c . The pump mode is driven by a classical field injected into the cavity. The output of the cavity is a source of the subharmonic. Here we are only interested in below threshold operation. In this case, the coupling between fluctuations in the pump mode and the subharmonic mode disappears so that we can obtain separate master equations for each of the modes. Thus we have the master equation for the subharmonic mode

$$\dot{\rho} = (1/i\hbar)[\hat{H}_{dpo}, \rho] + \kappa(2\hat{a}\rho\hat{a}^\dagger - \hat{a}^\dagger\hat{a}\rho - \rho\hat{a}^\dagger\hat{a}), \quad (5.20)$$

where

$$\hat{H}_{dpo} = \hbar\omega_c\hat{a}^\dagger\hat{a} + (\kappa\lambda/2)(\hat{a}^{\dagger 2}e^{-i2\omega_c t} - \hat{a}^2e^{i2\omega_c t}). \quad (5.21)$$

Here λ is the pump parameter which is proportional to the amplitude of the pump field. The stochastic Schrödinger equation corresponding to Eq. (5.20) is given by

$$|\dot{\bar{\psi}}_c\rangle = (1/i\hbar)[\hat{H}_{dpo} - i\hbar\kappa\hat{a}^\dagger\hat{a} + i\hbar\xi(t)e^{i(\omega_c t - \phi)}\sqrt{2\kappa}\hat{a}]|\bar{\psi}_c\rangle. \quad (5.22)$$

From Eqs. (5.21) and (5.22) we can simulate quantum trajectories based on homodyne detection for the degenerate parametric oscillator modeled by Eq. (5.20). Before doing this we simulate quantum trajectories based on direct photoelectric detection for this system using Eqs. (5.6), (5.7), (5.21) and (5.22) without the term proportional to $\xi(t)$. We then compare the quantum trajectories based on direct photoelectric detection and those based on homodyne detection.

Figure 5.4 shows a sample quantum trajectory for the conditioned mean photon number $\langle \hat{a}^\dagger \hat{a} \rangle_c = \langle \psi_c | \hat{a}^\dagger \hat{a} | \psi_c \rangle$ based on direct photoelectric detection. It is very surprising that the trajectory shows not only a downwards jump as seen before, but also an upwards jump. We know that the jump occurs at the time of a photon emission. How can the photon emission cause the upwards jump in the conditioned mean photon number – how can the photon emission make the number of photons in the cavity increase? The explanation is as follows. The conditioned mean photon number is the mean of $\hat{a}^\dagger \hat{a}$ with respect to a state that is conditioned on the specific history of photon emissions and coherent evolutions along the trajectory. It is not an actual photon number out there in the cavity, but it propagates information and tells us what is going on in the source. For the degenerate parametric oscillator the photons are created in pairs inside the cavity. The observation of the first photon of a pair means the second is very likely immediately following the first. Thus when the first photon is emitted from the cavity the collapse increases the conditioned mean photon number and gives an upwards jump; this ensures that the second photon will be

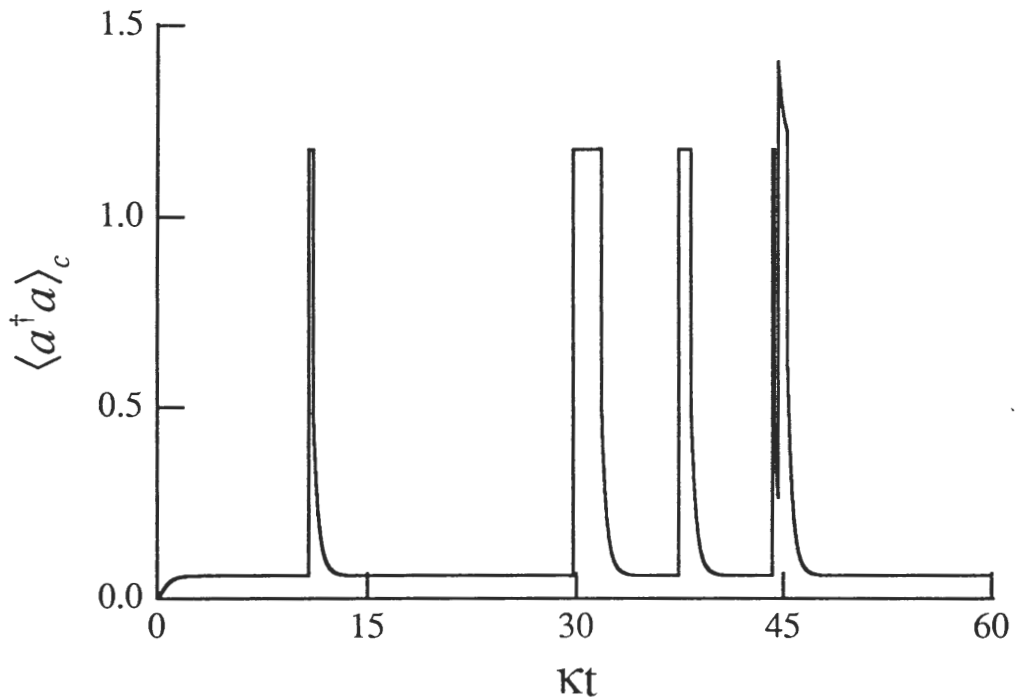


Figure 5.4. Sample quantum trajectory based on direct photoelectric detection showing the conditioned mean photon number for a degenerate parametric oscillator (DPO) operated 50% below threshold ($\lambda = 0.5$). The pump light is turned on at $t = 0$. The Fock state basis is truncated at 10 photons.

emitted within a short time [$\sim (2\kappa)^{-1}$] after the first. After the second photon of a pair has been emitted the collapse decreases the conditioned mean photon number (which in a few cavity lifetimes returns to its steady-state value) and gives a downwards jump; this ensures that no photon will be emitted for a long time compared to a cavity lifetime after a pair of photons has been emitted.

A quite different trajectory is obtained by modeling homodyne detection. Fig. 5.5 shows two sample quantum trajectories for the conditioned mean photon number for two different choices of the local oscillator phase. One choice corresponds to a measurement of the unsqueezed quadrature X of the fluctuating field amplitude and the other corresponds to a measurement of the squeezed quadrature Y . Comparing these two trajectories with the trajectory shown in Fig. 5.4, we see that there is nothing alike between them. Even for the two trajectories themselves shown in Fig. 5.5, qualitative differences can be seen: one shows much larger fluctuations than the other. However, in the mean there are no differences among all three of these trajectories. They are complementary unravelings of the quantum average $\text{tr}[\rho(t)\hat{a}^\dagger\hat{a}]$ (note that $\rho(t)$ here is not the conditioned density operator): the time averages of all three trajectories give exactly the same results, for the mean photon number in the cavity.

Fig. 5.6 shows two sample quantum trajectories for the fluctuating conditioned field amplitudes $\langle\bar{\psi}_c|(e^{i\phi}\hat{a}^\dagger + e^{-i\phi}\hat{a})|\bar{\psi}_c\rangle$ based on homodyne detection. In contrast to this figure, the conditioned field amplitudes are zero at all times for the trajectories based on direct photoelectric detection. By comparing the quantum trajectories based

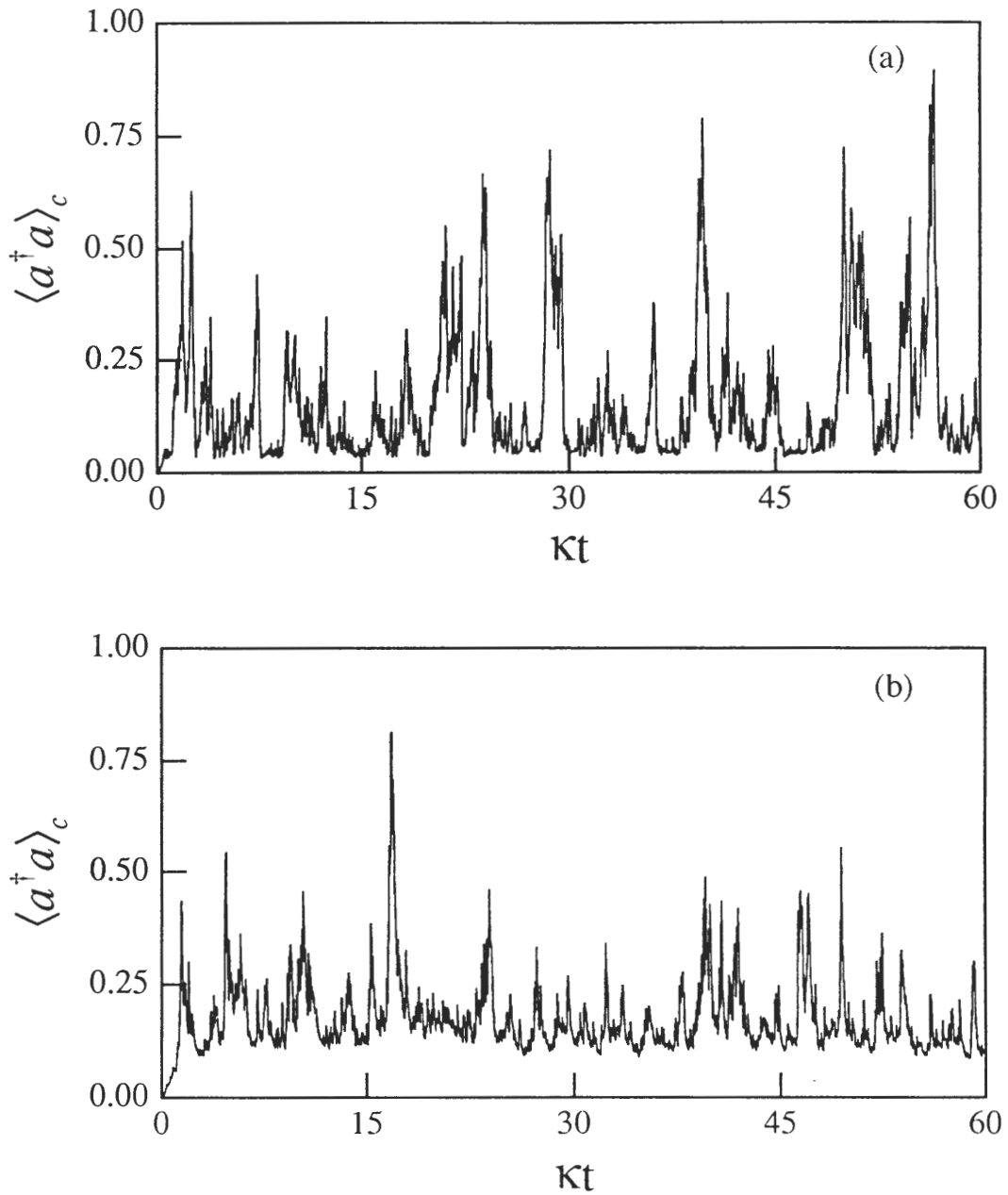


Figure 5.5. Sample quantum trajectories based on homodyne detection showing the conditioned mean photon number for a degenerate parametric oscillator (DPO) operated 10% below threshold ($\lambda = 0.9$). (a) $\langle \hat{a}^\dagger \hat{a} \rangle_c$ for X - quadrature ($\theta = 0$); (b) $\langle \hat{a}^\dagger \hat{a} \rangle_c$ for Y - quadrature ($\theta = \pi/2$).

on direct photoelectric detection and those based on homodyne detection, we see clearly that different measurements give different trajectories – different pictures of what is going on in the source, suited to help us understand different aspects of the physics.

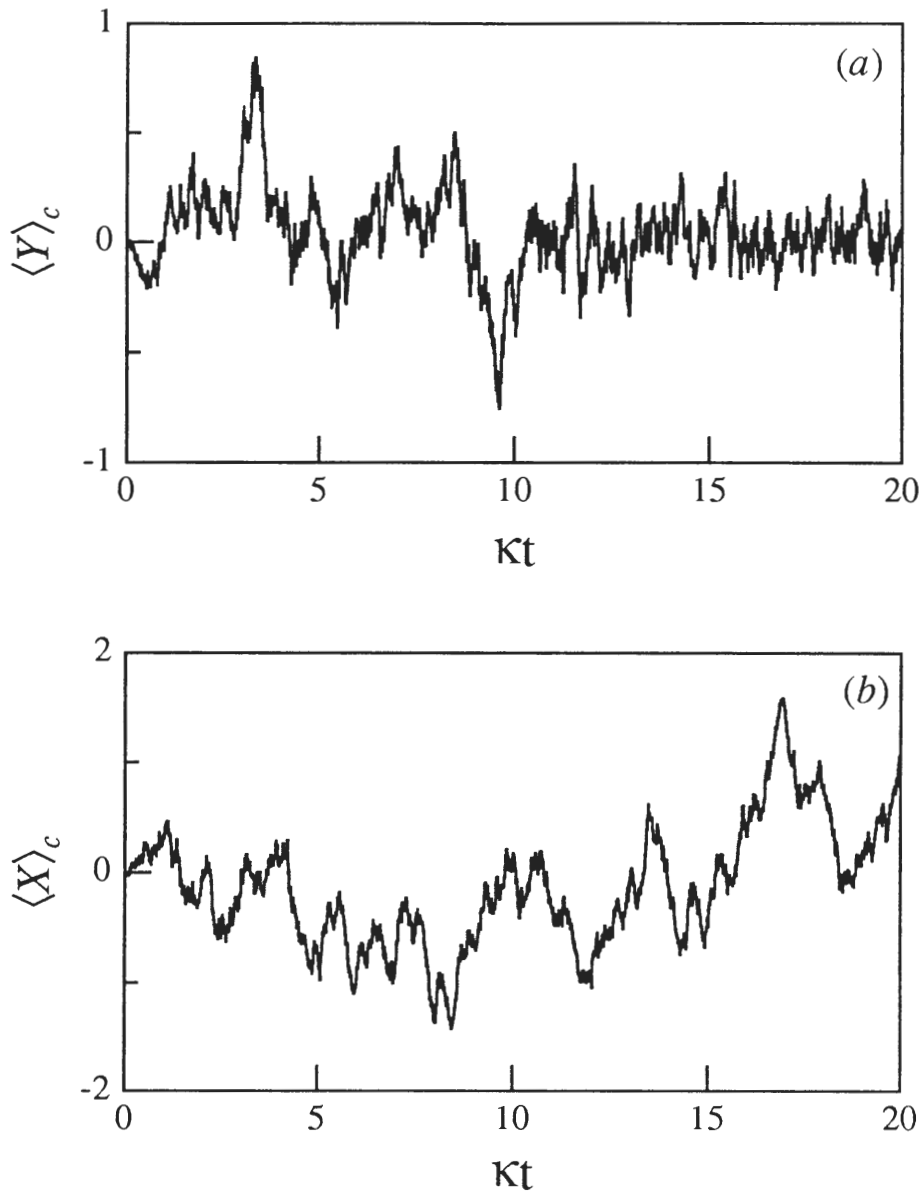


Figure 5.6. Sample quantum trajectories based on homodyne detection showing the conditioned mean field quadrature amplitudes for a degenerate parametric oscillator (DPO) operated 30% below threshold ($\lambda = 0.7$). (a) The Y amplitude for Y - quadrature ($\theta = \pi/2$); (b) the X amplitude for X - quadrature ($\theta = 0$).

CHAPTER VI

TWO-STATE BEHAVIOR

In chapters II – IV, we have demonstrated the quantum nature of the system formed by a coupled cavity mode and atom. This system can be viewed as a “molecule”. In this chapter we consider direct excitation of the “molecule” resonances – we tune the driving field to one of the “vacuum” Rabi resonances. From the analogy with molecular spectroscopy, we then expect that for sufficiently large dipole coupling the atom-cavity “molecule” behaves as a two-state system. We will demonstrate this behavior in a computer experiment based on the quantum trajectory simulations described in chapter V. In particular, we will show that the light transmitted by the cavity and the light emitted out the sides of the cavity by the atom have the photoelectron counting statistics of resonance fluorescence and a Mollow triplet spectrum for strong driving field intensities.

6.1 Photoelectron Counting Statistics

In chapter II we considered a strongly coupled atom and cavity mode driven by a coherent field. We studied the intensity of the field transmitted by the cavity as a function of the detuning of the driving field from the resonance frequency of the atom and cavity mode for a fixed amplitude of the driving field. Here we tune the coherent driving field to the lower “vacuum” Rabi resonance of the coupled system

(as illustrated in Fig. 6.1) – we fix the detuning $\Delta = g$. Thus the master equation to describe the coupled system is the same as the equation (2.10) (in the interaction picture), but with the fixed detuning g . Therefore, the quantum trajectory equations (5.3) – (5.7) can be used here with the Hamiltonian (in the interaction picture)

$$\hat{H} = \hbar g (\hat{a}^\dagger \hat{a} + 1/2 \hat{\sigma}_z) + i\hbar g (\hat{a}^\dagger \hat{\sigma}_- - \hat{a} \hat{\sigma}_+) + i\hbar \mathcal{E} (\hat{a}^\dagger - \hat{a}). \quad (6.1)$$

From what we learned about quantum trajectory theory in the previous chapter, we expect even a single quantum trajectory may show some features about the source system. Let us now see such a single trajectory, shown in Fig. 6.2, where we plot the conditioned averages that appear on the right-hand sides of Eqs. (5.4) and (5.6). The quantum trajectory is simulated based on Eqs. (5.3)–(5.7) and Eq. (6.1). It shows a fast coherent modulation at the detuning frequency $2g$ from the upper “vacuum” Rabi resonance. It also shows an oscillation at a much lower frequency (seen most clearly for $1.5 < \kappa t < 3.0$). This is caused by the dynamic Stark splitting as depicted in Fig. 6.1 [59]. The simplest model for this behavior is the two-state approximation

$$\begin{aligned} \hat{H} &= i\hbar(\gamma/2)\hat{\sigma}_+\hat{\sigma}_- - i\hbar\kappa\hat{a}^\dagger\hat{a} \\ &= -\hbar(\mathcal{E}/\sqrt{2})(\hat{l}_+ + \hat{l}_-) - (i\hbar/2)(\kappa + \gamma/2)\hat{l}_+\hat{l}_-, \end{aligned} \quad (6.2)$$

where $\hat{l}_+ = |1, l\rangle\langle g|$ and $\hat{l}_- = (\hat{l}_+)^\dagger$. Eqs. (5.4)–(5.7) are now read with $\hat{\sigma}_- \rightarrow (1/\sqrt{2})\hat{l}_-$ and $\hat{a} \rightarrow (-i/\sqrt{2})\hat{l}_-$. The Rabi frequency for this two-state system is $\sqrt{2}\mathcal{E}$ which agrees quite well with the modulation frequency observed in Fig. 6.2. Note that this frequency is independent of the dipole coupling constant g .

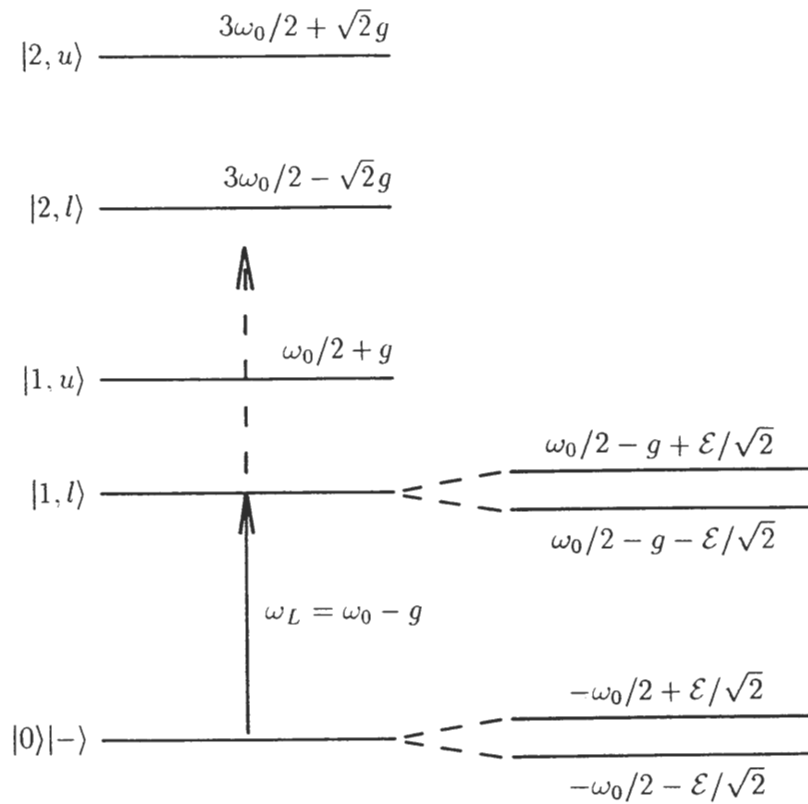


Figure 6.1. Energy-level diagram showing the excitation of the lower “vacuum” Rabi resonance and the resulting dynamic Stark splitting.

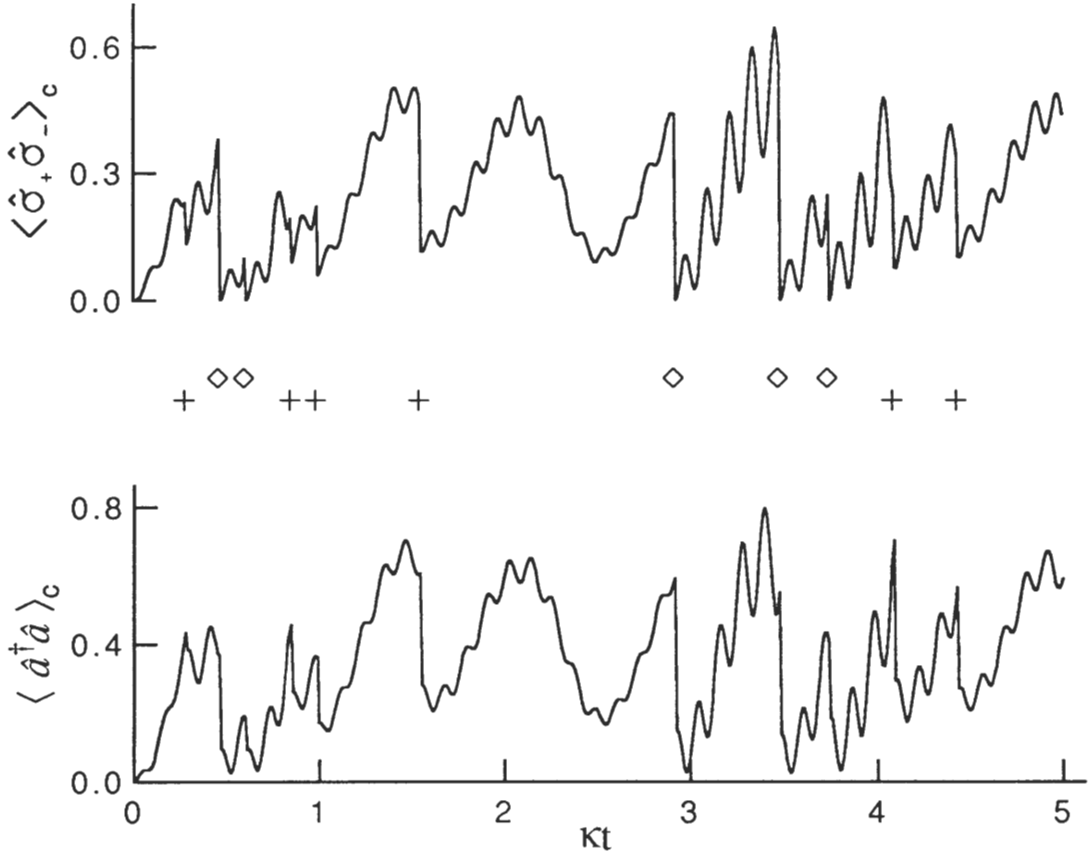


Figure 6.2. Sample quantum trajectory for $\gamma/2\kappa = 1$, $g/\kappa = 25$, and $\mathcal{E}/\kappa = 5$. $\langle \hat{\sigma}_+ \hat{\sigma}_- \rangle_c$ and $\langle \hat{a}^\dagger \hat{a} \rangle_c$ are the conditioned upper state probability of the atom and the conditioned mean photon number inside the cavity, respectively. \diamond and $+$ mark the times of photon emissions from the atom and cavity, respectively.

The two-state approximation is not suitable for a quantitative study. For example, the modulation at frequency $2g$ is absent in the two-state approximation. Also, in the two-state approximation every emission collapses the coupled system to its ground state – $\langle \hat{\sigma}_+ \hat{\sigma}_- \rangle_c \rightarrow 0$, $\langle \hat{a}^\dagger \hat{a} \rangle_c \rightarrow 0$; this does not happen in Fig. 6.2 (although emissions from the atom do collapse the atom to its lower state – $\langle \hat{\sigma}_+ \hat{\sigma}_- \rangle_c \rightarrow 0$).

Using a five-state basis, however, we can show that the two-state approximation is quantitatively good when the dipole coupling is sufficiently large. We solve Eqs. (5.3) and (6.1) in the five-state basis $|g\rangle$, $|1, l\rangle$, $|1, u\rangle$, $|2, l\rangle$, and $|2, u\rangle$. We write the conditioned wavefunction in the form

$$|\dot{\psi}_c\rangle = c_g(t)|g\rangle + c_{1,l}(t)|1, l\rangle + c_{1,u}(t)|1, u\rangle + c_{2,l}(t)|2, l\rangle + c_{2,u}(t)|2, u\rangle. \quad (6.3)$$

From Eqs. (5.3), (6.1) and (6.3), we find that the unnormalized amplitudes $\bar{c}_g(t)$, $\bar{c}_{1,l}(t)$, $\bar{c}_{1,u}(t)$, $\bar{c}_{2,l}(t)$, and $\bar{c}_{2,u}(t)$ obey the coupled equations

$$\begin{aligned} \dot{\bar{c}}_g &= i(g/2)\bar{c}_g + i(\mathcal{E}/\sqrt{2})(\bar{c}_{1,l} - \bar{c}_{1,u}), \\ \dot{\bar{c}}_{1,l} &= i(\mathcal{E}/\sqrt{2})\bar{c}_g + i(g/2 - \alpha)\bar{c}_{1,l} + \beta_3\bar{c}_{1,u} - \mathcal{E}_1\bar{c}_{2,l} + \mathcal{E}_2\bar{c}_{2,u}, \\ \dot{\bar{c}}_{1,u} &= -i(\mathcal{E}/\sqrt{2})\bar{c}_g + \beta_3\bar{c}_{1,l} - (i3g/2 + \alpha)\bar{c}_{1,u} + \mathcal{E}_2\bar{c}_{2,l} - \mathcal{E}_1\bar{c}_{2,u}, \\ \dot{\bar{c}}_{2,l} &= \mathcal{E}_1\bar{c}_{1,l} - \mathcal{E}_2\bar{c}_{1,u} + [i(\sqrt{2} - 3/2)g - \beta_1]\bar{c}_{2,l} + \beta_3\bar{c}_{2,u}, \\ \dot{\bar{c}}_{2,u} &= -\mathcal{E}_2\bar{c}_{1,l} + \mathcal{E}_1\bar{c}_{1,u} + \beta_3\bar{c}_{2,l} - [i(\sqrt{2} + 3/2)g + \beta_1]\bar{c}_{2,u}, \end{aligned} \quad (6.4)$$

where $\alpha = (\kappa + \gamma/2)/2$, $\beta_1 = (3\kappa + \gamma/2)/2$, $\beta_3 = (\kappa - \gamma/2)/2$, $\mathcal{E}_1 = (1 + \sqrt{2})\mathcal{E}/2$, and $\mathcal{E}_2 = (\sqrt{2} - 1)\mathcal{E}/2$. We make the transformation

$$\bar{c}_i = \tilde{c}_i e^{igt/2} \quad (i = g; 1, l; 1, u; 2, l; 2, u), \quad (6.5)$$

and have

$$\begin{aligned}
\dot{\tilde{c}}_g &= i(\mathcal{E}/\sqrt{2})(\tilde{c}_{1,l} - \tilde{c}_{1,u}) \\
\dot{\tilde{c}}_{1,l} &= i(\mathcal{E}/\sqrt{2})\tilde{c}_g - \alpha\tilde{c}_{1,l} + \beta_3\tilde{c}_{1,u} - \mathcal{E}_1\tilde{c}_{2,l} + \mathcal{E}_2\tilde{c}_{2,u} \\
\dot{\tilde{c}}_{1,u} &= -i(\mathcal{E}/\sqrt{2})\tilde{c}_g + \beta_3\tilde{c}_{1,l} - (i2g + \alpha)\tilde{c}_{1,u} + \mathcal{E}_2\tilde{c}_{2,l} - \mathcal{E}_1\tilde{c}_{2,u} \\
\dot{\tilde{c}}_{2,l} &= \mathcal{E}_1\tilde{c}_{1,l} - \mathcal{E}_2\tilde{c}_{1,u} + [i(\sqrt{2} - 2)g - \beta_1]\tilde{c}_{2,l} + \beta_3\tilde{c}_{2,u} \\
\dot{\tilde{c}}_{2,u} &= -\mathcal{E}_2\tilde{c}_{1,l} + \mathcal{E}_1\tilde{c}_{1,u} + \beta_3\tilde{c}_{2,l} - [i(\sqrt{2} + 2)g + \beta_1]\tilde{c}_{2,u},
\end{aligned} \tag{6.6}$$

From Eqs. (6.6) we see that, for very large dipole coupling, it is a good approximation to drop the terms in $\tilde{c}_{1,u}$, $\tilde{c}_{2,l}$, and $\tilde{c}_{2,u}$, since these terms oscillate at frequencies proportional to g . Thus a set of five coupled equations reduces to a pair of coupled equations

$$\begin{aligned}
\dot{\tilde{c}}_g &= i(\mathcal{E}/\sqrt{2})\tilde{c}_{1,l} \\
\dot{\tilde{c}}_{1,l} &= i(\mathcal{E}/\sqrt{2})\tilde{c}_g - \alpha\tilde{c}_{1,l}.
\end{aligned} \tag{6.7}$$

After transforming Eq. (5.13) into the interaction picture, we see that Eq. (6.7) is the same as Eq. (5.13) describing the resonance fluorescence of a two-state atom, with the correspondence $\sqrt{2}\mathcal{E} \leftrightarrow \Omega$ and $\alpha \leftrightarrow \gamma/2$. The results that follow were obtained using a basis truncated at the six photon level.

We check first whether the coupled cavity mode and atom saturates like a two-state system. Figure 6.3 shows results for different dipole coupling strengths, where we expect saturated steady-state averages $\langle \hat{\sigma}_+ \hat{\sigma}_- \rangle = \langle \hat{a}^\dagger \hat{a} \rangle = 1/4$ for the $|g\rangle \rightarrow |1, l\rangle$ transition. These results were actually calculated by direct inversion of the standard

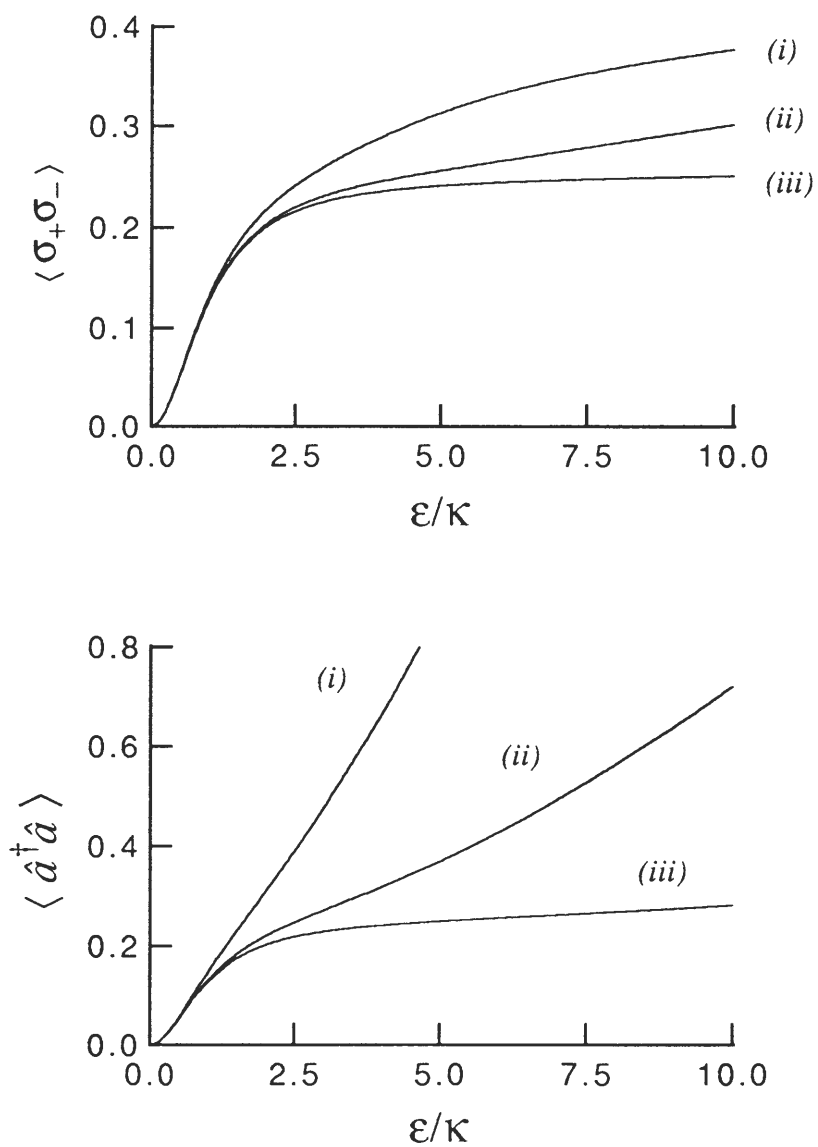


Figure 6.3. Approximate two-state saturation for $\gamma/2\kappa = 1$ and (i) $g/\kappa = 10$, (ii) $g/\kappa = 25$, and (iii) $g/\kappa = 100$.

density matrix equation, but in our simulations time averaging conditioned averages produced the same answers. We see that two-state saturation occurs over a substantial range of \mathcal{E}/κ for large values of g . Of course, it eventually breaks down as \mathcal{E}/κ continues to increase as two-photon transitions to the state $|2, l\rangle$ become important.

We now use quantum trajectories to simulate photon counting measurements on the light transmitted by the cavity and the light emitted out the sides of the cavity by the atom. From the time intervals between photon emissions we obtain the waiting time distributions $w_A(\tau)$, $w_C(\tau)$, and $w_{AC}(\tau)$. These are the distributions of the time intervals between photons emitted by the atom, the cavity, and the atom or cavity, respectively. We also divide the total time into counting intervals of duration T and sum the photon emissions in each interval to obtain photon counting distributions. The results are shown in Figs. 6.4 and 6.5.

Figure 6.4 shows the waiting time distributions and the photon counting distribution $P_{AC}(n)$ for a weak driving field. The waiting time distributions show photon antibunching and the photon counting distribution is sub-Poissonian. These results are essentially those for resonance fluorescence [compare Fig. 5.2 in chapter V]. The only departure is the less than perfect collapse to the ground state for photon emissions from the cavity, evidenced by the fact that $W_C(0)$ and $W_{AC}(0)$ are not zero. This is a consequence of the small probability for occupying states $|1, u\rangle$ and $|2, l\rangle$. Figure 6.5 shows the waiting time distributions for a strong driving field. Here the departure from a two-state cavity collapse is more obvious, and in addition, the modulation at

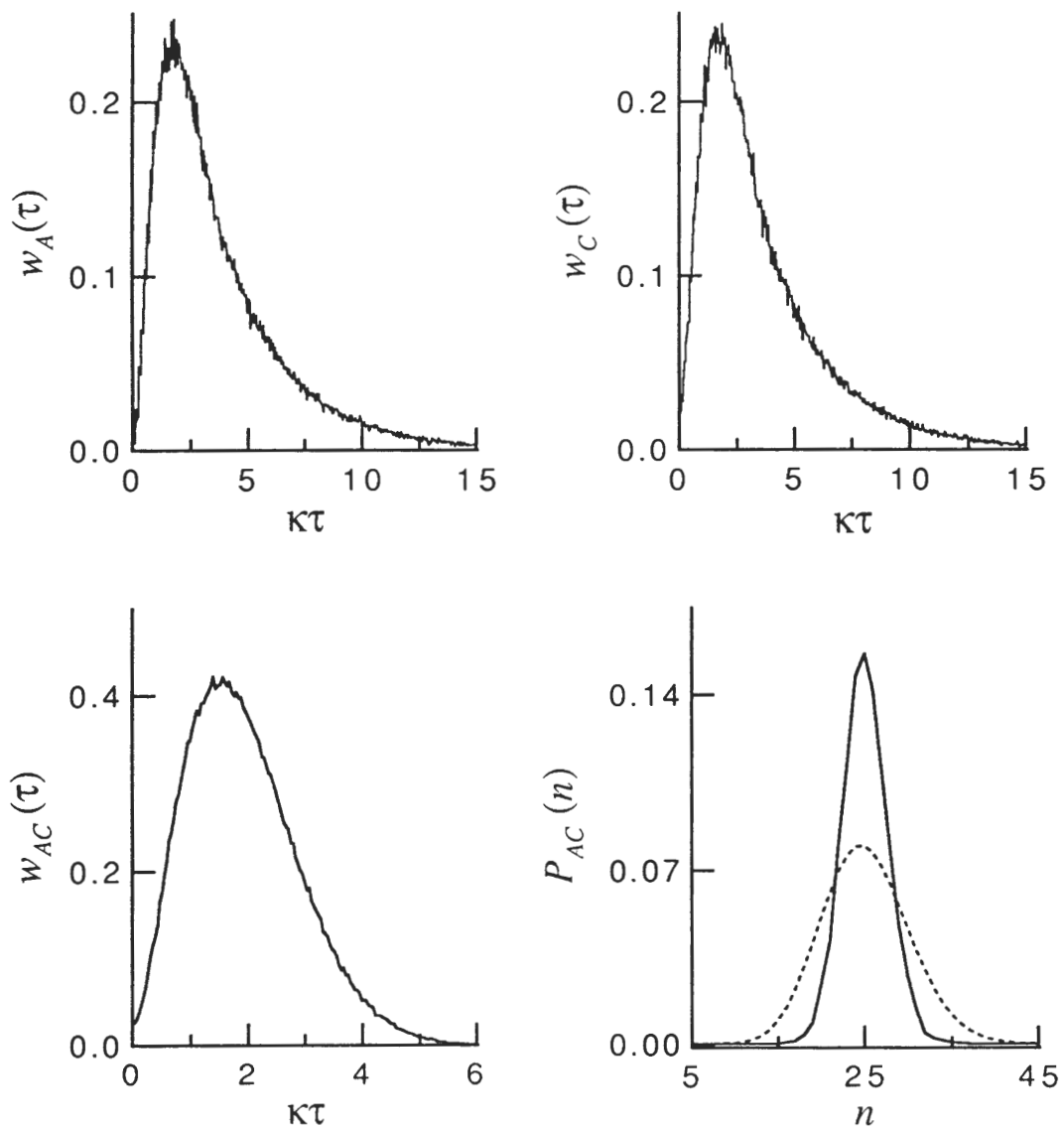


Figure 6.4. Results of simulated photon counting measurements for $\gamma/2\kappa = 1$, $g/\kappa = 25$, and $\mathcal{E}/\kappa = 1$. The photon counting distribution $P_{AC}(n)$ is compared with a Poisson distribution (dashed curve) with the same mean.

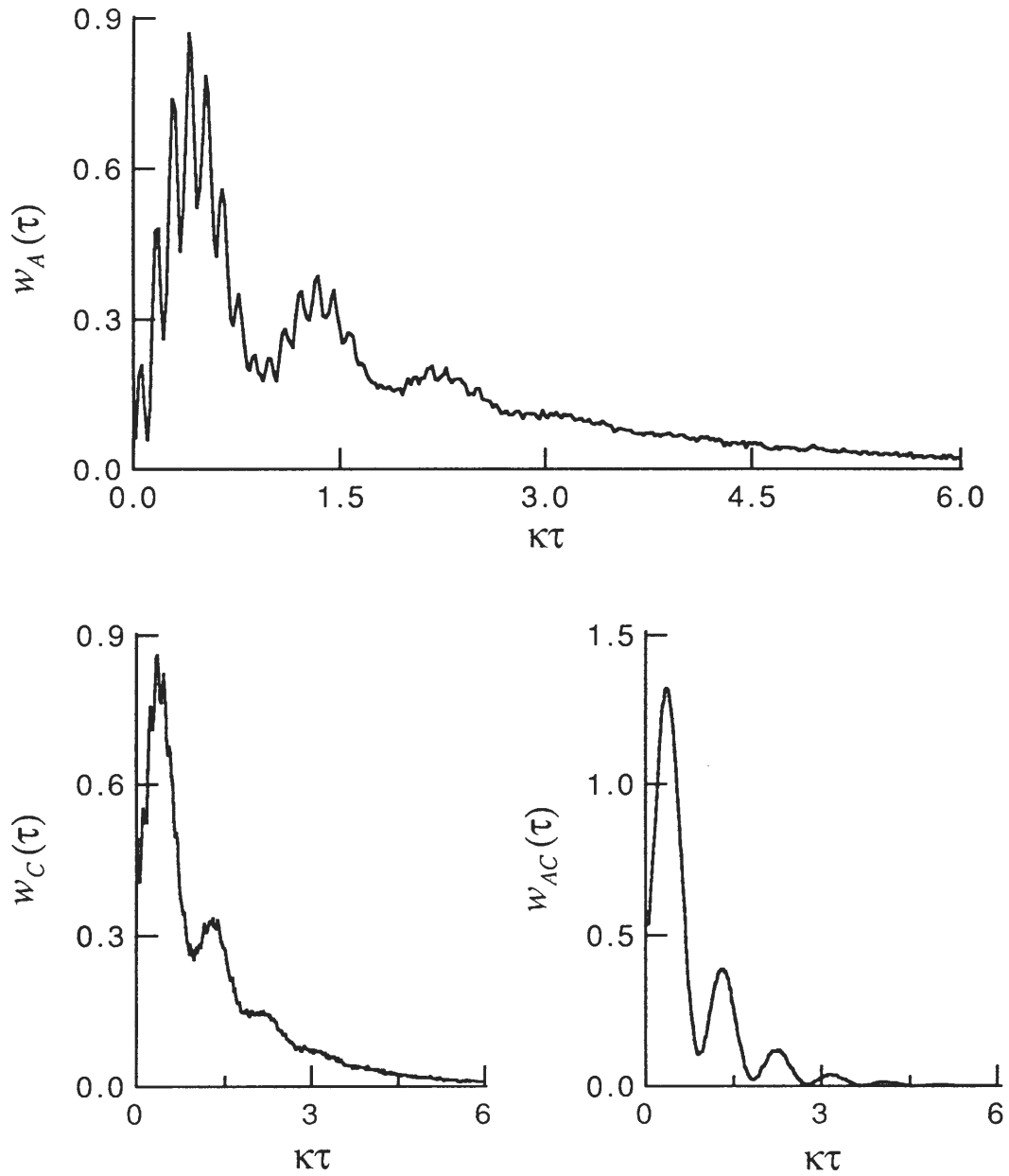


Figure 6.5. Results of simulated photon counting measurements for $\gamma/2\kappa = 1$, $g/\kappa = 25$, and $\mathcal{E}/\kappa = 5$.

frequency $2g$ is now in evidence. However, $w_{AC}(\tau)$ still resembles the waiting time distribution for resonance fluorescence [compare Fig. 5.3 in chapter V]. The oscillation in $w_{AC}(\tau)$ provides a signature in the time domain of the dynamic Stark splitting. In the next section we will discuss this Stark splitting in the frequency domain through the optical spectrum of the coupled cavity mode and atom.

6.2 Optical Spectrum

In the last section we demonstrated two-state behavior in simulated measurements of the photoelectron waiting time distribution and the photoelectron counting distribution. Let us now see the two-state behavior exhibited in the optical spectrum.

As we have seen in the last section, the dipole coupling must be quite large for the two-state approximation to be good, since the detunings from the states $|1, u\rangle$ and $|2, l\rangle$ are only $2g$ and $(2 - \sqrt{2})g$, respectively. Nonetheless, the two-state approximation allows us to make reliable qualitative predictions. Thus, we expect the spectrum of the light transmitted by the cavity and the spectrum of the fluorescence from the atom to both be given by the same Mollow spectrum [60]; for strong excitation they should both be a Mollow triplet.

Figure 6.6 shows examples of these spectra calculated numerically (without the two-state approximation) for a fixed amplitude of the driving field and different values of the dipole coupling constant. These spectra are calculated by traditional methods using the quantum regression theorem. For a large enough dipole coupling constant

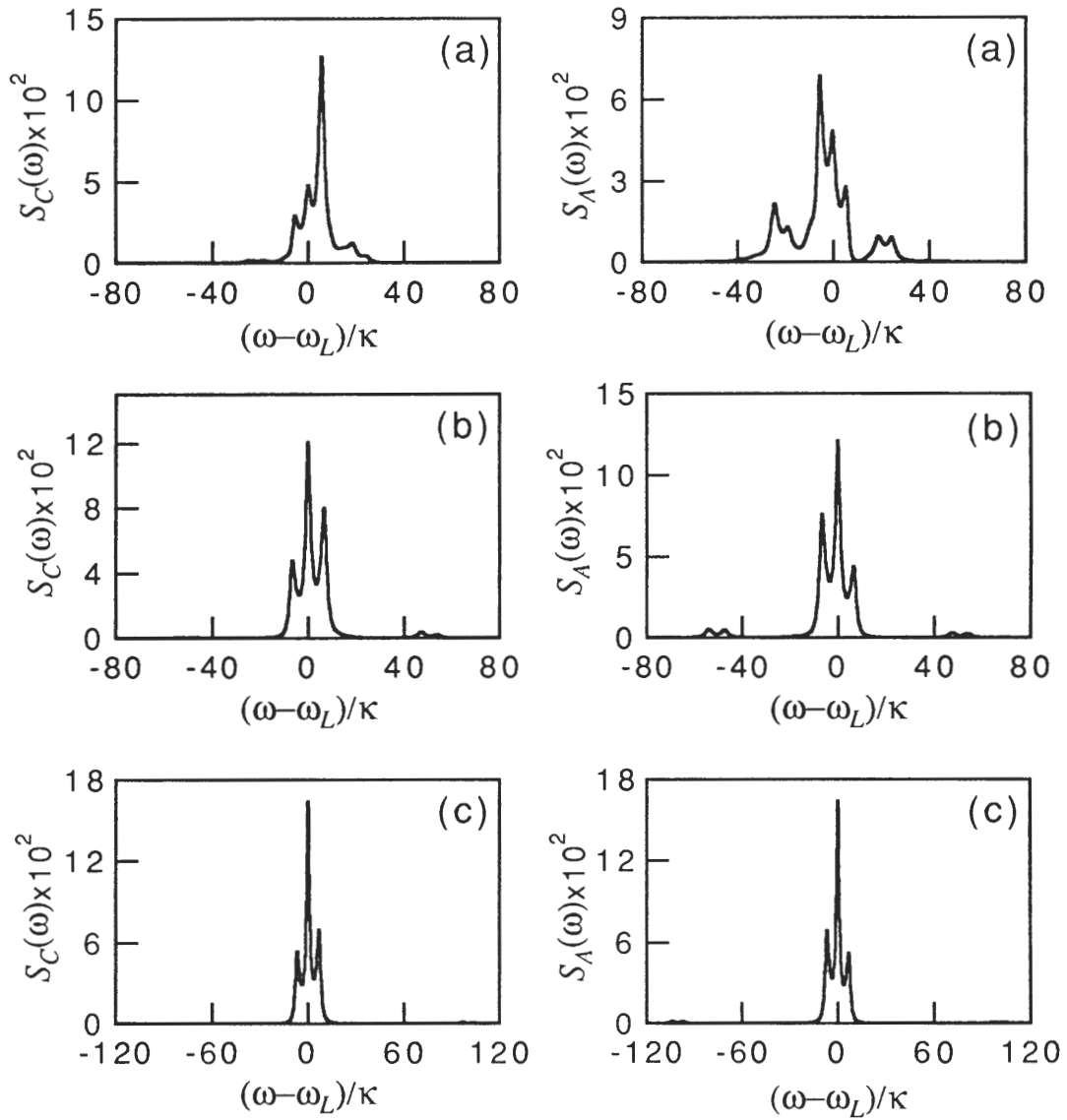


Figure 6.6. Incoherent spectrum of the light transmitted by the cavity, $S_C(\omega)$, and radiated by the atom, $S_A(\omega)$. The plots are for $\gamma/2\kappa = 1$ and $\mathcal{E}/\kappa = 5$: (a) $g/\kappa = 10$, (b) $g/\kappa = 25$, (c) $g/\kappa = 50$. Each spectrum is normalized so that its integral with respect to ω/κ is unity.

the expected Mollow triplet appears with a Rabi splitting $\pm\sqrt{2}\mathcal{E}$, which is what is expected from the model (6.2) for the two-state system. We emphasize that this splitting is not derived from any combination of the energy level separations in the spectrum of the Jaynes-Cummings Hamiltonian for the coupled atom and cavity; it does not depend on g (other than through the requirement of strong dipole coupling). Unlike the “vacuum” Rabi splitting itself, which is a result of the interaction between the atom and the cavity mode, the dynamic Stark splitting of the “vacuum” Rabi resonance is a result of the interaction between the classical driving field and the atom-cavity “molecule.” It provides further clear evidence of the existence of the “molecule” as a single quantum entity.

In the quantitative details our prediction of the same Mollow spectrum for the light transmitted by the cavity and the fluorescence from the atom is not born out in Fig. 6.6. The triplet components in the spectra are asymmetric and there are additional features centered at $\omega - \omega_L = \pm 2g$. These departures from the Mollow spectrum occur because the two-state approximation is really rather inaccurate. They are very large for $g/\kappa = 10$, but become smaller as this ratio is increased. The features at $\omega - \omega_L = \pm 2g$ are due to population in the state $|1, u\rangle$. The asymmetries are due to the near resonance of the $|1, l\rangle \rightarrow |2, l\rangle$ transition; the symmetry is broken by the unequal detuning of $|2, l\rangle$ from the two dressed components of $|1, l\rangle$ and the inequality of the matrix elements $\langle 2, l | \hat{a} | 1, l \rangle$ and $\langle 2, l | \hat{\sigma}_- | 1, l \rangle$.

In the above we have used the traditional method to calculate optical spectra.

In the rest of this section, we will describe a new way to do so – we will use the quantum trajectory theory for cascaded open systems to simulate a measurement of the optical spectrum [61]. In the case here, spectral calculations can be done using either the traditional method or the quantum trajectory method. As we mentioned before, however, for a large system perhaps it is very hard or impossible to use the traditional method to calculate spectra, while the quantum trajectory method may provide an easy way to do this. Let us now see how to simulate a measurement of the optical spectrum using the quantum trajectory theory for cascaded open systems.

We calculate the spectrum of the light transmitted by the cavity by injecting this light into a second, filter cavity, and simulating quantum trajectories for the coupled cavity and atom plus filter cavity. Figure 6.7 illustrates the cascaded open systems. We denote the unnormalized conditioned wavefunction for the cascaded systems (the coupled cavity and atom plus filter cavity) by $|\psi_{c,T}(t)\rangle$. According to the quantum trajectory theory for cascaded open systems, between photon emissions we have the Schrödinger equation (in the interaction picture):

$$|\dot{\psi}_{c,T}\rangle = [\hat{H}/i\hbar - (\gamma/2)\hat{\sigma}_+\hat{\sigma}_- - \kappa_a\hat{a}^\dagger\hat{a} - 2\sqrt{\kappa_a\kappa_b}\hat{a}\hat{b}^\dagger - (\eta + i\bar{\omega})\hat{b}^\dagger\hat{b}]|\bar{\psi}_{c,T}\rangle; \quad (6.8)$$

for the coupled cavity and atom (open system A), \hat{H} satisfies Eq. (6.1), $2\kappa_a$ and γ are the linewidths (full widths at half maximum) of the cavity and the atom, respectively; for the filter cavity (open system B), $2\eta = 2(\kappa_b + \kappa_{b'}) \ll 2\kappa_a$ is the linewidth for the filter cavity, $\bar{\omega} = \omega - \omega_L$ is the detuning of the filter cavity from the driving field for system A , \hat{b}^\dagger and \hat{b} are boson creation and annihilation operators for the filter cavity

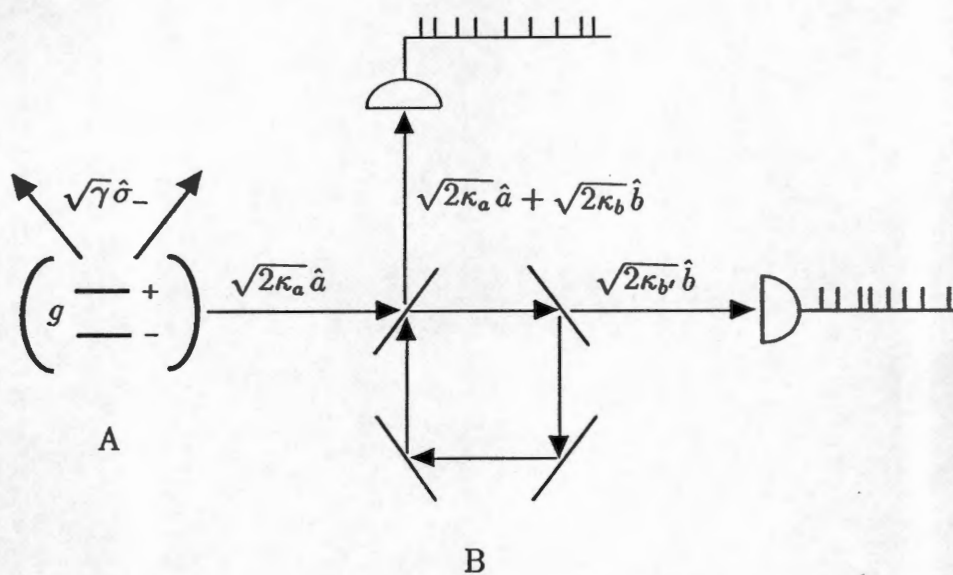


Figure 6.7. Open quantum system B (the filter cavity) cascades with a quantum system A (the coupled cavity and atom).

mode. In Eq. (6.8), the first three terms describe system A alone, the fourth term is the coupling between A and B , the fifth term describes system B alone.

In the limit $\eta \ll \kappa_a$, the unnormalized conditioned state may be written as

$$|\bar{\psi}_{c,T}(t)\rangle = |\bar{\psi}_c(t)\rangle|0\rangle_F + |\bar{\psi}_c^1(t)\rangle|1\rangle_F, \quad (6.9)$$

where $|0\rangle_F$ and $|1\rangle_F$ are the vacuum and the one-photon states of the filter cavity, respectively. Thus, from the equation (6.8), we obtain a pair of equations – Eq. (5.3) with \hat{H} satisfying Eq. (6.1) and the equation

$$|\dot{\bar{\psi}}_c^1\rangle = [\hat{H}/i\hbar - (\gamma/2)\hat{\sigma}_+\hat{\sigma}_- - \kappa_a\hat{a}^\dagger\hat{a} - (\eta + i\bar{\omega})]|\bar{\psi}_c^1\rangle - 2\sqrt{\kappa_a\kappa_b}\hat{a}|\bar{\psi}_c\rangle. \quad (6.10)$$

For $\eta \ll \kappa_a$, we can neglect the photon emission from the filter cavity (open system B). Thus Eqs. (5.4) – (5.7) are still satisfied. From Eqs. (5.3) – (5.7), (6.1) and (6.10), we calculate the spectrum – the time-averaged conditioned mean photon number for the filter cavity $\langle\bar{\psi}_c^1(t)|\bar{\psi}_c^1(t)\rangle/\langle\bar{\psi}_c(t)|\bar{\psi}_c(t)\rangle$, for different settings of the filter frequency ω . Figure 6.8 shows the results of this simulation, which includes a contribution from filtered coherent light (not shown in Fig. 6.6). Again, the numerical simulation shows residual sampling fluctuations, much like experimental data.

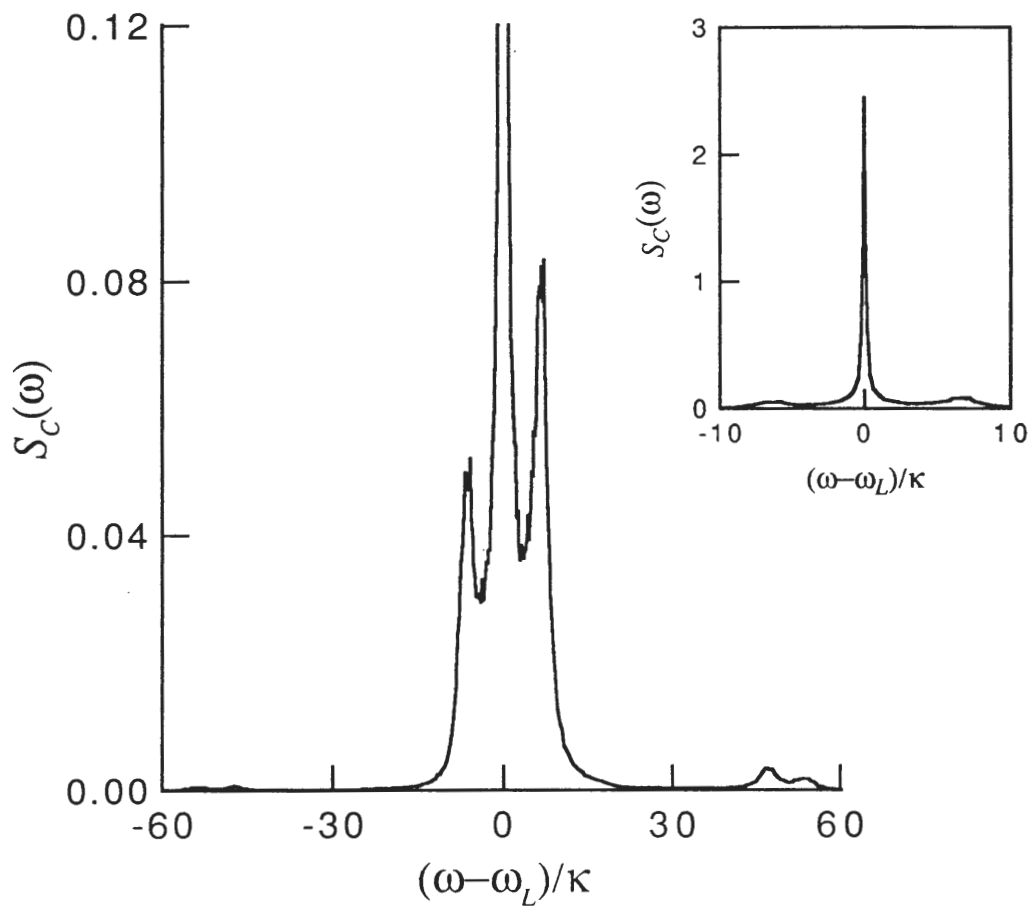


Figure 6.8. Simulated measurement of the spectrum of the light transmitted by the cavity for $\gamma/2\kappa = 1$, $g/\kappa = 25$, and $\mathcal{E}/\kappa = 5$.

CHAPTER VII

SCHRÖDINGER CATS

The previous chapters investigated a single atom strongly coupled to a single quantized mode of the field in a cavity. The quantum nature of this atom-cavity-mode system was demonstrated. In this chapter we apply the atom-cavity “molecule” to a study of Schrödinger cat states. Again, the quantum trajectory method is used. We simulate the generation of Schrödinger cat states using quantum trajectories based on direct detection, and the observation of these states using trajectories based on temporal-mode-matched homodyne detection. The Schrödinger cat states are macroscopic superpositions of coherent states. Here the Schrödinger cats we generated are only few-photon cats. The signature of the Schrödinger cat state is an interference fringe in the marginal distribution measured by homodyne detection. This follows from the fact that the marginal distribution for any quadrature amplitude of the signal field is obtained by integrating the Wigner function, representing the quantum state of the field, over the conjugate variable [62, 63, 64]. We first introduce the Wigner function. We then simulate the generation and homodyne detection of the Schrödinger cat states. We obtain the distribution of measurements using the homodyne detection in a computer “experiment.” This distribution shows the interference fringes that indicate the existence of the Schrödinger cat.

7.1 Wigner Function

The Wigner function $W(\alpha, \alpha^*)$ of the complex amplitude α and its conjugate α^* is defined as [65]

$$W(\alpha, \alpha^*) = (1/\pi^2) \int d^2z C_W(z, z^*) e^{-iz^*\alpha^*} e^{-iz\alpha}, \quad (7.1)$$

where $C_W(z, z^*)$ is a characteristic function

$$\begin{aligned} C_W(z, z^*) &= \text{tr}(\rho e^{iz^*\hat{a}^\dagger + iz\hat{a}}) \\ &= e^{-|z|^2/2} \text{tr}(\rho e^{iz^*\hat{a}^\dagger} e^{iz\hat{a}}). \end{aligned} \quad (7.2)$$

For the pure state $|\psi\rangle$, the density operator can be written as $\rho = |\psi\rangle\langle\psi|$. Thus, we have

$$C_W(z, z^*) = e^{-|z|^2/2} \langle\psi| e^{iz^*\hat{a}^\dagger} e^{iz\hat{a}} |\psi\rangle. \quad (7.3)$$

The real and imaginary parts of α are x and y :

$$x = (1/2)(\alpha + \alpha^*), \quad y = (1/2i)(\alpha - \alpha^*), \quad (7.4)$$

which correspond to two quadrature amplitudes of the field. From Eq. (7.1) we express the Wigner function in terms of x and y (proportional to position and momentum variables, respectively) as

$$W(x, y) = (1/\pi^2) \int_{-\infty}^{\infty} du \int_{-\infty}^{\infty} dv C_W(u + iv, u - iv) e^{-2i(ux - vy)}. \quad (7.5)$$

The Wigner function $W(x, y)$ may be viewed as a quantum mechanical analogue of a probability distribution. It is the quantum mechanical correspondence of the

classical joint probability distribution. The Wigner function $W(x, y)$, for a pair of non-commuting variables x and y , can take negative values in some parts of its range. For this reason it is referred to as a quasiprobability distribution.

Let us now consider a superposition of coherent states:

$$|\psi\rangle = e^{-i\theta}|ib\rangle - e^{i\theta}|-ib\rangle, \quad (7.6)$$

where θ is an arbitrary phase. From equations (7.3) and (7.5) the Wigner function for the state (7.6) is obtained in the form

$$W(x, y) = (1/\pi^3)e^{-2x^2}[e^{-2(y-b)^2} + e^{-2(y+b)^2} - 2e^{-2y^2} \cos 2(2bx - \theta)]. \quad (7.7)$$

Fig. 7.1 shows this distribution. The first two Gaussians on the right-hand side of Eq. (7.7) can be produced by a statistical mixture of two coherent states in Eq. (7.6). They are represented by two bumps in Fig. 7.1. The third term on the right-hand side of Eq. (7.7) is the interference term, associated with the quantum coherence between the two coherent states in Eq. (7.6). It is a Gaussian modulated by a cosine with a frequency of oscillation proportional to the amplitude of the field.

7.2 Generation of Schrödinger Cats

We consider a single three-level atom which is held stationary inside an optical cavity. Such a three-level atom is depicted in Fig. 7.2. We generate a Schrödinger cat — a superposition of coherent states — inside the cavity through two separate stages of duration τ_1 and τ_2 , respectively. In stage 1, the cavity mode, with frequency ω_0 , is

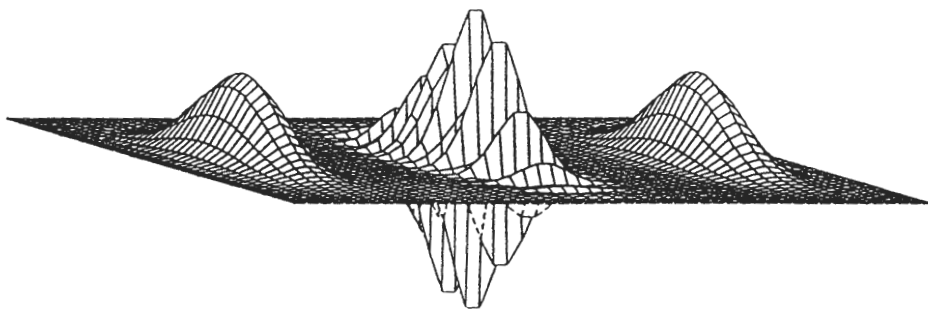


Figure 7.1. Wigner distribution for the superposition of coherent states.

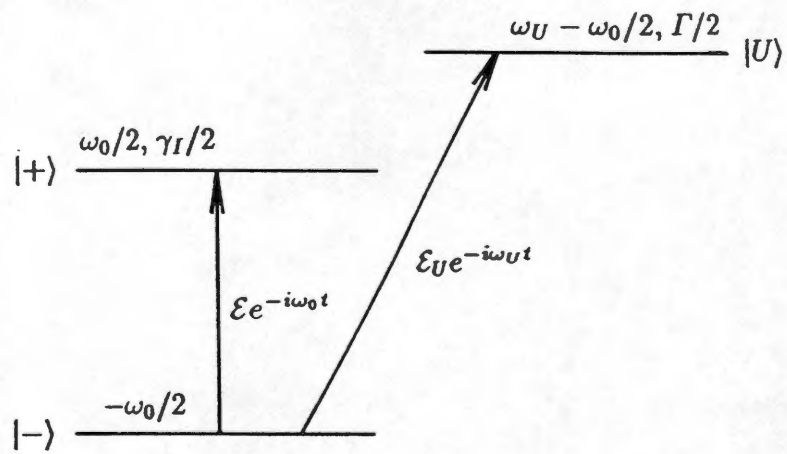


Figure 7.2. Energy levels of the three-level atom used to generate a Schrödinger cat state of the optical field.

coupled on resonance with the $|-\rangle \rightarrow |+\rangle$ transition of the atom which is driven from the side by an external coherent field. This generates a coherent state superposition in the cavity, entangled with the dressed states of the atom. At the end of stage 1 the coherent field is turned off and the atom is d. c. Stark shifted out of resonance with the cavity. Stage 2 untangles the coherent state superposition from the dressed states of the atom. This is achieved by coherently driving the $|-\rangle \rightarrow |U\rangle$ transition and detecting a photon in fluorescence. The detection of fluorescence is necessary to set the phase of the Schrödinger cat and if no fluorescence is detected the trajectory is abandoned.

Let us now simulate the evolution of the conditioned wavefunction for the coupled system of the atom and cavity mode. The evolution is governed by the following equations: For $0 < t \leq \tau_1$ (stage 1) the quantum trajectory is based on direct photoelectric detection. The Schrödinger equation between photon emissions is

$$|\dot{\bar{\psi}}_c\rangle = (1/i\hbar)\hat{H}_1(t)|\bar{\psi}_c\rangle, \quad (7.8)$$

with

$$\hat{H}_1(t) = \hat{H}_{free} + i\hbar g(\hat{\sigma}_-\hat{a}^\dagger - \hat{\sigma}_+\hat{a}) + i\hbar\mathcal{E}(\hat{\sigma}_-e^{i\omega_0 t} - \hat{\sigma}_+e^{-i\omega_0 t}). \quad (7.9)$$

The free Hamiltonian is a non-Hermitian operator:

$$\begin{aligned} \hat{H}_{free} &= \hbar(\omega_0 - i\kappa)\hat{a}^\dagger\hat{a} - \hbar(\omega_0/2)\hat{\sigma}_-\hat{\sigma}_+ + \hbar(\omega_0/2 - i\gamma/2)\hat{\sigma}_+\hat{\sigma}_- \\ &\quad + \hbar(\omega_U - \omega_0/2 - i\Gamma/2)\hat{\Sigma}_+\hat{\Sigma}_-, \end{aligned} \quad (7.10)$$

where $\hat{\Sigma}_- = |-\rangle\langle U|$ and $\hat{\Sigma}_+ = |U\rangle\langle -|$. Photon emissions occur randomly at the rates

given by Eqs. (5.4) and (5.6) (The state $|U\rangle$ cannot be reached during stage 1 and there are no photon emissions from this state.).

In order to see how stage 1 generates a coherent state superposition entangled with the atom we first solve Eq. (7.8) analytically in the limit $g/\mathcal{E} \rightarrow 0$. Here we assume that τ_1 is so short (compared to the cavity and atom lifetimes) that it is unlikely that a photon emission will occur. Thus by solving only Eq. (7.8) we obtain the conditioned wavefunction at time τ_1 . In the interaction picture, Hamiltonian \hat{H}_1 can be written as

$$\hat{H}_1(t) = i\hbar g(\hat{\sigma}_- \hat{a}^\dagger - \hat{\sigma}_+ \hat{a}) + i\hbar \mathcal{E}(\hat{\sigma}_- - \hat{\sigma}_+), \quad (7.11)$$

where we have assumed that there are no emissions for stage 1. We define the dressed states of the atom by

$$\begin{aligned} |u\rangle &= (1/\sqrt{2})(|+\rangle + i|-\rangle), \\ |l\rangle &= (1/\sqrt{2})(|+\rangle - i|-\rangle), \end{aligned} \quad (7.12)$$

where $|+\rangle$ and $|-\rangle$ are the upper and lower atomic states. The dressed states are eigenstates of $i\hbar \mathcal{E}(\hat{\sigma}_- - \hat{\sigma}_+)$. We then write

$$\begin{aligned} \hat{\sigma}_- &= (-i/2)(\hat{d}_z + \hat{d}_u - \hat{d}_l), \\ \hat{\sigma}_+ &= (i/2)(\hat{d}_z + \hat{d}_l - \hat{d}_u), \end{aligned} \quad (7.13)$$

where

$$\begin{aligned} \hat{d}_u &= |u\rangle\langle l|, & \hat{d}_l &= |l\rangle\langle u|, \\ \hat{d}_z &= |u\rangle\langle u| - |l\rangle\langle l|. \end{aligned} \quad (7.14)$$

Substituting from Eqs. (7.13) into Eq. (7.11):

$$\hat{H}_1(t) = \hbar\mathcal{E}\hat{d}_z + (\hbar g/2)\hat{d}_z(\hat{a}^\dagger + \hat{a}) + (\hbar g/2)(\hat{d}_u - \hat{d}_l)(\hat{a}^\dagger - \hat{a}). \quad (7.15)$$

We expand the conditioned state as

$$|\bar{\psi}_c\rangle = |\bar{\psi}_u\rangle|u\rangle + |\bar{\psi}_l\rangle|l\rangle, \quad (7.16)$$

then from Eqs. (7.8) and (7.15) we obtain

$$\begin{aligned} |\dot{\bar{\psi}}_u\rangle &= [-i\mathcal{E} - i(g/2)(\hat{a}^\dagger + \hat{a})]|\bar{\psi}_u\rangle - i(g/2)(\hat{a}^\dagger - \hat{a})|\bar{\psi}_l\rangle, \\ |\dot{\bar{\psi}}_l\rangle &= [i\mathcal{E} + i(g/2)(\hat{a}^\dagger + \hat{a})]|\bar{\psi}_l\rangle + i(g/2)(\hat{a}^\dagger - \hat{a})|\bar{\psi}_u\rangle. \end{aligned} \quad (7.17)$$

We make the transformation

$$|\bar{\psi}_u\rangle = e^{-i\mathcal{E}t}|\tilde{\psi}_u\rangle, \quad |\bar{\psi}_l\rangle = e^{i\mathcal{E}t}|\tilde{\psi}_l\rangle, \quad (7.18)$$

and have

$$\begin{aligned} |\dot{\tilde{\psi}}_u\rangle &= -i(g/2)(\hat{a}^\dagger + \hat{a})|\tilde{\psi}_u\rangle - i(g/2)e^{2i\mathcal{E}t}(\hat{a}^\dagger - \hat{a})|\tilde{\psi}_l\rangle, \\ |\dot{\tilde{\psi}}_l\rangle &= i(g/2)(\hat{a}^\dagger + \hat{a})|\tilde{\psi}_l\rangle + i(g/2)e^{-2i\mathcal{E}t}(\hat{a}^\dagger - \hat{a})|\tilde{\psi}_u\rangle. \end{aligned} \quad (7.19)$$

In the limit $g/\mathcal{E} \rightarrow 0$, we drop the oscillatory terms in Eqs. (7.19) using the secular approximation, and then have

$$\begin{aligned} |\dot{\tilde{\psi}}_u\rangle &= -i(g/2)(\hat{a}^\dagger + \hat{a})|\tilde{\psi}_u\rangle, \\ |\dot{\tilde{\psi}}_l\rangle &= i(g/2)(\hat{a}^\dagger + \hat{a})|\tilde{\psi}_l\rangle. \end{aligned} \quad (7.20)$$

The solutions to Eqs. (7.20) may be written as

$$|\tilde{\psi}_u(t)\rangle = e^{-i(g/2)(\hat{a}^\dagger + \hat{a})t}|\tilde{\psi}_u(0)\rangle, \quad |\tilde{\psi}_l(t)\rangle = e^{i(g/2)(\hat{a}^\dagger + \hat{a})t}|\tilde{\psi}_l(0)\rangle. \quad (7.21)$$

For the initial state $|\bar{\psi}_c(0)\rangle = |-\rangle|0\rangle$, we have

$$|\tilde{\psi}_u(0)\rangle = (-i/\sqrt{2})|0\rangle, \quad |\tilde{\psi}_l(0)\rangle = (i/\sqrt{2})|0\rangle, \quad (7.22)$$

where $|0\rangle$ is the vacuum state. Both operators $e^{-i(g/2)(\hat{a}^\dagger + \hat{a})t}$ and $e^{i(g/2)(\hat{a}^\dagger + \hat{a})t}$ in Eqs. (7.21) are called the coherent state displacement operators [66]. When they act on the vacuum state they perform displacements of the vacuum state to the coherent states $| -igt/2\rangle$ and $|igt/2\rangle$, respectively. Thus, we have

$$|\hat{\psi}_u(t)\rangle = (-i/\sqrt{2})| -igt/2\rangle, \quad |\hat{\psi}_l(t)\rangle = (i/\sqrt{2})|igt/2\rangle, \quad (7.23)$$

The conditioned wavefunction at time τ_1 is obtained (in the interaction picture):

$$|\psi_c(\tau_1)\rangle = (-i/\sqrt{2})(e^{-i\mathcal{E}\tau_1}|u\rangle| -igt_1/2\rangle - e^{i\mathcal{E}\tau_1}|l\rangle|igt_1/2\rangle), \quad (7.24)$$

We transform Eq. (7.24) to the Schrödinger picture and have

$$|\psi_c(\tau_1)\rangle = (-i/\sqrt{2})(e^{-i\mathcal{E}\tau_1}|u_s\rangle| -igt_1/2\rangle - e^{i\mathcal{E}\tau_1}|l_s\rangle|igt_1/2\rangle), \quad (7.25)$$

where

$$\begin{aligned} |u_s\rangle &= (1/\sqrt{2})(e^{-i(\omega_0/2)\tau_1}|+\rangle + ie^{i(\omega_0/2)\tau_1}|-\rangle), \\ |l_s\rangle &= (1/\sqrt{2})(e^{-i(\omega_0/2)\tau_1}|+\rangle - ie^{i(\omega_0/2)\tau_1}|-\rangle). \end{aligned} \quad (7.26)$$

Equation (7.25) describes a coherent state superposition in the cavity, entangled with the dressed states of the atom.

For $\tau_1 < t \leq \tau_1 + \tau_2$ (stage 2) the quantum trajectory is still based on direct photoelectric detection, but the interaction Hamiltonian is changed. The Schrödinger

equation between photon emissions is now

$$|\dot{\bar{\psi}}_c\rangle = (1/i\hbar)\hat{H}_2(t)|\bar{\psi}_c\rangle, \quad (7.27)$$

where

$$\hat{H}_2(t) = \hat{H}_{free} + i\hbar\mathcal{E}_U(\Sigma_- e^{i\omega_U t} - \Sigma_+ e^{-i\omega_U t}). \quad (7.28)$$

(We note that the $|-\rangle \rightarrow |+\rangle$ resonance frequency in \hat{H}_{free} has been changed by the d. c. Stark shift.) If $\Gamma \gg \gamma, 2\kappa$ the dominant rate for photon emissions is $r_U(t) = \Gamma\langle\psi_c(t)|\hat{\Sigma}_+\hat{\Sigma}_-|\psi_c(t)\rangle$ which governs the fluorescence on the $|-\rangle \rightarrow |U\rangle$ transition of the atom. The first emitted photon sets the time $\tau_1 + \tau_2$. At this time the entangled state (7.25) is changed by the collapse $|\bar{\psi}_c(t)\rangle \rightarrow \hat{\Sigma}_-|\bar{\psi}_c(t)\rangle$ into the product state

$$\begin{aligned} |\psi_c(\tau_1 + \tau_2)\rangle &= (1/\sqrt{2})(e^{-i\mathcal{E}\tau_1}|-ig\tau_1/2\rangle + e^{i\mathcal{E}\tau_1}|ig\tau_1/2\rangle) \\ &\quad (e^{i(\omega_0/2)(\tau_1+\tau_2)}e^{i\omega_U\tau_2}|-\rangle), \end{aligned} \quad (7.29)$$

where we have used $\Gamma \gg \mathcal{E}_U$ and dropped some small terms. Equation (7.29) describes a coherent state superposition inside the cavity. A Schrödinger cat is now generated.

7.3 Observation of Schrödinger Cat

In the last section we have generated a Schrödinger cat, a coherent state superposition in the cavity. Let us now see how to observe the cat. Figure 7.3 illustrates the detection scheme we will use. The field inside the cavity is allowed to freely decay, and the cavity output is combined with a strong local oscillator whose amplitude is decaying at the same rate. The phase of the local oscillator is set to $\theta = 0$ so

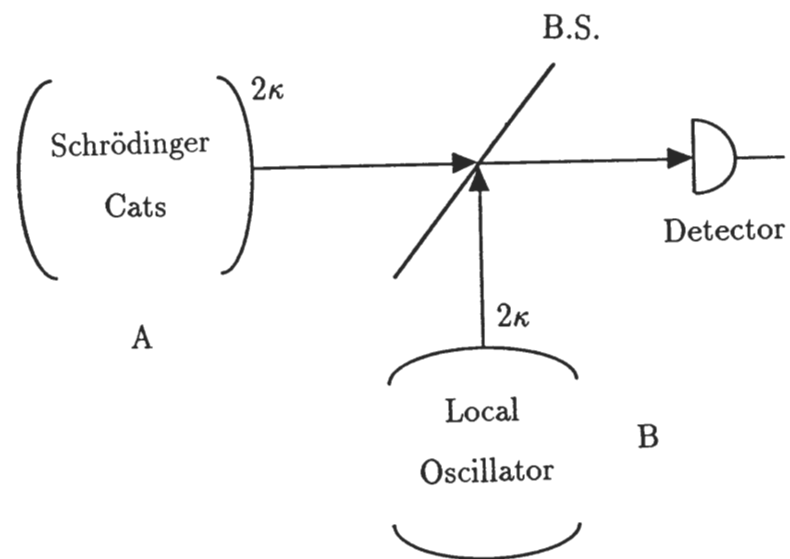


Figure 7.3. Model of the Schrödinger cat inside the cavity A seen by the detector in homodyne detection. The cavity B radiates a coherent local oscillator field.

we observe the interference fringe which is in quadrature to the displacement of the coherent states. We integrate the photocurrent to obtain one measured quantity for each trajectory. Over an ensemble of trajectories the distribution of measurements shows the interference pattern that reveals the existence of the Schrödinger cat.

Now the quantum trajectory is based on homodyne detection. Notice that all of the quantum trajectories we have constructed so far are based on ideal detection, the conversion of photons to photoelectrons with unit efficiency. In the present case we need to consider the factor of nonunit efficiency. We generalize Eqs. (5.17) – (5.19) to detection with efficiency $\eta \leq 1$. We model the cavity with two transmitted mirrors rather than one for unit efficiency. Then the photon loss rates for the cavity through the two mirrors are $2\kappa\eta$ and $2\kappa(1-\eta)$, respectively. By modeling homodyne detection, we arrive at the stochastic Schrödinger equation

$$|\dot{\bar{\psi}}_c\rangle = (1/i\hbar) \left\{ \hat{H}_O(t) + i\hbar \left[\sqrt{\eta} \xi_\eta(t) + \sqrt{1-\eta} \xi_{1-\eta}(t) \right] e^{i(\omega_0 t - \phi)} \sqrt{2\kappa} \hat{a} \right\} |\bar{\psi}_c\rangle, \quad (7.30)$$

with $\hat{H}_O = \hat{H}_{free}$ and

$$\begin{aligned} \xi_\eta(t) &= \sqrt{\eta} \sqrt{2\kappa} \langle \psi_c(t) | (e^{-i(\omega_0 t - \phi)} \hat{a}^\dagger + e^{i(\omega_0 t - \phi)} \hat{a}) | \psi_c(t) \rangle + \mu_\eta(t), \\ \xi_{1-\eta}(t) &= \sqrt{1-\eta} \sqrt{2\kappa} \langle \psi_c(t) | (e^{-i(\omega_0 t - \phi)} \hat{a}^\dagger + e^{i(\omega_0 t - \phi)} \hat{a}) | \psi_c(t) \rangle + \mu_{1-\eta}(t). \end{aligned} \quad (7.31)$$

$\mu_\eta(t)$ and $\mu_{1-\eta}(t)$ are independent Gaussian white noise sources. Eqs. (5.17) and (5.18) can be obtained from Eqs. (7.30) and (7.31) for $\eta = 1$. Now the quantity $\xi_\eta(t)$ is related to the homodyne photocurrent $I_\eta(t)$ for efficiency η , with

$$I_\eta(t) = Ge \left[\eta f e^{-2\kappa t} + \sqrt{\eta} f e^{-\kappa t} \xi_\eta(t) \right], \quad (7.32)$$

Note that Eq. (7.32) is obtained from Eq. (5.19) after the local oscillator photon flux f is replaced by $\eta f e^{-2\kappa t}$; thus, we assume that the local oscillator leaks out of a cavity identical to the one in which the Schrödinger cat is prepared. We integrate the photocurrent noise to obtain

$$X_\eta = \int_{\tau_1+\tau_2}^{\tau_1+\tau_2+\tau_O} dt \frac{I_\eta(t) - Ge\eta f e^{-2\kappa t}}{Ge\sqrt{\eta f}} = \int_{\tau_1+\tau_2}^{\tau_1+\tau_2+\tau_O} dt e^{-\kappa t} \xi_\eta(t), \quad (7.33)$$

where τ_O is the duration for the Schrödinger cat to be observed.

For each trajectory we obtain one number of X_η . Over an ensemble of trajectories we build up the distribution of the quantity X_η . This distribution is related to a marginal distribution of the Wigner function representing the state of the cavity mode before it begins to decay. It has been shown that for unit detection efficiency the distribution of X_η is proportional to the marginal distribution obtained by integrating (7.7) over y [67]. Thus the interference pattern appearing in the distribution of X_η reveals the existence of the Schrödinger cat.

It is straightforward to calculate the marginal distribution of the Wigner function representing the state of the cavity mode in (7.29). This Wigner function can be obtained from Eq. (7.7) by replacing $b = -g\tau_1/2$ and $\theta = \mathcal{E}\tau_1$. The interference term in Eq. (7.7) indicates the quantum superposition of the state we generated inside the cavity. The marginal distribution $W(x)$ is then obtained

$$W(x) = \int_{-\infty}^{\infty} dy W(x, y) = \sqrt{2/\pi^5} e^{-2x^2} [1 - \cos 2(2bx - \theta)]. \quad (7.34)$$

Figure 7.4 shows the distribution represented by Eq. (7.34) for $b = 5$ and $\theta = 1.7\pi$. The marginal distribution gives us some idea about what the distribution of X_η should

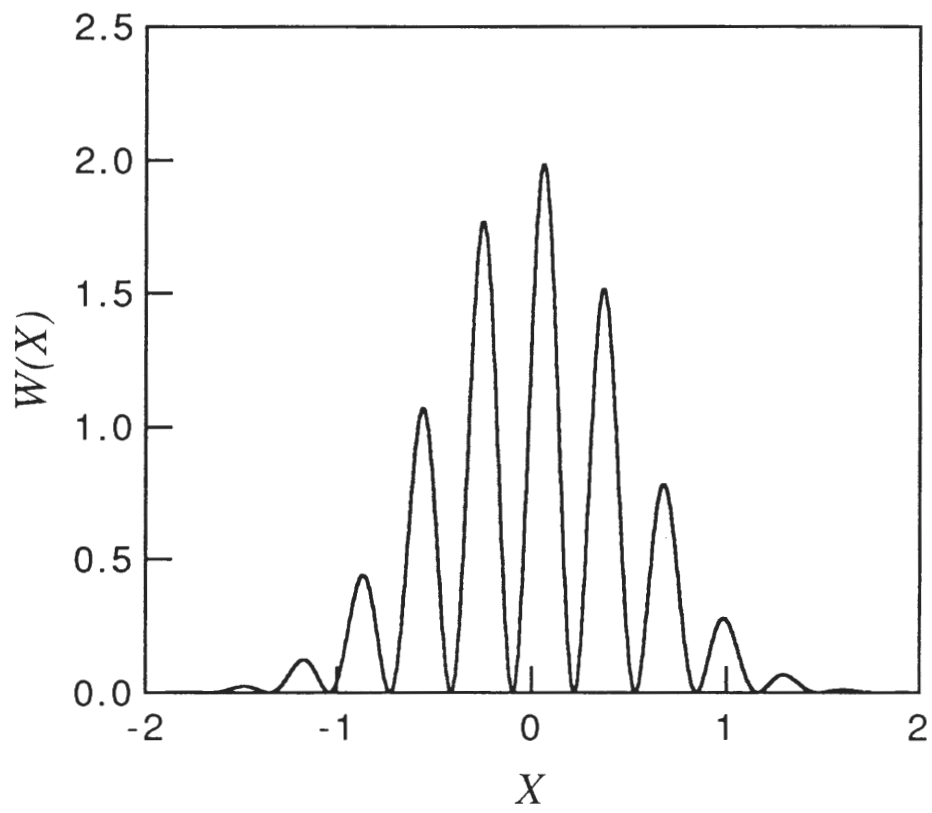


Figure 7.4. Marginal distribution obtained from Eq. (7.34) for $b = 5$, and $\theta = 1.7\pi$.

look like. We then expect to see the interference pattern in the distribution of X_η . Let us now see the results of numerical simulations for this distribution.

Figure 7.5 and 7.6 show results for the distribution of X_η obtained from an ensemble of 10^5 trajectories generated from Eqs. (7.8) – (7.10), (7.27) – (7.28), and (7.30) – (7.33). The quantity $N_\eta(X_\eta)$ is the number of trajectories giving a result for the integrated photocurrent in the range X_η to $X_\eta + 0.01$. In Fig. 7.5 the detection efficiency is 95%. Two sets of results are shown: distributions (a), (b), and (c) are for a ~ 2 -photon Schrödinger cat; (d), (e), and (f) are for a ~ 6 -photon Schrödinger cat. Figs. 7.5(a) and 7.5(d) include the effects of photon loss during the preparation of the Schrödinger cat. For the chosen parameters the loss virtually destroys the interference. The negative effects of loss during the preparation stage can easily be understood. A single photon emission causes the conditioned wavefunction to collapse according to Eqs. (5.5) and (5.7). If the photon is emitted through the cavity mirrors, the operator \hat{a} is applied to $|\psi_c(t)\rangle$ at some time during the generation of the state (7.29). This changes the phase of the coherent state superposition by π (shifted the fringe in Fig. 7.4 by π). Thus, if half the trajectories suffer just one photon loss from the cavity, the interferences for the phase-shifted and unshifted cats will cancel in the ensemble average.

A photon lost in fluorescence has a similar effect; although, for a saturated atom the rate governing this loss does not increase with photon number. The collapse in this case projects the atom to its ground state. It is most likely to occur when the

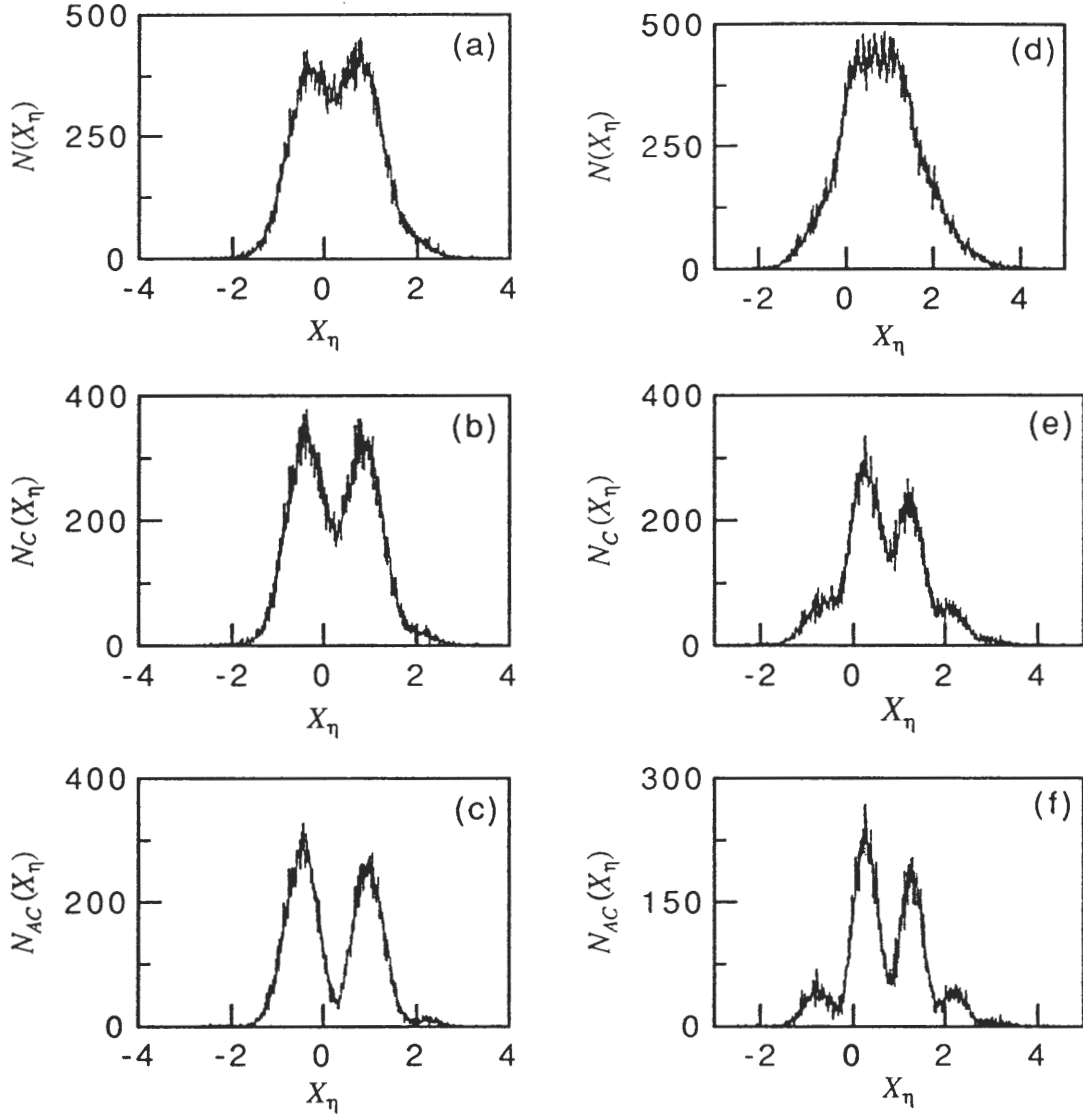


Figure 7.5. Two sets of distributions of the integrated photocurrent for an ensemble of quantum trajectories generated by Eqs.(7.8)-(7.10), (7.26)-(7.27), and (7.29)-(7.32) for different values of intracavity photon numbers: $\gamma/2\kappa = 1.5$, $\kappa\tau_1 = 0.19$, $\kappa\tau_0 = 3$, $\eta = 0.95$, and $g/\kappa = 15$, $\mathcal{E}/\kappa = 60$ [(a), (b), (c)]; $g/\kappa = 25$, $\mathcal{E}/\kappa = 100$ [(d), (e), (f)]. (a) and (d) include all trajectories; (b) and (e) exclude trajectories which suffered a photon loss through the cavity mirrors during the preparation time τ_1 ; (c) and (f) exclude trajectories which suffered a photon loss either through the cavity mirrors or by atomic fluorescence during the preparation time.

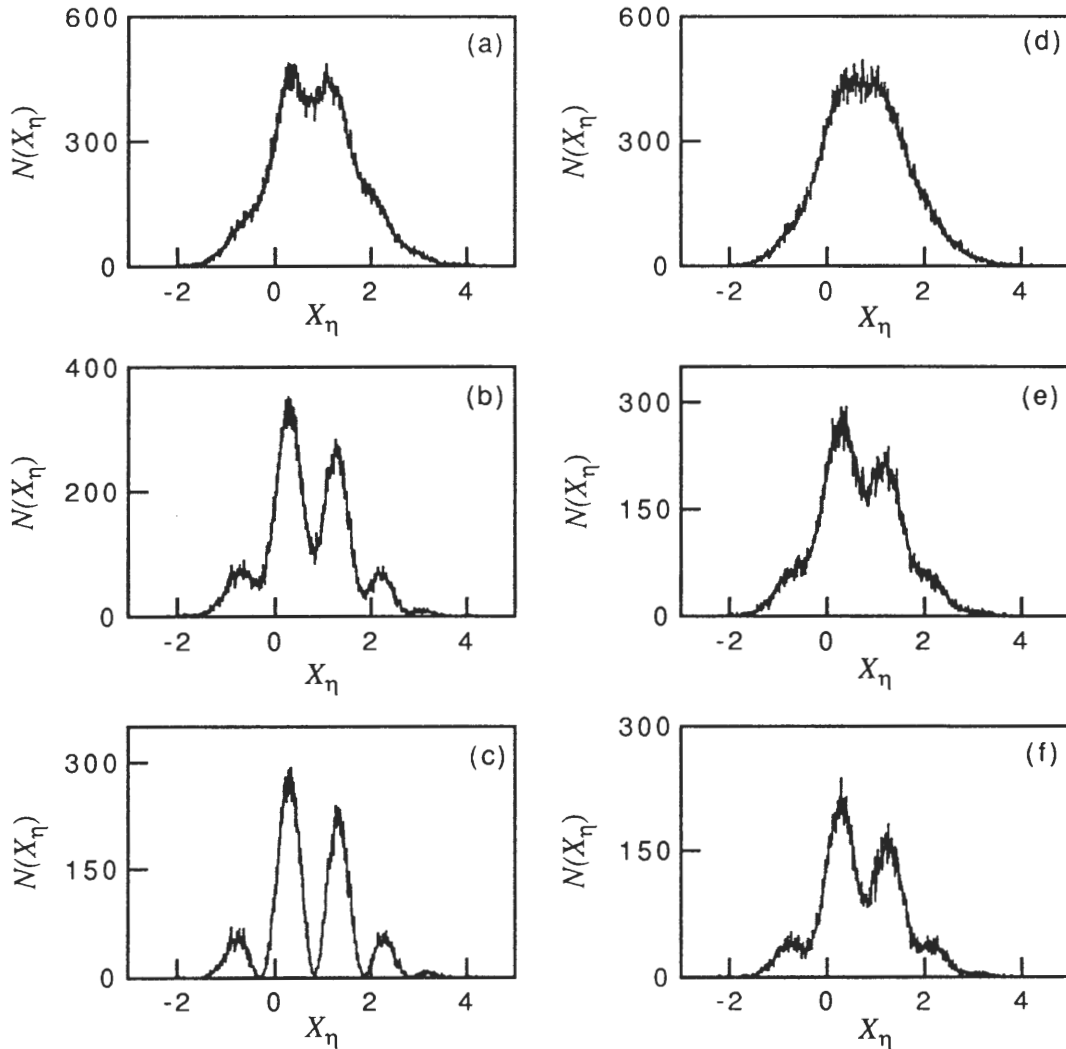


Figure 7.6. Two sets of distributions of the integrated photocurrent for an ensemble of quantum trajectories generated by Eqs.(7.8)-(7.10), (7.26)-(7.27), and (7.29)-(7.32) for different values of detection efficiencies: $\gamma/2\kappa = 1.5$, $\kappa\tau_1 = 0.19$, $\kappa\tau_0 = 3$, $g/\kappa = 25$, $\mathcal{E}/\kappa = 100$, and $\eta = 1.0$ [(a), (b), (c)]; $\eta = 0.9$ [(d), (e), (f)]. (a) and (d) include all trajectories; (b) and (e) exclude trajectories which suffered a photon loss through the cavity mirrors during the preparation time τ_1 ; (c) and (f) exclude trajectories which suffered a photon loss either through the cavity mirrors or by atomic fluorescence during the preparation time.

atom is excited, and the excited to ground state collapse introduces a π phase shift in the Rabi oscillation of the atom. Again, if half the trajectories suffer a loss like this the quantum interference is washed out.

In a computer experiment it is possible to eliminate the negative effects of loss by removing from the ensemble all those trajectories which suffer a photon loss during the preparation time τ_1 . Figs. 7.5(b) and 7.5(e) eliminate the effects of loss through the cavity mirrors; Figs. 7.5(c) and 7.5(f) eliminate the effects of loss both through the cavity mirrors and out the sides of the cavity. In principle the same thing can be done in the laboratory at the expense of a reduced data collection rate. Of course, in practice, for technical reasons it is impossible to detect every lost photon. However, if a significant percentage are detected, in particular, of the photons lost through the cavity mirrors, then the visibility of the quantum interference fringe will be greatly improved. The message in this is that Schrödinger cats may be seen so long as observations are made at the level of the very last quantum. Lost photons are no problem; but we must know that they are lost.

In Fig. 7.6 we compare the two sets of distributions of X_η for the detection efficiency of 100% and 90%. They clearly show that the appearance of quantum interference is extraordinarily sensitive to the detection efficiency. This, again, emphasizes that the basic message is that every photon radiated by the coupled system of the atom and cavity mode must be observed.

CHAPTER VIII

SUMMARY AND CONCLUSIONS

We have studied the interaction of a single two-state atom with a single quantized mode of the electromagnetic field in an optical cavity. Our interest has been in strong coupling conditions where the dipole coupling between the atom and the cavity mode splits the first excited state of the Jaynes-Cummings Hamiltonian by an amount that is larger than its width. Under these conditions, we have found that the coupled system of the atom and the cavity mode is not just a single atom in an optical cavity. It is a new composite structure, an atom-cavity “molecule.” We have explored quantum effects in the excited-state spectroscopy of the “molecule.” We have demonstrated two-state behavior in the “molecule,” and we have used the “molecule” to explore the generation and detection of Schrödinger cats. In both of these studies the quantum trajectory formulation was used. While many of our results concern effects that are too subtle to be seen in current experiments, we hope they will be observed in a new generation of experiments. One avenue that may realize the required conditions at optical frequencies involves the replacement of thermal atomic beams with cooled or trapped atoms (ions).

In chapters II – IV we explored the spectroscopy of the coupled system of the atom and cavity mode driven by an external field. We presented three ways to observe the excited-state spectra for the coupled system driven either by coherent light or by

broadband chaotic light. All of the spectra calculated from the QED theory show peaks produced by transitions between the excited states of the Jaynes-Cummings Hamiltonian. These peaks are a clear signature of the quantum Hamiltonian governing the interaction between the atom and the cavity mode, and provide direct evidence of the composite structure of the coupled atom and cavity mode like a “molecule.” On the other hand, the “vacuum” Rabi peaks, taken on their own, are consistent with a classical, coupled harmonic oscillator interpretation of the interaction.

Chapter II discussed the first way to observe the excited-state transitions. This is to use coherent excitation and to observe transmission spectra. The transmission spectra calculated from semiclassical and QED theories were presented. In the limit of very weak fields, both calculations produce the same “vacuum” Rabi spectra. But as the strength of the field is increased, it was seen that the semiclassical and QED calculations exhibit completely different behaviors. The spectra calculated from the semiclassical theory develop bistability on the “vacuum” Rabi peaks. The spectra calculated from the QED theory develop a series of additional resonances in between the “vacuum” Rabi peaks. These resonances have been explained in terms of multi-photon absorption. The positions of these resonances were calculated from the excited-state energies of the Jaynes-Cummings Hamiltonian; they were determined by the level structure of the atom-cavity “molecule.” These resonances show a clear signature of the underlying quantized energy level structure of the coupled atom and cavity mode.

The second way to observe excited-state transitions is to measure modulation spectra for the coupled atom and cavity mode driven by coherent light. In chapter III we first analyzed a modulation spectroscopy scheme designed to reveal the first-to-second excited-state transition. We then performed both QED and semiclassical calculations of the modulation spectra and compared the results of these calculations. As the strength of the pump field is increased, the features that distinguish the QED calculation from the semiclassical calculation were identified and explained. The QED calculation, again, shows the quantum nature of the coupled atom and cavity mode. The parameters we used in these calculations are very close to those realized in current experiments. We expect that the results we obtained here may be observed very soon.

Under extremely strong coupling conditions ($g \gg \gamma, 2\kappa$) we were able to perform analytical calculations by using the secular approximation. For very weak fields we calculated the modulation spectra analytically from both the QED and semiclassical theories. The analytical results supported the earlier numerical results and help us to understand the physics.

The third way to observe excited-state transitions is to use incoherent excitation. This was discussed in chapter IV. We calculated spectra for a coupled atom and cavity mode driven by broadband chaotic light. We calculated three kinds of spectra: the spectrum of the dipole scattering from the atom, the spectrum of the light transmitted by the cavity, and the spectrum of the light reflected by the cavity. All of the spectra

show peaks (or absorption dips) at the incommensurate frequencies corresponding to transitions between the excited states of the Jaynes-Cummings Hamiltonian. These peaks provide a clear signature of the quantum character of the new system formed by a coupled atom and cavity mode.

Extremely strong coupling conditions provide some justification for using the secular approximation. We therefore first obtained analytical results for the spectra in the secular approximation. The linewidths and transition amplitudes obtained in this approximation suggested that the most prominent departures from the two-peaked “vacuum” Rabi spectrum would appear in between the “vacuum” Rabi peaks in the spectrum of the light transmitted by the cavity. This was so for the spectra plotted from our analytical results. But for realistic dipole coupling strengths the accuracy of the secular approximation is in doubt. We therefore also calculated spectra numerically without using the secular approximation. These calculations supported our earlier conclusions, and fortunately increased, rather than decreased, the size of the spectral features associated with excited state transitions.

The quantum trajectory theory was reviewed in chapter V. It is a formulation of open quantum system dynamics in terms of stochastic wavefunctions. The wavefunctions acquire physical meaning as the conditioned wavefunctions of a system whose output channels are monitored by ideal detectors; they are wavefunctions for the system, conditioned on a particular history of signals seen at the detectors. The method brings ideas from quantum measurement theory together with the open-system theory

(master equations) and photoelectric detection theory familiar to people in quantum optics. Systems in cavity quantum electrodynamics are ideally suited to solution by the quantum trajectory method. We therefore presented quantum trajectory formulations based on direct photoelectric detection and on homodyne detection for the cavity QED system. Two standard examples were used to illustrate the theory. While it is the ensemble average over trajectories that reproduces the usual quantum-mechanical average, it was seen that even a single trajectory may show some features about the source system. Thus the quantum trajectory approach clarifies the physical interpretation. On the other hand, this approach also provides new computational tools.

In chapter VI we demonstrated two-state behavior for an optical cavity containing one atom. Here we considered direct excitation of the atom-cavity “molecule” resonance — we tuned a coherent field to one of the “vacuum” Rabi resonances of the coupled atom and cavity mode. We observed that for sufficiently strong dipole coupling the “vacuum” Rabi resonances behave as approximate *two-state* resonances of an atom-cavity “molecule.” We have shown that the atom-cavity “molecule” saturates like a two-state system. We have also demonstrated two-state behavior in simulated measurements of the photoelectron waiting-time distribution, the photoelectron counting distribution, and the optical spectrum; the atom-cavity “molecule” transmits the antibunched and sub-Poissonian light of resonance fluorescence, and shows the triplet spectrum produced by the dynamic Stark effect. We used the quantum

trajectory approach in these simulations, and, in particular, developed a quantum trajectory formulation for simulating the measurement of the optical spectrum.

The final chapter, chapter VII, explored the generation and detection of optical Schrödinger cats (few-photon cats). The quantum trajectory approach was used again here. We generated the Schrödinger cats inside an optical cavity using the coupled system of the atom and cavity mode. The Schrödinger cat states (superpositions of coherent states) are radiated into the cavity by the atom which is driven coherently. The quantum interference of the Schrödinger cats were observed by homodyning the freely decaying field radiated by the cavity using a local oscillator of fixed phase and matched exponential decay. Quantum trajectories enable us to understand how photon loss destroys the quantum interference. With this understanding we have shown that, in principle, the negative effects of loss (other than those due to finite detection efficiency) can be avoided by adding a “spontaneous emission veto” while preparing the Schrödinger cat.

BIBLIOGRAPHY

- [1] E. M. Purcell, *Phys. Rev.* **69**, 681 (1946).
- [2] K. H. Drexhage, *Jour. of Lumin.* **1**, 693 (1970).
- [3] P. Goy, J. M. Raimond, M. Gross, and S. Haroche, *Phys. Rev. Lett.* **50**, 1903 (1983).
- [4] Y. Kaluzny, P. Goy, M. Gross, J. M. Raimond, and S. Haroche, *Phys. Rev. Lett.* **51**, 1175 (1983).
- [5] W. Jhe, A. Anderson, E. A. Hinds, D. Meschede, L. Moi, and S. Haroche, *Phys. Rev. Lett.* **58**, 666 (1987).
- [6] D. J. Heinzen, J. J. Childs, J. E. Thomas, and M. S. Feld, *Phys. Rev. Lett.* **58**, 1320 (1987).
- [7] D. J. Heinzen, and M. S. Feld, *Phys. Rev. Lett.* **59**, 2623 (1987).
- [8] D. Meschede, H. Walther, and G. Muller, *Phys. Rev. Lett.* **54**, 551 (1985).
- [9] G. Rempe, H. Walther, and N. Klein, *Phys. Rev. Lett.* **58**, 353 (1987).
- [10] G. Rempe, F. Schmidt-Kaler, and H. Walther, *Phys. Rev. Lett.* **64**, 2783 (1990).
- [11] G. Rempe, R. J. Thompson, R. J. Brecha, W. D. Lee, and H. J. Kimble, *Phys. Rev. Lett.* **67**, 1727 (1991).
- [12] E. T. Jaynes, and F. W. Cummings, *Proc. IEEE* **51**, 89 (1963).
- [13] J. J. Sanchez-Mondragon, N. B. Narozhny, and J. H. Eberly, *Phys. Rev. Lett.* **51**, 550 (1983).
- [14] M. G. Raizen, R. J. Thompson, R. J. Brecha, H. J. Kimble, H. J. Carmichael, *Phys. Rev. Lett.* **63**, 240 (1989).
- [15] Y. Zhu, D. J. Gauthier, S. E. Morin, Q. Wu, H. J. Carmichael, and T. W. Mossberg, *Phys. Rev. Lett.* **64**, 2499 (1990).
- [16] G. S. Agarwal, *Phys. Rev. A* **43**, 2595 (1991).
- [17] H. J. Carmichael, *Phys. Rev. A* **44**, 4751 (1991).
- [18] H. J. Carmichael, R. J. Brecha, M. G. Raizen, H. J. Kimble, and P. R. Rice, *Phys. Rev. A* **40**, 5516 (1989).

- [19] H. J. Carmichael, R. J. Brecha, and P. R. Rice, *Opt. Commun.* **82**, 73 (1991).
- [20] J. H. Eberly, N. B. Narozhny, and J. J. Sanchez-Mondragon, *Phys. Rev. Lett.* **44**, 1323 (1980).
- [21] R. J. Thompson, O. Carnal, Q. Turchette, and H. J. Kimble, OSA Annual Meeting, Toronto, Canada, 1993, p. 187.
- [22] H. J. Carmichael, in *An Open Systems Approach to Quantum Optics*, Lecture Notes in Physics, New Series m: Monographs, Vol. m18 (Springer, Berlin, 1993).
- [23] J. Dalibard, Y. Castin, and K. Molmer, *Phys. Rev. Lett.* **64**, 580 (1992).
- [24] R. Dum, A. S. Parkins, P. Zoller, and C. W. Gardiner, *Phys. Rev. A* **46**, 4382 (1992).
- [25] A. O. Caldeira, and A. J. Legget, *Phys. Rev. A* **31**, 1059 (1985).
- [26] D. F. Walls, and M. G. Milburn, *Phys. Rev. A* **31**, 2103 (1985).
- [27] B. Yurke, and D. Stoler, *Phys. Rev. Lett.* **57**, 13 (1986).
- [28] S. Song, C. M. Caves, and B. Yurke, *Phys. Rev. A* **41**, 5261 (1990).
- [29] B. Yurke, W. Schleich, and D. F. Walls, *Phys. Rev. A* **42**, 1703 (1990).
- [30] C. M. Savage, S. L. Braunstein, and D. F. Walls, *Opt. Lett.* **15**, 628 (1990).
- [31] J. Gea-Banacloche, *Phys. Rev. A* **44**, 5913 (1991).
- [32] P. Meystre, in *Progress in Optics*, edited by E. Wolf (North-Holland, Amsterdam, 1992), Vol. 30.
- [33] M. Brune, S. Haroche, J. M. Raimond, L. Davidovich, and N. Zagury, *Phys. Rev. A* **45**, 5193 (1992).
- [34] B. Sherman, and G. Kurizki, *Phys. Rev. A* **45**, R7674 (1992).
- [35] L. A. Lugiato, in *Progress in Optics*, edited by E. Wolf (North-Holland, Amsterdam, 1984), Vol. 21, p.102.
- [36] W. Ren, J. D. Cresser, and H. J. Carmichael, *Phys. Rev. A* **46**, 7162 (1992).
- [37] R. J. Thompson, G. Rempe, and H. J. Kimble, *Phys. Rev. Lett.* **67**, 1132 (1992).
- [38] L. A. Lugiato, in *Progress in Optics*, edited by E. Wolf (North-Holland, Amsterdam, 1984), Vol. 21, p.106.
- [39] G. P. Agrawal, and H. J. Carmichael, *Phys. Rev. A* **19**, 2074 (1979).

- [40] S. S. Hassan, P. D. Drummond, and D. F. Walls, *Opt. Commun.* **27**, 480 (1978).
- [41] H. J. Carmichael, in *An Open Systems Approach to Quantum Optics*, Lecture Notes in Physics, New Series m: Monographs, Vol. m18 (Springer, Berlin, 1993), p. 156.
- [42] W. H. Louisell, in *Quantum Statistical Properties of Radiation* (Wiley, New York, 1973), pp. 331-347.
- [43] H. Haken, in *Handbuch der Physik*, edited by L. Genzel (Springer, Berlin, 1970), Vol. 25/2c, pp. 51-56.
- [44] M. Sargent III, M. O. Scully, and W. E. Lamb, Jr., in *Laser Physics* (Addison-Wesley, Reading, Massachusetts, 1974), pp. 257-267.
- [45] C. Cohen-Tannoudji, and S. Reynaud, *J. Phys. B* **10**, 345 (1977).
- [46] H. J. Carmichael, *Phys. Rev. A* **33**, 3262 (1986).
- [47] C. M. Savage, and H. J. Carmichael, *IEEE J. Quantum Elec.* **24**, 1495 (1988).
- [48] B. R. Mollow, *Phys. Rev. A* **5**, 2217 (1972).
- [49] L. Tian, and H. J. Carmichael, *Phys. Rev. A* **46**, R6801 (1992).
- [50] R. Graham, in *Springer Tracts in Modern Physics* (Springer, Berlin, 1973), Vol. 66, p. 32.
- [51] H. J. Carmichael, and D. F. Walls, *J. Phys. A* **6**, 1552 (1973).
- [52] P. L. Knight, and P. W. Milonni, *Phys. Rep.* **66**, 21 (1980).
- [53] M. Lax, *Phys. Rev.* **129**, 2342 (1963); *Phys. Rev.* **157**, 213 (1967).
- [54] C. W. Gardiner, and M. J. Collett, *Phys. Rev. A* **31**, 3761 (1985).
- [55] E. B. Davies, in *Quantum Theory of Open Systems* (Academic Press, London, 1976).
- [56] H. J. Carmichael, in *An Open Systems Approach to Quantum Optics*, Lecture Notes in Physics, New Series m: Monographs, Vol. m18 (Springer, Berlin, 1993), Chapter 7 and pp. 157-158.
- [57] H. J. Carmichael, S. Singh, R. Vyas, and P. R. Rice, *Phys. Rev. A* **39**, 1200 (1989).
- [58] H. P. Yuen, and V. W. Chen, *Opt. Lett.* **8**, 177 (1983); B. L. Schumaker, *Opt. Lett.* **9**, 189 (1984).

- [59] P. Alsing, D. S. Guo, and H. J. Carmichael, *Phys. Rev. A* **45**, 5135 (1992).
- [60] B. R. Mollow, *Phys. Rev.* **188**, 1969 (1969).
- [61] H. J. Carmichael, *Phys. Rev. Lett.* **70**, 2273 (1993).
- [62] K. Vogel, and H. Risken, *Phys. Rev. A* **40**, R2847 (1989).
- [63] P. Yuen, and J. H. Shapiro, *IEEE Trans. Inf. Theory*, IT-26, 78 (1980).
- [64] B. Yurke, and D. Stoler, *Phys. Rev. A* **36**, 1955 (1987).
- [65] M. Hillery, R. F. O'Connell, M. O. Scully, and E. P. Wigner, *Phys. Rep.* **106**, 121 (1984).
- [66] R. Loudon, in *The Quantum Theory of Light* (Oxford Science Publications, 1983), p. 148.
- [67] H. J. Carmichael, P. Kochan, and L. Tian, "Coherent States and Open Quantum System: a Comment on the Stern-Gerlach Effect and Schrödinger's Cat", in *Proceedings of the International Symposium on Coherent States: Past, Present, and Future*, edited by J. R. Klauder (World Scientific, Singapore, 1993).